SYNTHESIZING AND SHAPING ULTRAFAST PULSES EFFECTIVELY USING

COHERENTLY GENERATED RAMAN SIDEBANDS

A Dissertation

by

ALEXANDRA ANTONOVNA ZHDANOVA

Submitted to the Office of Graduate and Professional Studies of
Texas A&M University
in partial fulfillment of the requirements for the degree of

DOCTOR OF PHILOSOPHY

Chair of Committee,	Alexei V. Sokolov
Committee Members,	Alexey Belyanin
	Aleksei M. Zheltikov
	Philip R. Hemmer
Head of Department,	Grigory Rogachev

May 2018

Major Subject: Physics

ABSTRACT

Any chemical process can be, in principle, understood and manipulated through electron dynamics. Such dynamics occur on what is known as the "ultrashort" time scale, taking place in 10^{-15} of a second (a femtosecond). Observing or controlling these processes is extremely challenging, as it requires electromagnetic forces that can be arbitrarily shaped in space and manipulated on the sub-femtosecond time scale, i.e. ultrashort laser pulses. Furthermore, the pulses used in such experiments are typically intense enough to modify the optical properties of the material system under study, thereby changing the way the laser pulses themselves propagate. There is thus a need to better understand this "nonlinear" regime before having the ability to demonstrate full control. This thesis describes the experiments and simulations we used to study the spatial and temporal physics in the ultrashort nonlinear processes of filamentation and stimulated coherent Raman scattering in solids. In particular, we develop several novel techniques for pulse synthesis by taking advantage of these two processes. By recombining Raman sidebands and characterizing the resultant pulse via cross-correlation interferometric FROG (ξFROG), we synthesize an ultrashort ≈ 5 fs pulse. Meanwhile, in filamentation, we contribute to an alternate pulse synthesis technique by means of nonlinear spatio-temporal waveform coupling. We use liquid crystal spatial light modulators to influence the spatial domain and find a substantial increase in the possible frequency bandwidth generated in this technique, potentially leading to shorter and more stable pulses. Deeper physical insight was achieved via comparison of experimental results with supercomputer simulations.

"In a minute there is time

For decisions and revisions which a minute will reverse."

T.S. Eliot, *The Love Song of J. Alfred Prufrock*

ACKNOWLEDGMENTS

Many wonderful people helped me in the experiments and simulations detailed in this thesis. Firstly, I want to thank the unsung heroes of the university: the TAMU Facilities Services division. Dwight and Sam, you guys are amazing and this dissertation would have taken another three years without you. To the Physics and IQSE offices, Veronica, Cheryl, Heather, Michelle, Brendan, Sherree, Kim H., Kim C., and Jay: thank you for being incredibly helpful while putting up with my antics, strange requests, and constant badgering. Garrick and the machine shop: thanks for being wizards and making magic out of the most commonplace materials. Yujie, Aysan, David, Jonathan, Tony, and Masha: thank you for being my co-authors, sharing your skills with me, and staying with the experiments through the terrible times. Zhenhuan: thank you for being reliable and awesome. Kai, Miaochan, and Ilya: thank you for teaching me the basics of being an experimentalist. Dr. Sokolov: thank you for giving me freedom and guidance in equal measure. Vlad: thank you for being especially helpful at vital junctures. Tatiana: you are an incredible inspiration, thank you for showing me the fun side of physics. Thanks to my committee, Dr. Alexey Belyanin, Dr. Aleksei Zheltikov, and Dr. Phil Hemmer, for being there at the most important times in my PhD and for your collaboration and direction.

On the less professional side; James with a TIARA, Joe, Charles, Chyzh, Dasha, Emily, Ira, Fefe, Oleks, Marianna, Ranji, Roman, Sara, Stef, Timur, and Liza: thank you for being my friends through a difficult time. Matt and Cameron: thanks for being fun :) John, Dawson, and Sean: thank you for keeping cool and talking through. Liz, Alexia, Natalie, Varsha, and Matthias: thank you for giving me advice when I needed it most, and keeping in touch despite the distance. To my DEEP students: thank you for being distracting in the best way possible.

This document would never have been written without the support of my family. Vlad and Lena insisted on weekly experimental reports in exchange for delicious food and many wonderful ping-pong matches. My cousin and my great aunt, Grisha and Lena, are a constant model for me to be more cool. My parents taught me that its good to be different and pushed me to follow my

dreams. My mechanically-inclined sister, Katya, showed me how to successfully collaborate with engineers, and my youngest sister, Zina, reminds me how to enjoy the simple things in life (like trampolines).

Finally, to Pita: you are the best. Thank you.

CONTRIBUTORS AND FUNDING SOURCES

NOMENCLATURE

AS	Anti-Stokes
fs	femtosecond
FFT	Fast Fourier Transform
FROG	Frequency Resolved Optical Gating
FTL	Fourier-Transform Limited
FWHM	Full-Width at Half-Maximum
OAM	Orbital Angular Momentum
SFG	Sum Frequency Generation
SHG	Second Harmonic Generation
SLM	Spatial Light Modulator
TAMU	Texas A&M University
TC	Topological Charge

TABLE OF CONTENTS

Page

xiii

LIST OF TABLES

1. INTRODUCTION AND LITERATURE REVIEW

1.1 Motivation

There are a variety* of motivating factors for the study of nonlinear effects. For example, ultra-fast coherent Raman spectroscopy has several key advantages over the more traditional CW Raman spectroscopy; it produces a higher signal-to-noise ratio, allows for greater chemical selectivity, and provides a pathway towards even better precision and setup simplification. It is also highly convenient for measurements that are simply not possible in the CW regime, in particular, high resolution measurements in the time as well as the spatial domains. Such measurements are currently driving the rapidly developing field of attoscience, which aims to understand the temporal scale beyond the femtosecond regime [12]. The long-term goal of this field is to understand the dynamics of ultrafast, fundamental processes in atoms, molecules, nanosctructures, and biological samples that occur on the time scale of electron motion – the attosecond time scale. However, these observations often demand arbitrarily controllable waveforms. Sub-fs waveforms in the visible regime are particularly desirable, as such waveforms would necessarily have a pulse duration shorter than the optical period and allow sub-cycle field shaping.

This possibility has led to the optical arbitrary waveform generation (OAWG) technique, a combination of pulse shaping methods and Nobel-prize-winning optical comb technology [13]. It has many applications, such as coherent control over quantum mechanical processes and the manipulation of high-field laser-mater interaction [14]. Weiner's group demonstrated programmable line-by-line shaping of more than 100 spectral lines and recently demonstrated line-by-line pulse shaping on frequency combs generated from silicon nitride micro-ring resonators [15]. Many of the current efforts currently only manipulate a relatively small number of comb lines.

Present techniques produce pulses with shaped temporal envelopes; these already allow for coherent control of molecular dynamics and chemical reactions [16]. Sub-cycle shaping will lead

---

*Section partially adapted with permission from "Coherent Raman generation in solid-state materials using spatial and temporal laser field shaping" by A. Zhdanova, M. Zhi, and A. Sokolov, [1].

Table 1.1: Comparing selected sources of isolated, single-cycle, optical pulses. From this table it is clear that our group eventually plans to achieve nearly equal bandwidth as the source of Goulielmakis, *et al.*, but will have greater flexibility and $4\times$ as much power thanks to our multiband approach.

Group Name	Technique	Bandwidth	Pulse Energy	Pulse Duration
Krausz, Goulielmakis	divided supercontinuum [18]	275-1250 nm	320 μJ	380-975 as < 1 cycle
Kärtner	OPCPA [19]	750-1100 nm $+$ 2.0-2.5 μm	15 μJ	4.2 fs, 0.8 cycles
Baltuška	Self-compressed filaments [21]	3.0-4.5 μm	20 mJ	30 fs, < 3 cycles
Sokolov (envisioned)	Raman + OPA Pulse Synthesis	350-1250 nm	$\approx$1 mJ	≈ 500 as, < 1 cycle

to the synthesis of waveforms where the electric field is an arbitrary predetermined function of time, not limited to quasi-sinusoidal oscillations. As a result, direct and precise control of electron trajectories in photoionization and high-order harmonic generation will become possible. Such sub-cycle waveforms have been generated in the work of Hassan, Wirth, *et al.* who reported on the generation of sub-cycle field transients spanning the infrared through the ultraviolet spectral regions with a >2-octave four-channel optical field synthesizer [17, 18]. Further, Huang *et al.* recently presented a light source that enables sub-cycle waveform shaping with a two-octave-spanning spectrum and a pulse energy of 15 μJ [19]. The same group produced a light source that uses a pulse shaper to shape their pulse prior to compression and amplification [20]; however, their resultant power is lower and pulse duration is longer compared to [19]. Finally, self-compressed filaments [21] also have the potential to serve as a source of high power, single-cycle pulses. All of these techniques are compared in Table 1.1.

The goal of this thesis is to better understand the spatial and temporal effects that come into various aspects of this sub-cycle field shaping in order to improve on the aforementioned techniques. Chapter 2 deals with the specific spatial physics associated with topological charge and

orbital angular momentum in the coherent Raman process. Chapter 3 will discuss experiments and simulations that pertain to more general aspects of spatial shaping, but applied to supercontinuum generation rather than coherent Raman; the results from this chapter were eventually brought back to coherent Raman experiments by Shutova, et al. [22]. After this, Chapter 4 will cover my work on the spectral shaping and characterization of < 10 fs waveforms from coherent Raman beams. Finally, Chapter 5 will cover preliminary experiments we did on using these < 10 fs waveforms to ionize Xenon gas.

Although this seems to be unusual, I have listed part numbers for all experimental equipment (including translation stages/dichroics/everything else) and prices where I feel relevant. I feel that a large part of my thesis was spent in obtaining quotes and hunting parts, and I would like to give the prospective student a feel for where/from whom things are bought so they are not completely mystified like I was. I hope the inclusion of prices will also give them a feel for which parts to treat with great care (the 10 micron BBO) and which parts can be reasonably thrown around (the lead tungstate crystals).

1.2   Producing Ultrafast Pulses (in General Terms)

1.2.1   Requirements

In order to accurately produce ultrafast pulses, one needs to have [23]:

- A broad, coherent bandwidth (for perspective, a bandwidth stetching from at least $785 - 815$ nm FWHM is needed for a ~ 35 fs FWHM Gaussian pulse). Optional but highly recommended: a way to adjust the phases of different parts of the bandwidth.

- A way of measuring ultrafast pulses and probing their coherence and spectral phase.

The spectral phase plays a critical role in determining how the bandwidth of an ultrafast pulse will translate to the temporal domain. If the spectral phase is not ideal (resulting in a Fourier-transform limited pulse), then the pulse will be distorted and so will be not the shortest possible pulse. The spectral phase can be measured by many techniques, but the research described here will

mostly employ the FROG technique developed by R. Trebino and its closely related variants [24]. The basic FROG technique involves making a delayed copy of the pulse to be measured (generally using a beamsplitter and translation stage) and then using that to "gate" the original pulse. The signal can be read out from various nonlinear effects by scanning the time delay between the pulses, and then an iterative algorithm attempts to reconstruct the pulse from the resulting "spectrogram".

As will be most relevant to later parts of this thesis, the second pulse does not have to be an exact copy of the first pulse. Indeed, it is possible to reconstruct a pulse from the interaction between the pulse and a frequency-shifted copy of it using the process of sum-frequency generation (SFG) [25].

As of the writing of this dissertation, the shortest possible pulses have been produced with the technique of high-harmonic generation in low-pressure gas cells [26, 27]. However, the efficiency of this technique is relatively low and the pulses produced with this method are unable to cover the visible spectrum. There has been further work on alternate methods, including the molecular modulation technique.

1.2.2 Molecular Modulation

The molecular modulation technique was first described by Sokolov, et al., who predicted that coherent molecular oscillations can produce laser frequency modulation (FM), with a total bandwidth extending over the infrared, visible, and ultraviolet spectral regions, and with the possibility of subfemtosecond pulse compression [28, 29]. This technique utilizes the idea of Electromagnetically Induced Transparency (EIT) and relies on the adiabatic preparation of maximal molecular coherence. The coherence is established by driving the molecular transition with two single-mode laser fields slightly detuned from the Raman resonance so as to excite a single molecular eigenstate. Molecular oscillations, in turn, modulate the driving laser frequencies, causing the collinear generation of a very broad FM-like spectrum.

Over the course of recent years, several groups have made substantial advances in molecular modulation. Harris' group has demonstrated a nearly 100% conversion efficiency in rotational molecular modulation [30] and used their Raman light source to demonstrate single-cycle pulse

compression [31]. Katsuragawa's group has implemented substantial technological improvements and has shown line-by-line control of a 10-THz-frequency-spacing Raman comb by employing a combination of a spatial phase controller and a spectral interferometer; this led to a 10 THz ultrafast function generator, capable of generating rectangular and triangular pulse trains [32, 33, 34]. Marangos' group has performed detailed studies of molecular modulation in gases driven by nanosecond and femtosecond laser pulses, and has also investigated the possibilities of hollow-core fiber pulse compressors [35, 36]. Recently, Kung's group achieved the absolute phase control of five discrete optical harmonics (two pump beams and three generated Raman sidebands from H_2 gas), and thus has demonstrated the synthesis and measurement of ultrafast waveforms such as square and saw-tooth fields [37].

The molecular modulation technique I used for the work in this thesis has been originally developed to utilize low-pressure molecular gases adiabatically driven by transform-limited nanosecond laser pulses. The results of this technique were summarized in [38]. However, Zhi et al. have extended this technique to a qualitatively different time regime and to a different state of medium – Raman-active crystals driven by (optimally shaped) femtosecond and picosecond pulses [39, 11, 40]. A typical free-space image and bandwidth obtained by this technique is shown in Fig. 1.1.

The work of Zhi, et al. in extending this technique allowed me to build free-space setups that have the potential for miniaturization and compactness, while not sacrificing bandwidth or power. Any Raman-active crystal will in principle work with this technique, but we have chosen $PbWO_4$ and diamond as our crystals of choice.

1.3 Producing Ultrafast Pulses (in Specifics)

1.3.1 Broadband Coherent Light Generation in Raman-Active Crystals

Lead tungstate ($PbWO_4$) belongs to the tetragonal crystal system; it has attracted attention in the recent years as the material for the Compact Muon Solenoid's (CMSs') scintillation detector at CERN [41]. Lead tungstate features a wide optical transparency, a relatively large damage
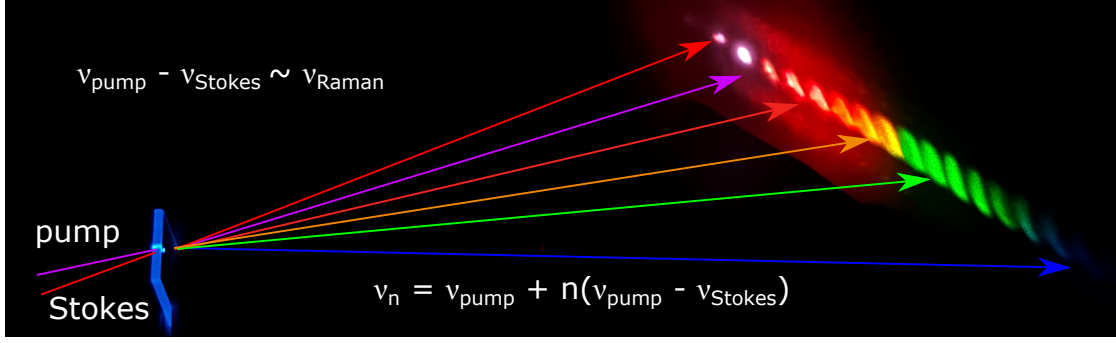
Figure 1.1: Typical sidebands generated by two-color femtosecond laser fields in a $PbWO_4$ crystal, where ν_{pump} is the frequency of pump and ν_{Stokes} is the frequency of Stokes. Selected antiStokes (AS) sidebands are marked, as is the formula for the frequency ν_n of the nth sideband, AS n. Figure 1.2 shows the full setup for generating such sidebands. Adapted from [1].

Table 1.2: Properties of $PbWO_4$ that will be used throughout the thesis. Data from [9]
.

$PbWO_4$ Facts	
Space Group	$C_{4h}^6 - I4_1/a$
Optical Transparency	0.33 - 5.5 μm
Density	8.23 g/cm^3
Crystal Type	Negative Uniaxial: $n_o > n_e$
Bandgap	4.5 eV
Main Raman Modes, ν_R	191, 325, and 903 cm^{-1}

threshold, and high density. These properties have contributed to its success as a Raman lasing medium [42, 43]. The specific numbers can be found in Table 1.2. The crystal also has several Raman transitions – 191, 325, and 901 cm^{-1} being the most prominent. Throughout the following experiments, a 1 mm thick crystal is used.

Diamond is a theoretically much simpler system. It has a higher optical damage threshold and a single Raman mode; its thermal conductivity is ≈ 2000 times that of sapphire. It is, however, much more expenisve. Hence, preliminary results in this dissertation are often obtained with $PbWO_4$ then repeated in diamond. The important material properties are summarized in Table 1.3.

Table 1.3: Properties of Diamond (C) that will be used throughout the thesis. Data from [10]

C Facts	
Space Group	Fd-$3m$
Optical Transparency	0.225 μm – far IR
Density	3.5 g/cm^3 or 1.77$\times10^{23}$ atoms/cm^3
Crystal Type	Isotropic
Bandgap	5.45 eV
Main Raman Mode, ν_R	1332 cm^{-1}

In order to produce cascaded Raman sidebands from either PbWO$_4$ or diamond, the bare requirements are to have a pump and a Stokes pulse with equal polarizations. For all experiments, it is absolutely necessary to have the beams at least partially overlap in time. The wavelengths for pump and Stokes excitation are tunable, the idea is simply to match the frequency difference between them to whichever Raman mode we are most interested in. The Raman modes with smaller difference hence even allow for chirped-pulse based excitation schemes [11] that utilize a single pulse split in two rather than two separate colors [39]. Having the pulse split in two is still necessary to satisfy phase-matching conditions so that the sidebands are efficiently generated; unlike in gasses, the sidebands can not be produced collinearly. The frequency spacing between each Raman sideband is not quite equal to the Raman shift and is affected by this phase-matching angle as well as polarization [11, 1]. The basic setup for generating Raman sidebands via two-color excitation is shown in Fig. 1.2.

As a side note, while spectroscopists work in units of cm^{-1}, it is often more convenient to convert to the wavelength for laser specialists:

$$\delta\nu * 10^2 \frac{\text{cm}}{\text{m}} = \frac{1}{\lambda_{pump}} - \frac{1}{\lambda_{Stokes}} \tag{1.1}$$

Where $\delta\nu$ is the frequency difference between pump and Stokes in wavenumbers (cm^{-1}) and is ideally slightly detuned from the Raman mode ν_R for proper excitation, and $\lambda_{pump}/\lambda_{Stokes}$ are the wavelengths (in m) for pump and Stokes beams respectively.
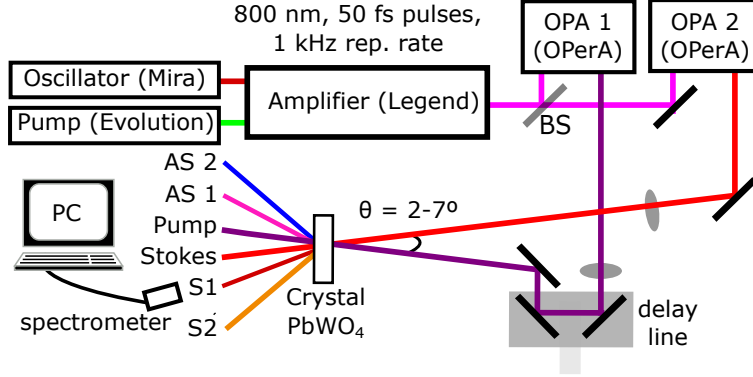
Figure 1.2: A typical two-color Raman setup to generate several cascaded Raman sidebands in PbWO$_4$. "BS" stands for 50/50 beamsplitter. A retroreflector or two mirrors on a translation stage may be used as a delay line to adjust the temporal overlap between the two beams. Adapted from [1].

We can measure the overall conversion efficiency of the pump beam to the sidebands as follows. We first measure the power of the pump beam after the crystal while blocking the Stokes beam (there is therefore no sideband generation) and call it P_1. Then we measure the power of the same beam with the Stokes beam present (i.e. so that sidebands are generated) and call it P_2. We call $\frac{P_1 - P_2}{P_1}$ the conversion efficiency. As described below, high efficiency conversion of pump energy to the Raman sidebands has been demonstrated: 31% for two-color pumping and 25% for the chirped-pulse based pump. The generated spectrum extends from the infrared, through the visible region, to the ultraviolet, and it consists of discrete spatially separated sidebands, as shown in Figure 1.1. We therefore define a conversion efficiency to a specific order as $\frac{P_{ASn}}{P_1}$, where P_{ASn} is the power of the nth order of sideband.

Such high efficiency is achieved by using intense ultrafast pulses (1-2 μJ/pulse focused to about a 100 μm spot size on the crystal) and by taking care to satisfy phase-matching conditions.

1.3.2   Femtosecond Lasers

For the experiments in Section 2 and 4 as well as Appendix 5, I used a femtosecond (fs) Ti:Sapphire laser system developed by Coherent. In detail, the seed laser (Mira, Coherent) is a mode-locked (via the Kerr Lens mechanism) ultrafast laser that produces ultrashort, wide-bandwidth
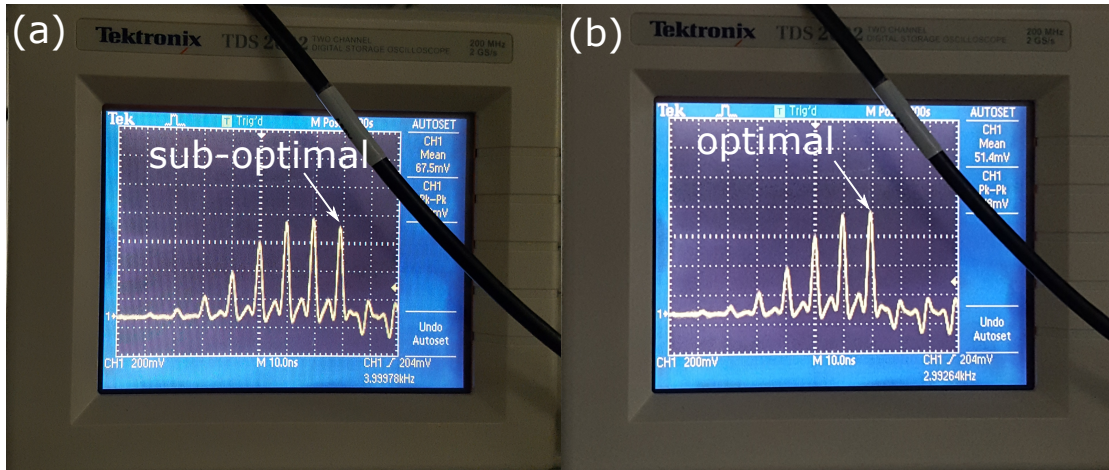
Figure 1.3: Amplifier signal as read out by a photodiode in the amplifier cavity. There are many round trips that are not shown in the signal as they are much weaker than the last few. (a) Sub-optimal number of round trips, resulting in lower power out of the amplifier. This extra peak can be eliminated by tweaking the timing for Pockels Cells 1 and 2. (b) Optimal number of round trips.

(>50 nm), fs pulses (<20 fs) using a Ti:Sapphire crystal as the gain medium. The output pulse has a repetition rate of 76 MHz with a wavelength at 800 nm. The pulses are then stretched by a grating to about 200 ps and then used to seed a Ti:Sapphire regenerative amplifier system (Legend, Coherent). This is in turn pumped by a pulsed, frequency-doubled Nd:YLF laser at 523.5 nm (Evolution, Coherent). The number of round trips that each amplified pulse makes in the cavity before exiting can be fine-tuned by adjusting the timing of the entrance/exit gate keepers, called "Pockels cells". There is generally an optimal number of round trips, as shown in Fig. 1.3, and the precise timing can and does change from day-to-day. Generally, one wants $140 - 160$ s between the timing for Pockels Cell 1 and Cell 2 [44].

The amplified pulses are afterwards compressed by a grating compressor; in optimal conditions, the pulse should have > 1.0 mJ of energy/pulse (at a stability of $<1\%$ RMS) at a 1 kHz repetition rate and pulse duration of < 35 fs FWHM. However, these optimal conditions are subject to day-to-day flux. For example, the optimal Pockels Cell timing mentioned before really should be adjusted daily to maximize the power out of the laser. In the case of dramatic timing changes, where adding or subtracting a round trip is necessary, the pulse at the output will be

9

severely chirped. **Adding** a round trip results in a very **negatively** chirped pulse, so the chirp needs to be adjusted in the positive direction to correct for this. A handy mnemonic for remembering this: "add a round trip, add chirp." Subtracting a round trip results in the opposite issue.

This amplified pulse is used to pump two computer-controlled optical parametric amplifiers (OPerA, Coherent). For an in-depth explanation of optical parametric amplification (OPA), see Boyd [25]. For our purposes, within each OPA, the pulse is down-converted to a a signal pulse (the short wavelength, $1150 - 1600$ nm) and an idler pulse (the long wavelength, $1600 - 2630$ nm). These pulses can then be frequency doubled or mixed with the fundamental pulses to produce up to 30 μJ per 50 fs Gaussian pulse at tunable visible wavelengths.

For the experiments in Section 3, a very similar but much newer Ti:Sapphire laser system was used. The mode-locking, stretching, and gain are all the same. The seed laser is renamed Micra from Mira, and the Legend is renamed the Legend Elite. At the time of the experiments, there were no OPAs attached to the system and hence none used for the experiments.

1.3.3 Previous Raman-Based Schemes

Our group has produced and tested various schemes for recombining Raman sidebands and thereby producing ultrashort, visible, isolated fs pulses [8, 2, 3, 45]. Most relevant to our current research are the "Phazzler" setup [8, 2, 46] and the "spherical mirror" setup [3, 45].

For the "Phazzler" setup, the sidebands were recombined using a prism and a spherical mirror (for collimation). The setup and results are shown in Fig. 1.4. The beam profiles were optimized using a beam profiler and then sent to an acousto-optic pulse shaper (Phazzler, FastLite). Zhi, et. al were able to program the pulse shaper to align all sidebands spatially and temporally, and then used the pulse shaper to vary the phase of each of the sidebands. As they varied the phase of each sideband, they recorded the SFG and SHG spectrum of each sideband from a 20 μm BBO included in the pulse-shaping unit. This way, they were able to show that the sidebands are mutually coherent, as they observed coherent beats in the SFG and SHG spectrums as each sideband's phase varied. These beats are slightly controversial in the sense that Zhi, et al. reported one interpretation of the beat duration. There are several possible interpretations, as discussed in
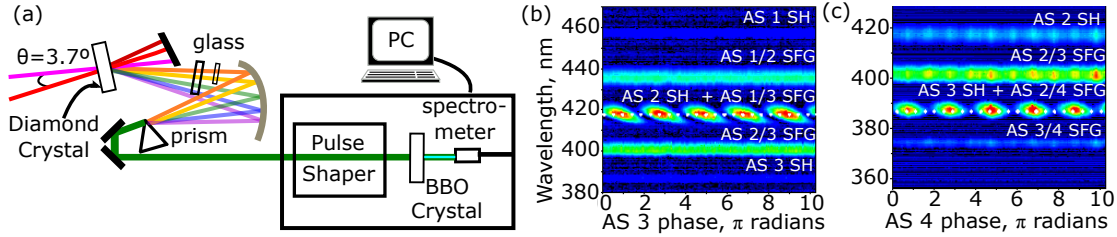
Figure 1.4: (a) Schematic of the experimental setup. In this experiment, a spherical mirror (instead of a lens) is used to focus the Raman sidebands to the prism in order to minimize dispersion. The glass plates are inserted (and tilted as needed) so as to coarse-tune the spectral phases, thus producing a waveform precompensated for pulse shaping by Dazzler. (b), (c) Adapted from [2]. SHG/SFG spectrum generated by (b) AS 1, AS 2, and AS 3 sidebands in the BBO crystal, as the AS 3 phase is varied; (c) AS 2, AS 3 and AS 4 sidebands in the BBO crystal, as the AS 4 phase is varied. The dotted lines in the 420/390 nm (b, c) bands were added post-data collecting to better show the coherent beating. Adapted from [1].

Section 4.4.1.

They were also able to completely optimize the phase of their sidebands and produce Fourier-transform limited pulses: a pulse duration of 3.2 fs from 5 sidebands was reported in [8] (originating from the 50 fs laser described earlier). There is the caveat that the pulses synthesized in this way are limited by power to 100 μJ/pulse (for comparison, the full power we have available using our laser system is 1 mJ/pulse), as the Phazzler is very sensitive to power and can easily be permanently damaged [47].

In an attempt to get around this power limitation, the group moved onto schemes that allowed pulse shaping without a pulse shaper, but with spherical and/or deformable mirrors instead [3, 45]. The experimental setup is depicted in Figure 1.5 (a). Pump and Stokes were reflected by one spherical mirror back to the crystal, while AS 3-7 were reflected by a different spherical mirror. The second spherical mirror was put on a translation stage and so could be scanned to produce a spectrogram: the spectrum of the sidebands after the crystal was collected by a spherical mirror/spectrometer pair and measured as the delay was scanned. Hence, instead of using the SFG process to characterize their pulses, the Raman process was used. They observed similar beats in the Raman spectrum as they had previously in the SFG spectrum and so were able to retrieve the

11
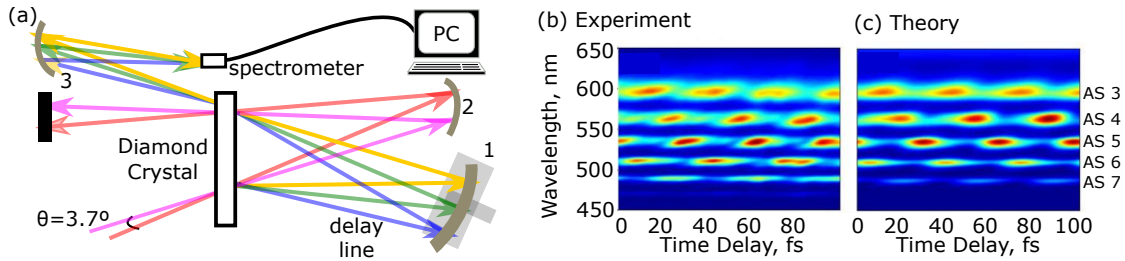
Figure 1.5: (a) Schematic of the experimental setup. The size of the diamond crystal relative to the beampath is greatly exaggerated. Only three (our technique utilizes five) sidebands are shown reflecting off of Mirror 1 for clarity. Pump and Stokes are reflected and focused by Mirror 2, while Mirror 3 serves as a collecting mirror for the spectrometer. (b), (c) Adapted from [3]; Experimental (b) and theoretical (c) interferograms of AS 3-7. The theoretical simulation is in agreement with the experimental results within a 10% average error. Adapted from [1].

pulse duration. In order to improve on this setup, they substituted a deformable mirror in place of the spherical one and so were able to at least roughly optimize all 5 sidebands. As a result, they report a 7 fs pulse obtained from 5 sidebands [45].

Nevertheless, we improved on the work of Wang, Zhi et al. by combining different parts of their setups that worked the best. We used the SFG signal to more accurately characterize our pulses than the Raman signal, and our setup allows for individual control of each sideband by fully separating each one. This will be further discussed in Section 4.

12

2.   THE RAMAN PROCESS WITH OPTICAL VORTICES

2.1   Introduction

An optical vortex (OV)* is a simple yet intriguing object which finds its use in a multitude of areas of research and technology [48]. An optical vortex beam exhibits a characteristic donut-shaped transverse profile (a ring of light) with a spiral wavefront. The zero-intensity center axis of such a beam is a basic light-wave phase singularity [49]. An integer number of 2π phase accumulation around one turn of the wavefront spiral corresponds to integer topological charge (TC), or, in the ideal case, an integer amount of orbital angular momentum (OAM) that the vortex carries [50]. Vortex beams with varying amounts of OAM are shown in Fig. 2.1.

As He *et al.* showed in [51], a focused optical vortex can impart its orbital angular momentum onto a trapped microparticle and make it spin in a direction determined by the helicity of the beam. Of particular pertinence to the Raman interaction of optical vortices is a study of optical vortices interacting nonlinearly in atomic vapors [52], where TC transfer allows identification of nonlinear pathways. A variety of vortex applications, however, simply utilize its stable and reproducible donut shape, with a perfectly dark center, resulting from destructive interference at the point of phase anomaly. In optical tweezers, vortex beams are used for studying proteins as well as for micro- (and nano-) manipulation of absorbing or scattering particles such as biological cells [53, 54, 55]. In stimulated-emission-depletion (STED) microscopy, an optical vortex serves as a perfect depletion beam [56]. In astronomy, a vortex coronagraph allows for the detection of faint extrasolar planets near their very bright host stars [57, 58]. Other interesting applications of optical vortices include quantum [59] and classical [60] communication systems based on information encryption via OAM states of photons.

As explained earlier, coherent multi-sideband Raman generation offers opportunities for the production of ultrashort (sub-femtosecond) optical pulses of adjustable shapes and for non-sinusoidal

---

*Section partially adapted from "Topological charge algebra of optical vortices in nonlinear interactions," by A. A. Zhdanova, M. Shutova, A. Bahari, M. Zhi, and A. V. Sokolov [4].
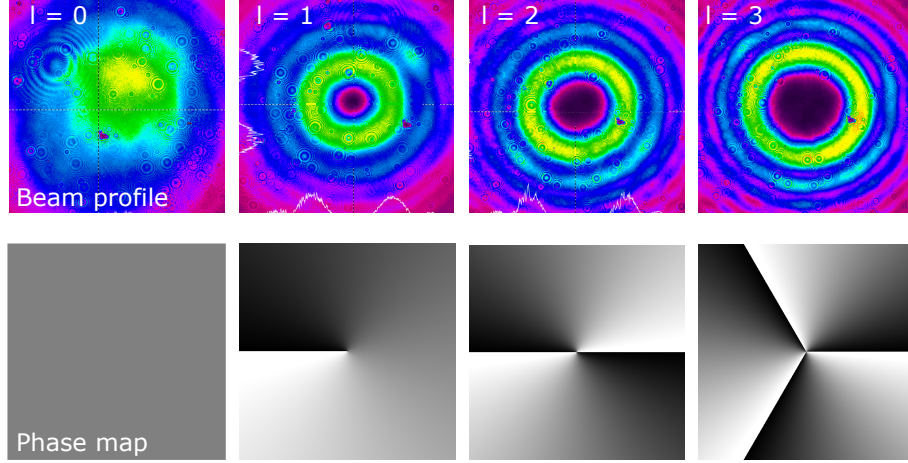
Figure 2.1: Experimentally obtained vortices from $l = 0$ (a Gaussian beam) to $l = 3$. 2-Dimensional plots of the phase across the beam are shown in the lower row for each beam profile. Adapted from [4].

field synthesis [61, 39, 62]. The possibility of adjusting the transverse beam profile and producing coherent Raman sidebands of various vortex shapes adds another dimension to light-field shaping. Furthermore, before the work of Sokolov et al., little was known about the role of optical vortices in the Raman interaction [63, 64, 4]. My work, specifically, investigated how orbital angular momentum (OAM) is transferred in such an interaction, thereby obtaining a deeper understanding of the theory behind the Raman interaction and pulse manipulation. Mathematically, an optical vortex beam propagating along the z axis in cylindrical coordinates can be represented by a complex field:

$$
\begin{aligned}
E(\rho, \phi, z, t) = & E_0 \frac{w_0 \rho^{|l|}}{w^{|l|+1}} \exp\left[\frac{-\rho^2}{w^2}\right] \\
& \times \exp[-i(|l|+1)\arctan\frac{z}{z_R} + \frac{ik\rho^2}{2R(z)} + i(l\phi + kz - wt)]
\end{aligned}
\tag{2.1}
$$

where ρ, ϕ are polar coordinates in the transverse plane; w_0 is the radius of the beam at the beam waist (at $z = 0$); E_0 is amplitude parameter; $w = w_0(1 + z^2/z_R^2)^{1/2}$ is the transversal beam radius; $z_R = kw_0^2/2$ is the Rayleigh range; $R(z) = z(1 + z_R^2/z^2)$ is the radius of the wavefront

curvature; l is the value of the TC; k is the wavenumber [48].

2.1.1   Topological Charge Transfer

Topological charge is related to the OAM of a beam in a pure Laguerre-Gaussian state of order l through the relation:

$$l\hbar = \text{OAM} \tag{2.2}$$

However, it is generally not the same [65, 66]. Nonlinear processes involving vortex beams also generally involve the transfer of TC, in order to converse photon momentum or in regards to phase-matching conditions. The equation that governs TC transfer in optical vortices may be derived from either orbital angular momentum conservation for created and annihilated photons or, equivalently, from considerations of phase-matching between the applied and generated beams. OAM, as a rule, is only conserved in cylindrically symmetric systems (*i.e.* in collinear setups), but is approximately conserved at sufficiently small angles (on the order of $10°$, which is significantly larger than the value used in our experiments), as [59, 67, 68, 69] have shown in spontaneous parametric down conversion, second harmonic generation, and four wave mixing.

Following the orbital angular momentum conservation argument in order to derive the equation that governs TC transfer in the Raman interaction, we note that one photon is added to the Stokes pulse and two photons are removed (annihilated) from the pump pulse to make a photon of the first anti-Stokes (AS) sideband, so that the resulting OAM conservation equation becomes $l_{AS1} = 2l_p - l_s$. Hence, by applying the same logic to n sidebands, we may derive a simple equation that clearly predicts the TC of each sideband:

$$l_n = (n + 1)l_p - nl_s \tag{2.3}$$

where n is the order of the sideband (*i.e.* $n = 1, 2,...$ correspond to AS orders, and $n = -1, -2,...$ correspond to Stokes orders), l_n is the TC of a sideband of order n, l_p is the TC of the pump, and $l_s = l-1$ is the TC of Stokes [63]. In the language of phasematching, this conservation of orbital

15

angular momentum comes from a phase relationship among the applied and generated beams: $\phi_n = (n+1)\phi_p - n\phi_s$ (where ϕ_n is the relative phase of the nth field, in the transverse plane) [63]. This is analogous to how photon momentum conservation is equivalent to wavevector (k-vector) matching.

2.2 Experimental Methods

2.2.1 Vortex Production and Measurement

There are several methods to convert ordinary Gaussian beams into vortex beams. This can be done with the help of spiral phase plates [64, 63], computer-generated holograms (or gratings with defects) [70], or SLMs [71, 72, 73]. In our present work, we use an SLM-based method. Our particular SLM modulates the phase of incoming light as it reflects off of a mirror covered by a programmable liquid crystal layer. We program this liquid crystal layer using computer-generated phase masks, an example of which is shown in Fig. 2.2. These phase masks are actually bitmaps where the darkness of each pixel varies based on basic equations for the phase that should be added to a Gaussian beam in order to produce a vortex beam. For example, for a first order vortex beam generated from a Gaussian beam, $\phi = \tan(\frac{x}{y})$ (for in-plane angle $\theta = 0$ to $\frac{\pi}{2}$), where ϕ is the added phase, x is one spatial direction in the plane of the beam, and y is the perpendicular spatial direction (again, in the plane of the beam). An analogous relationship can be defined for a 3rd order vortex, as shown by Fig. 2.2a).

Several methods have been proposed for measuring the topological charge of optical vortices. These include using the diffraction pattern after propagating an optical vortex through an annular aperture [74] or by using a cylindrical lens [75]. One popular method involves building an interferometer and studying the interference pattern produced between a Gaussian beam and a vortex beam [76]. Our group has employed this method in the past, generating two sets of coherent Raman sidebands by two sets of input beams, one set of vortices and another set of reference Gaussian sidebands [64, 63], and then interfering them. Another, simpler method was proposed by P. Vaity *et al.* [77]. The essence of this method is to use a tilted lens to determine the topological charge of an
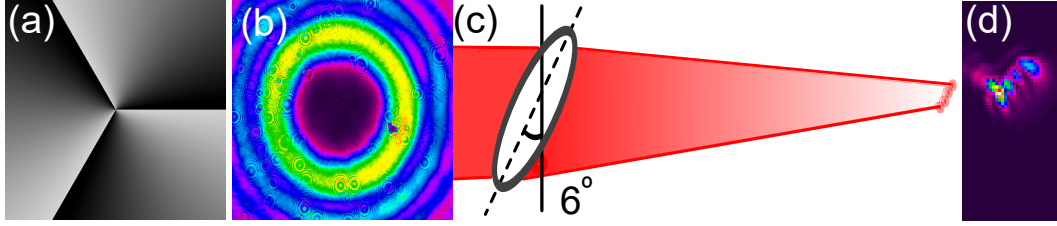
Figure 2.2: Production and measurement of optical vortices. (a) Computer-generated phase mask applied to the SLM to generate a donut-beam. (b) Donut-shaped beam profile (taken approximately 76 cm after the SLM) resulting from Gaussian beam reflection off of the SLM. (c) Schematic of an astigmatic focusing method for TC measurement. (d) Resultant intensity distribution in the focal plane. Data in (a), (b), and (d) are shown for a vortex beam with TC = 3, hence we see 4 distinguishable spots in part (d). Adapted from [4].

optical vortex by taking advantage of astigmatic focusing produced by this lens, as demonstrated schematically in Fig. 2.2 c) and d). This astigmatic focusing results in the vortex breaking up in the focus of the lens into a number of nodes equal to its TC + 1. The main advantages of this method are its simplicity and clarity; in addition, because there is no need for a reference beam, we have more power available to generate higher order optical vortices. Previously, we have employed this method and showed that it performs equally well to the standard interferometric method (albeit without giving detailed phase information) in determining the topological charge of each sideband [64].

2.2.2 Optimizing Vortices Produced via SLM

We used a MATLAB program to generate the inital phase masks using the atan function. However, we quickly noticed that the uncorrected phase masks were producing very ugly vortices. We corrected this by adding "fudge factors" to the phase masks - adding a constant factor (c_1) to the whole phase mask and dividing by a different constant factor (c_2). We optimized both of these parameters empirically by using a beam profiler to characterize the "darkness" in the center of the vortex hole and the evenness of the vortex ring. This optimization process is illustrated in Fig. 2.3, where the results of two similar phase masks but with different phase corrections are compared.

While the corrections may seem minor, it is important to remember that we are using the vor-
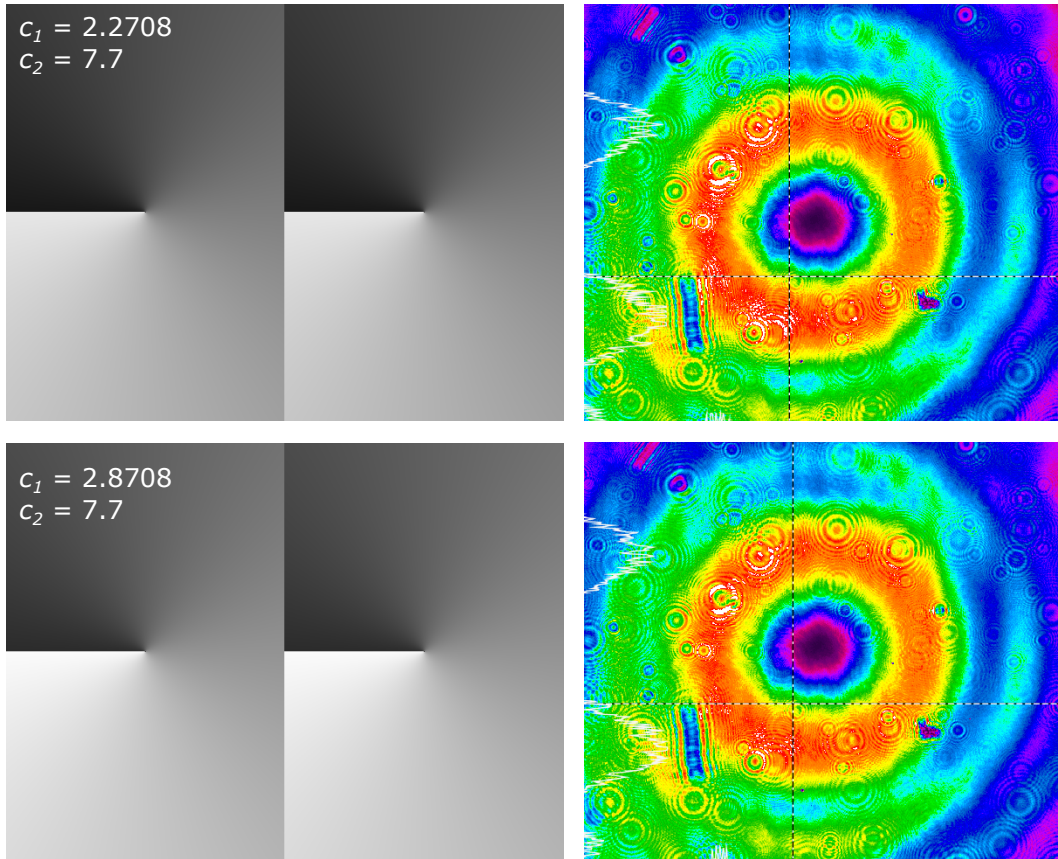
Figure 2.3: Optimization of vortex beams. The phase masks on the left are used to generate to the vortices on the right. c_1 and c_2 are defined in the text as "fudge factors" - i.e. factors that affect the brightness of the phase mask and result in different vortices. Note that the ring of the vortex on the bottom is smoother than the ring of the vortex on the top. The blue line in the lower left of each vortex profile is an artifact of the beam profiler and not present in the vortex beam itself.

tices to generate many orders of cascaded Raman sidebands. This is a highly nonlinear interaction, and each error in the topological construction of the vortex will be reproduced and exagerrated throughout the different sideband orders.

2.2.3 Coherent Raman with Chirped Pulses

This experiment used a "one-color" scheme to excite the 325 cm^{-1} Raman mode of PbWO$_4$ [11], as we confirmed with a spectrometer. We used one linearly chirped pulse that has been split in two, such that one copy serves as "pump" and the other serves as "Stokes" [11]. This eliminates the need for OPA systems (which not every laboratory owns) and allows for an easier setup and higher power in the sidebands, as the threshold for self-phase modulation (SPM) and other parasitic processes is pushed back. Unfortunately, this comes at the cost of having temporally longer sidebands.

We use the laser system described in Section 1.3.2, but we now chirp the pulses by deliberately misaligning the compressor within the amplifier system, i.e. by changing the grating distance. This is done quite easily with our laser system, as all Coherent lasers mount the compressor gratings on a translation stage. This translation stage can be adjusted by hand or by a stepper motor . In our system, it is thus possible to produce pulses with durations that range from 100 fs to 2 ps. We may then adjust the exact frequency difference between the two pumps by adjusting the time delay between them (such that one frequency of the pump overlaps with a different frequency in the other pump and matches the Raman shift) - this is shown schematically in Figure 2.4 (b). The entire experimental setup is depicted in Figure 2.4 (a). Furthermore, as mentioned earlier, with chirped pulses we may use higher power to generate the sidebands, increasing the power in the visible part of the bandwidth without reaching the threshold where parasitic processes dominate.

We use Table 2.1 to choose the best experimental conditions (depending on desired pulse duration and Raman shift). In [11], these concepts are presented slightly differently and a simple equation relating the instantaneous difference in frequency between the pulses $\Delta\omega$ (which should be equal to the Raman shift ω_R in wavenumbers), time delay t (in femtoseconds), and chirp rate b (in fs $-$ cm^{-1}) is derived: $\Delta\omega = bt$.

Table 2.1: Exciting PbWO$_4$ Raman modes with linearly chirped pulses; empirically obtained best-working conditions for cascaded sideband generation in PbWO$_4$ [11]. The power in one pump is the same as the power in the other. The Raman process is very sensitive to phase-matching angle and time delay; this table should be followed as closely as possible when exciting a particular Raman mode. Adapted from [1].

Raman Mode	Power in One Pump Beam	Phase-Matching Angle	Chirp Rate (b)
191 cm^{-1}	7.5 mW	1°	2100 cm^{-1}/ps
325 cm^{-1}	2-3 mW	2.5°	2100 cm^{-1}/ps
903 cm^{-1}	10 mW	4°	620 cm^{-1}/ps

For this particular experiment, we used pulses of around 200 fs to excite the PbWO$_4$ Raman mode of 325 cm^{-1}. We retrieved the precise chirp using a second harmonic FROG setup, with software provided by Rick Trebino [24]. However, we took care to optimize the chirp to produce the best experimental results. The original 800 nm beam was split into pump and Stokes beams by a non-polarizing beamsplitter. We adjusted the power in each beam with separate neutral density filters and observed the behavior of the sidebands. By tuning the power we were able to reduce nonlinear parasitic effects and thus optimize the quality of the sidebands. Finally, after either one or both beams are spatially modulated, they are focused (by separate 50 cm lenses) and recombined at a small angle (3.16 degrees, to satisfy phase matching conditions) in a 0.5 mm single-crystal lead tungstate (MTI Corporation, PbWO4-101005S2, 128$).

This crystal was placed 2.5 cm before the focus, resulting in a beam diameter of about 1 mm. This distance ensures that the intensity is low enough that parasitic effects (such as self-phase modulation) do not dominate over the Raman generation. There was much careful experimentation concerning this distance, and we empirically found that distances closer to the focus resulted in almost complete loss or distortion of the Raman sidebands. **If this happens to any future students, place your crystal FURTHER FROM THE FOCUS.**

For positive chirp (which is what we used for all results given here), the pump pulse propagates without delay (see inset to Fig. 3.1) and the time delay of Stokes pulse can be adjusted to excite the
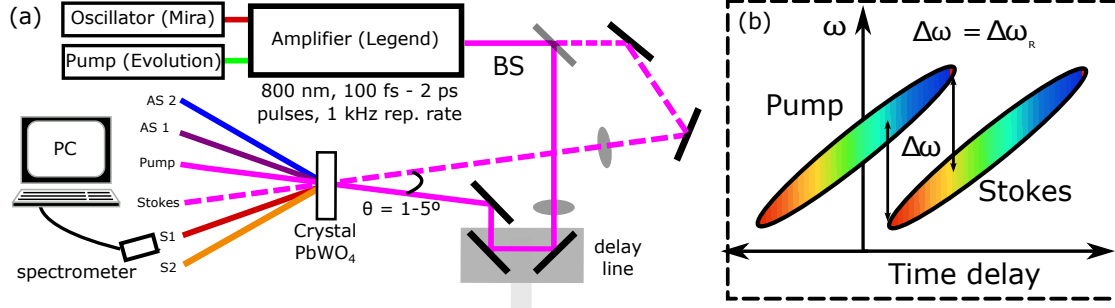
Figure 2.4: (a) Schematic of the experimental setup. "BS" stands for a 50/50 beamsplitter. The dashed line is to help separate the two pumps from each other although one is a time-delayed copy of the other. (b) A schematic depiction of the two chirped pulses used in the experiment and the delay between them. Adapted from [1].

particular Raman mode (325 cm^{-1} in our case). A standard set of sidebands thus generated is also shown in Fig. 3.1(a). We label the sidebands as anti-Stokes One (AS1), anti-Stokes Two (AS2), and so on.

2.2.4 Setup and Methods

Our experimental setup is shown in Fig. 2.5. We used the aforementioned chirped pulse Raman setup but varied the setup to add the possiblitiy for spatial shaping of one or both beams.

A spatial light modulator (Hamamatsu x$10468 - 02$) was used for all spatial shaping of the beam. We optimized the phase masks (*i.e.* by adding a constant phase or multiplying by a constant) using a beam profiler (Spiricon SP620U) to produce beams which appear darkest in the center in the far field. We confirmed independently with an interferometric setup that these beams correspond to vortex beams that exhibit the proper behavior when interfered with Gaussian beams. These phase masks and examples of the beams thus produced are shown in Fig. 3.1. We performed two sets of experiments; for the first, we only spatially shaped one beam (so that the topological charge did not equal 0) and left the other as a Gaussian. Therefore, only one beam was input to the SLM and we were able to use the full size of the beam. For the second setup, we reduced the size of both beams by 25% with a telescope placed before the beamsplitter, so that the diffraction that results from the clipping of one beam on the SLM is avoided. The telescope was built with thin negative

21
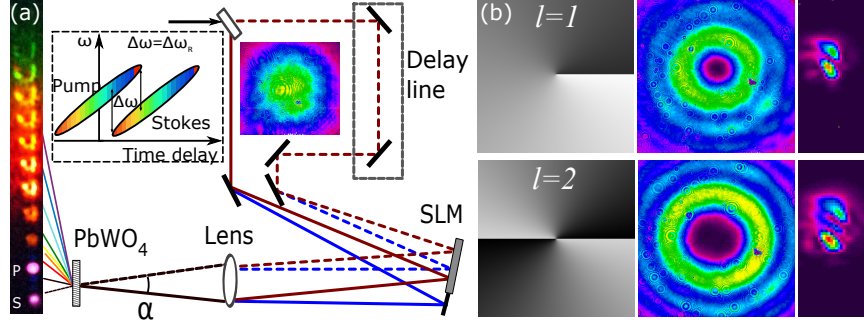
Figure 2.5: (a) Our experimental setup. Dashed lines correspond to pump beam, while solid lines correspond to Stokes. The blue lines correspond to the one-beam modulation case and the red lines correspond to the two-beam modulation case. The angle of the SLM is greatly exaggerated. Typical sidebands produced from this arrangement are also shown. The inset schematically depicts our two chirped pulses and the delay between them. (b) Computer generated phase masks (left), optical vortices obtained with these phase masks just before the focusing lens, approximately 76 cm after the SLM (middle), and vortices focused with a tilted lens (right). Adapted from [4].

miniscus and plano-convex lenses to produce minimal spherical aberrations.

2.3   Results

As mentioned above, after generating a set of Raman vortex sidebands, the TC for each sideband was checked by focusing with a lens tilted by 6 degrees [77] and counting the number of spots in the focal plane. The number of observed spots is equal to $l_n + 1$. The spots form a titled row and the slope of this row corresponds to the sign of TC, such that positive slope corresponds to positive TC and vice versa. As shown by Figs. 2.6-2.8, our results confirm that higher order optical vortices (i.e. vortices generated by l_p and $l_s \neq 1$ or 0) follow the algebra given by Eq. (2.3).

2.3.1   Results for One Modulated Beam

This experiment was performed with six sets of TC values. We set l_p equal to zero for the whole experiment and $l_s = \pm 1; \pm 2; \pm 3$. We present our calculations for the topological charge of each set in Table 2.2.

As depicted in Fig. 2.6, the theory matches our experimental results.

We were able to generate up to 7 high quality vortices with $l_s = \pm 1$, without any background nonlinear processes and noise, and 15 vortices (up to blue wavelengths) at the maximum intensity
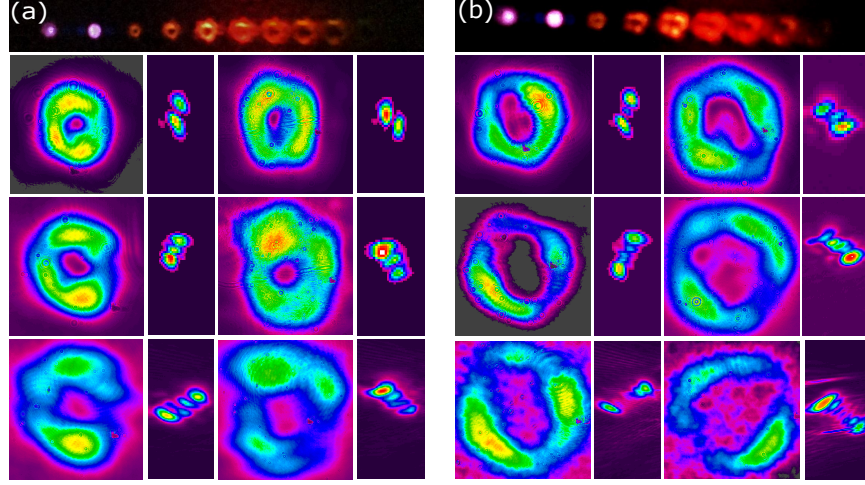
Figure 2.6: TC measurement of Raman sidebands using a tilted lens. For each block: columns 1 and 3 are the sidebands before the lens, Columns 2 and 4 are the sidebands after the lens. From top to bottom – AS1, AS2, AS3. Results are summarized in Table 2.2. (a) Left (right) two columns: sidebands generated with $l_p = 0$ and $l_s = -1$ ($l_s = 1$). (b) Left (right) two columns: sidebands generated with $l_p = 0$ and $l_s = -2$ ($l_s = 2$). Adapted from [4].

Table 2.2: Predicted, and measured, TC for (from top to bottom) $l_s = +1(-1)$, $l_s = +2(-2)$, and $l_s = +3(-3)$. In all cases, $l_p = 0$. Adapted from [4].

n	TC	Number and direction of spots
1	$-1(1)$	2 spots in the negative (positive) direction
2	$-2(2)$	3 spots in the negative (positive) direction
3	$-3(3)$	4 spots in the negative (positive) direction
1	$-2(2)$	3 spots in the negative (positive) direction
2	$-4(4)$	5 spots in the negative (positive) direction
3	$-6(6)$	7 spots in the negative (positive) direction
1	$-3(3)$	4 spots in the negative (positive) direction
2	$-6(6)$	7 spots in the negative (positive) direction
3	$-9(9)$	10 spots in the negative (positive) direction
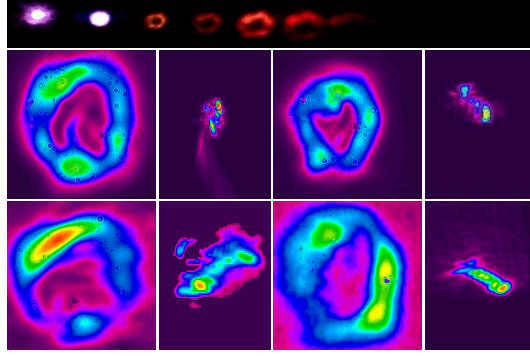
Figure 2.7: TC measurement of Raman sidebands using a tilted lens. Columns 1 and 3 are the sidebands before the lens, Columns 2 and 4 are the sidebands after the lens. Left (right) two columns: sidebands generated with $l_p = 0$ and $l_s = -3$ ($l_s = 3$). From top to bottom – AS1 (TC=± 3; 4 spots), AS2 (TC=± 6; 6 spots). Adapted from [4].

below the burning point of the crystal. However, the intensity of the vortices generated with $l_s = \pm 2$ and ± 3 is lower than for $l_s = \pm 1$. In addition, only 6 AS sidebands were generated for $l_s = \pm 2$ and 5 AS sidebands for $l_s = \pm 3$. We hypothesize that this is due to the increase in order and correspondingly the increase in the bright area of each vortex, as was shown in [78, 79] and can be seen in Fig. 3.1. Therefore, the peak intensity (at a fixed point) is smaller from order to order, impacting the Raman generation negatively. We can calculate by how much smaller it is using the equation for the bright area A_l of a Laguerre-Gauss beam of order l generated from a Gaussian beam of radius w_0 given in [79]. We have $A_l = \pi w_0^2 \sqrt{(l+1.3)^2 - l^2 e^{-1.4/l}}$, so the intensity of a $l = 2$ beam is 75% what it is for a $l = 1$ beam, and the intensity of a $l = 3$ beam is 83% what it is for a $l = 2$ beam. However, it is important to note that the question of Raman efficiency from order to order is quite complicated and is also be due to a wide variety of factors, such as spatial overlap and the increased divergence of higher order beams. Reduction in peak intensity is only the most obvious and most dramatic cause.

Finally, we checked the TC of the first three AS sidebands for $l_s = \pm 1$, ± 2 and the first two AS sidebands for $l_s = \pm 3$, as is shown in Figs. 2.6 and 2.7. Our measurements were limited by the resolution of the intensity distribution at the focus for each vortex; despite our use of loosely focusing lenses, we were unable to resolve the 10 spots theoretically predicted for AS3 of $l_s = \pm 3$.
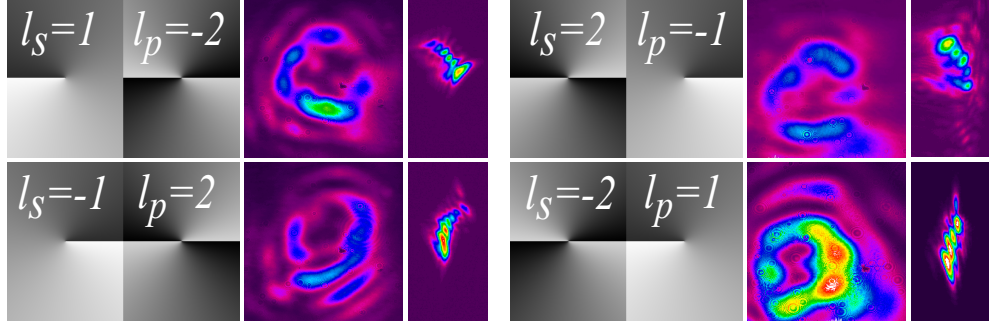
Figure 2.8: TC measurement of Raman sidebands using a tilted lens. For each block: digital phase maps for generating pump and Stokes beams (left), AS1 generated when these phase maps are applied (middle), AS1 focused with tilted lens (right). Adapted from [4].

Table 2.3: Predicted, and measured, TC for 4 different cases of mixed l_p and l_s. Adapted from [4].

l_s	l_p	TC of AS 1	Number and direction of spots
1	-2	-5	6 spots in the negative direction
-1	2	5	6 spots in the positive direction
-2	1	4	5 spots in the positive direction
2	-1	-4	5 spots in the negative direction

2.3.2   Results for Two Modulated Beams

In this experiment, we tested 4 different combinations of TC of input beams but kept the difference $|l_p - l_s|$ equal to 3. To confirm that the topological charge transfer took place, even for such a relatively large value of $|l_p - l_s|$, we measured the resultant TC of AS1. From Eq. (2.3), we predict the results shown in Table 2.3.

As depicted in Fig. 2.8, Eq. (2.3) correctly predicts the results in all 4 cases. The sidebands generated in this experiment are worse in quality (have diffraction fringes and are not complete donut shapes) and efficiency (they are barely seen by eye) than sidebands generated with one modulated beam. Our experience has shown that small changes (such as any coma introduced by lenses) from ideal spatial alignment can add a significant amount of distortion to Raman-generated beams. This issue is especially relevant for Raman-generated vortices, as any distortions in the

beam profile reflect distortions in the carried OAM.

2.4 Conclusions and Extended Work

In this section we have produced multi-color optical vortices in Raman sideband generation with two fem- tosecond linearly chirped pulses, verified the TC algebra, and used a single SLM to shape two beams.

This work resulted in further research into how superpositions of vortex states can be measured with the tilted lens method [80]. Experiments and simulations were led by M. Shutova. We investigated two different cases: when coherent interference (or addition) between components is present and when it is absent (incoherent addition). We discover that this technique is suitable for measuring the TC of the dominant component of a mixed state.

3. SPATIALLY TAILORED BEAMS FOR CUSTOM SUPERCONTINUUM GENERATION

3.1   Introduction

Stable broadband sources[*] are essential for a variety of applications, from spectroscopy [81] to imaging [82] and nonlinear optical parametric amplifiers [83]. Supercontinuum (also known as white light) generation offers a promising tool for these multidisciplinary uses. Sapphire is regarded as the crystal of choice for visible supercontinuum generation [84] and is the focus of our particular study. The important material properties of sapphire as used to guide our experiments and simulations are shown in Table 3.1.

Supercontinua are generated in sapphire through the process of single filamentation. This general process encompasses a wide variety of linear and nonlinear effects including self-steepening, self-phase modulation, dispersion, four-wave mixing, Raman excitation, second and third harmonic generation, and plasma generation, absorption, and refraction [85]. Since in the most general case it is difficult to separate the exact contribution of each of these, individual optimization of each effect is neither particularly feasible nor extremely desirable. However, each of these effects can be highly influenced by the spatial distribution of the beam – one of the most basic effects of spatial shaping is to focus the beam tighter, thereby enhancing plasma excitation and influencing the resultant spectrum. Previous studies with spatial shaping have included work with Bessel [86] and Laguerre-Gauss beams [87]. However, these failed to find significant spectral deviations or improvements in efficiency from the Gaussian regime. Systematic spatial optimization has not been performed.

Previous work that has shown promise in this direction includes a study performed with microlenses generated via spatial light modulators [88]. Moreover, there have been several successful studies of spectral pump-beam optimization in filamentation [89, 90] and other effects, such as the wavefront-shaping control of second harmonic generation [91] and the enhancement of sponta-

---

[*]This chapter is derived in part from an article published in *Journal of Modern Optics* on Aug. 30, 2017 (copyright Taylor & Francis), available online: `http://www.tandfonline.com/10.1080/09500340.2017.1366566` [5].

Table 3.1: Properties of sapphire that will be used throughout the chapter.

Sapphire (Al_2O_3) Facts	
Space Group	D_{3d}^6 - $R3C$
Optical Transparency	0.18 - 4.5 μm
Density	3.98 g/cm^3 or 2.2 $\times 10^{28}$ atoms/m^3
Crystal Type	Negative Uniaxial: $n_o > n_e$
Bandgap	9 eV
Main Raman Modes, ν_R	379.6, 418 cm^{-1}

neous Raman signals through a turbid medium [92]. We extend these results and methods to the theoretically challenging regime of supercontinuum generation by using a wavefront shaping algorithm to influence the supercontinuum spectrum. This chapter will explore this effect. Section 3.3 covers preliminary experimental results that set the basis for the results in Section 3.5.

There are several aspects of interest here, including the physics of filamentation and drawing attention to the potential of non-Gaussian beams. Further commercial applications are also possible. This work will lead to universally stronger seeds for spectroscopic applications that depend on nonlinear effects for a large signal-to-noise ratio. Our preliminary results are a "proof-of-concept" that the idea of spatial optimization has merit and should be further expanded with additional work.

3.2 Experimental Methods

3.2.1 Experimental Setup

The experimental setup is depicted in Fig. 3.1. We used a Ti:Sapphire regenerative amplifier (Coherent, Legend) to produce infrared ($\lambda = 802$ nm) 35 fs pulses with a 1 kHz repetition rate and 4 W average power that we attenuated to produce a supercontinuum. We then investigated two regimes of supercontinuum generation: chirped and unchirped. In the first case, we added a positive chirp by changing the grating distance within the compressor unit of the amplifier. This produced pulses of 900 fs FWHM duration, measured using a commercial autocorrelator (Pulse Check; A.P.E.; Berlin, Germany).
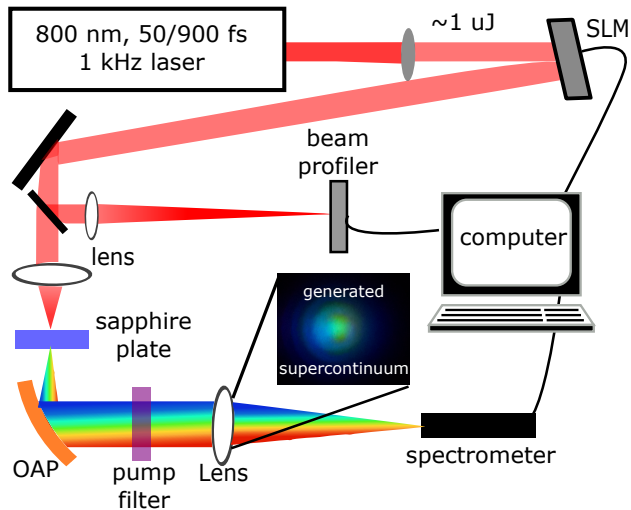
Figure 3.1: Setup for generating supercontinua from shaped pulses; a photograph of the generated supercontinuum is shown in the inset. The angle of the spatial light modulator (SLM) is greatly exaggerated. OAP stands for off-axis parabola and was used to collimate the supercontinuum spectrum after the crystal. Adapted from [5].

Different powers/pulse were needed to produce supercontinua in each regime: we used $5-6$ μJ in the chirped and 1 μJ in the unchirped cases, giving a peak power of roughly 10 MW for both cases. In both cases, we are operating at $5\times$ the critical power of self-focusing, P_{cr}:

$$P_{cr} = \alpha \frac{\lambda}{4\pi n_0 n_2} \tag{3.1}$$

Where, in our case, $\lambda = 800 \times 10^{-9}$ m, α is a constant which depends on the initial spatial distribution of the beam and has been found to be 1.8962 for Gaussian beams [93], n_0 is the linear refractive index and is equal to 1.7602 for sapphire at 800 nm, and n_2 is the nonlinear refractive index and is equal to 3×10^{-20} m^2/W for sapphire at 800 nm [94, 95]. Hence, we find that $P_{cr} = 1.98$ MW. Despite the fact that we are operating at several times the critical power, numerous studies have shown that operating at lower powers results in unstable or weak supercontinua [84].

In both regimes, we used a spatial phase-only light modulator (Hamamatsu; x10468; abbreviated SLM) to shape the originally Gaussian beam. The beam has a $9-10$ mm diameter at $1/e^2$ intensity prior to being shaped by the SLM; this is the greatest we could expand the beam without

clipping on the SLM screen. We then split the beam and focused part of it with a 5 cm focal length lens to generate a supercontinuum in a 3 mm thick single crystal c-cut sapphire plate (Newlight Photonics; SAP0030-C; Toronto, ON). The resultant diverging supercontinuum was collimated by an off-axis paraboloic mirror with a reflective focal length of 100 mm. The pump beam was then filtered out via a 750 nm short pass filter (Semrock; FF01-745/SP-25; Rochester, NY). The filtered beam was subsequently refocused with a 20 cm focal length lens into a multi-mode 600 μm core fiber. Since the supercontinuum light should roughly focus to 5 μm, the fiber core is of sufficient size to collect all the light and not be affected by any spatial phase changes the SLM adds. We checked this assumption by translating the fiber in $x - y$ dimensions in the focal plane; this operation revealed no unmeasured light. Hence, we are confident that the optimization program is not optimizing the light-collection system.

The other part of the beam was sent through a long (2 m focal length) lens to be very loosely focused onto a CCD array (Spiricon; SP620U) and recorded by the computer. These images did not take part in the spatial optimization – they are there to help visualize the effect of different phase maps on the beam's spatial profile in the focus.

3.2.2   Optimization Details

For all optimization regimes, we used a variation of the continuous sequential algorithm (abbreviated VCSA) [96, 97]. The VCSA groups pixels on the SLM together and cycles through 2π phase values in 8 steps. The algorithm then compares spectrometer output in a particular spectral range before and after adding different phase values. If the average of the spectrometer reading in that spectral range improves, then the algorithm keeps the phase value. This cycle is repeated three times and the results averaged to minimize influence from shot-to-shot fluctuations and other noise. The algorithm then moves on to another pixel group and repeats the process. Each iteration takes 12 seconds, with the spectrometer integration time forming the largest limit on speed.

For all results given in this paper, we employed the "spiral out" method of this algorithm, which starts with large pixel groups (of 264×300 pixels) in the center of the SLM and spirals out to the edges, as in Figure 3.2. It then starts a new stage at the center with smaller pixel

SLM Screen Divided into Pixel Blocks

Block Color:

Added Phase: 0 $\frac{2\pi}{7}$ $\frac{4\pi}{7}$ $\frac{6\pi}{7}$ $\frac{8\pi}{7}$ $\frac{10\pi}{7}$ $\frac{12\pi}{7}$ 2π

Algorithm - Stage 1   Algorithm - Stage 2...
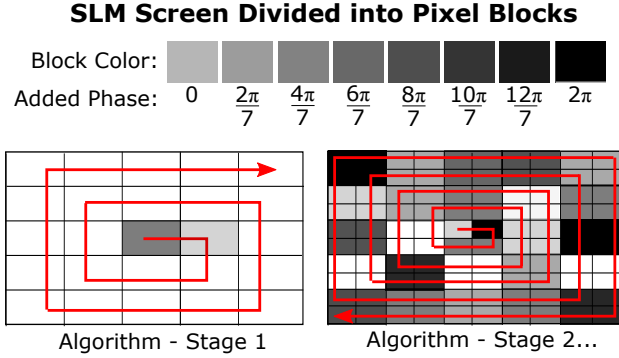
Figure 3.2: A schematic depiction of the algorithm's path in optimizing the spatial mask for our experiment. A full description of the program's workings is given in Section 3.2.2. The smaller the block the longer the program takes to finish; the process can be stopped at any time if the user is satisfied with the result. Our SLM is comprised of 792×600 pixels total. Adapted from [5].

groups (of 132×150 pixels) and spirals out until it is forced to repeat itself with even smaller groups of pixels (of 72×60). The final run consists of groups of 24×24 pixels. In total, we let the algorithm optimize for roughly half an hour for the results given in this dissertation. We do not consider optimization time to be a major limit in our experiment, as there are no discernible differences between spectra taken at the beginning of the day and those taken at the end. Further, for spectroscopic applications, it will not be necessary to quickly reoptimize the masks so long as the user takes care to produce a bank of working masks that they may easily switch between.

3.2.2.1 A Note on Convergence and Repeatability

By and large, the algorithm was able to make immediate and substantial improvements to the signal. Whenever the algorithm had troubles optimizing, it was largely due to some error in the system. These errors included bad (i.e. significant) chirp, lens tilt, or misalignment of the crystal in the focus of the pulse. In one case, we found that we had trouble with algorithm convergence due to the fact that the laser had burned a hole in the polarizer we were using as part of a polarizer-HWP combination to reduce the power!

Repeatability was also difficult to confirm experimentally. We often obtained the best masks after ≈ 30 minutes of algorithmic optimization, and so were unwilling to waste valuable experimental time on repeating the same set of optimization and focusing conditions. Further, we often

inadvertently were able to repeat experiments among a range of optimization conditions (we found several filament interference and tilted SC conditions). We were encouraged by this to try many new conditions, rather than repeating the old ones. The hope is that we will be able to return to this experiment and make a more systematic study of the repeatability and what changes might occur over time.

3.3 Results

3.3.1 Results for Highly Chirped Pulses

Using these methods, we were able to obtain a general 10% broadening of the spectral width of the supercontinuum generation for highly positively chirped pulses (900 fs), as shown in Fig. 3.3. However, this regime is tricky to work with as the damage threshold for these focusing conditions in sapphire is near the critical power of self-focusing. This leads to multiple issues including stability and repeatability, making further optimization difficult. For comparison, these results took 5-6 optimization runs each to obtain; in most runs, the algorithm would result in a burn on the sapphire.

Although there is the potential for further improvements under less intense focusing conditions, this possibility is not explored in this experimental iteration. We feel that these results may still be applicable to areas where users are restricted to using these sorts of highly chirped pulses. We have also not explored the possibility of removing the chirp and using FTL-limited (but long) pulses, as we wished to keep the setup simple. The compressor grating distance within the amplifier is changed very simply to produce highly chirped pulses – more complicated pulse shaping techniques would be required to test FTL-limited, long pulses.

3.3.2 Results for FTL Pulses

3.3.2.1 Tuning SC Peaks

For 35 fs unchirped pulses, we discovered that it is possible to shift the supercontinuum spectral cutoff peak between 450 and 650 nm, as our preliminary results indicate in Figure 3.4. The region from 450–500 nm is completely absent in the supercontinuum spectrum generated without any
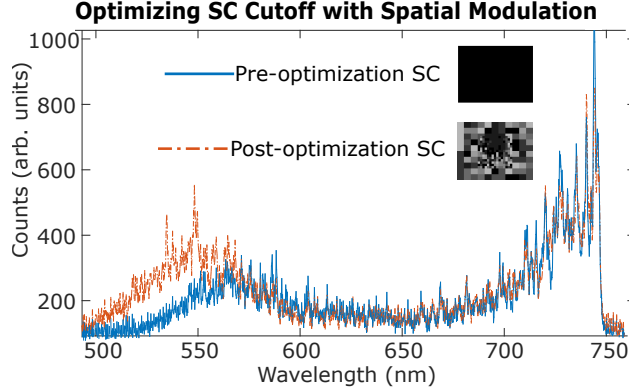
Figure 3.3: The supercontinuum spectrum before (blue line) and after (red line, dash-dot) spatially optimizing the pump pulse. The range of optimization was 500–550 nm. Adapted from [5].

phase mask applied and so represents a significant broadening ($> \approx 20\%$). In this case, the effect of the added phase mask on the supercontinuum spectrum is easily noticeable by eye and hence can not be due to any limitations in our light-collection system.

Further, the phase masks shown in Figure 3.4 generate the same spectrum from day-to-day without any special additional environmental control, making our experiment repeatable in a variety of conditions. However, the spatial profile of the shaped beam is very sensitive to the alignment of the pump beam on the SLM screen. This is because any displacement in this region will result in different parts of the beam obtaining different phase values, and hence not reproducing the original phase-optimized beam. In this case, each phase mask will need to be re-optimized to obtain a tailored spectrum.

3.3.2.2 Interfering Filaments

For some regimes of optimization, most notably on the lower frequency end (500–650 nm), the SLM of its on accord split the originally single Gaussian beam into two, more or less, Gaussian beams that then interfered with each other. This inadvertently recreated the results of Cook, et al. [98] who generated a pair of filaments by focusing a Gaussian beam with a cylindrical lens. This was a landmark result for its time, as it showed that filaments are very much mutually coherent. Our results are significant in this light as it shows that the SLM does not destroy this coherence.

33
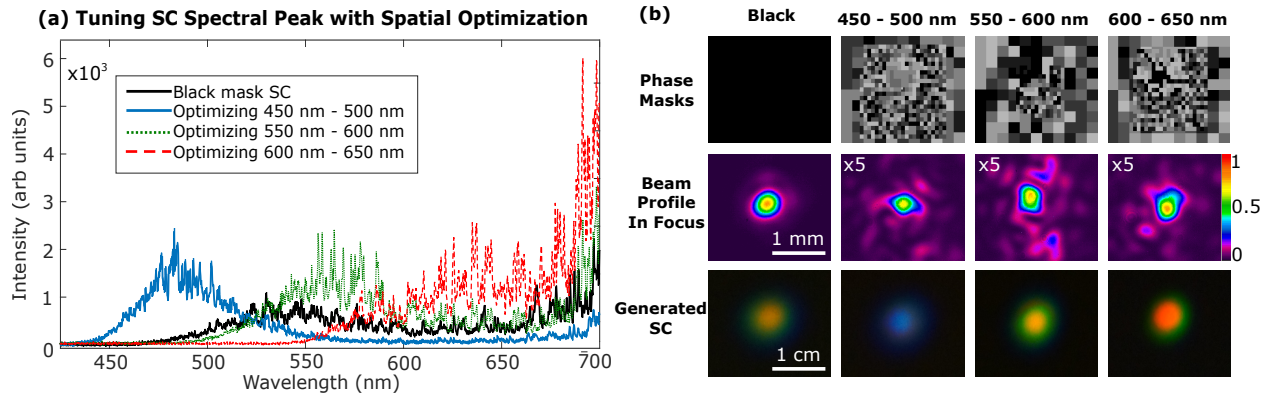
Figure 3.4: (a) Measured supercontinuum spectrum for different optimization regimes – the SC cutoff peak is spectrally shifted as the spatial shape changes. Each entry in the legend corresponds to the optimization range of that particular run of the algorithm (i.e. for the second entry, the algorithm attempts to optimize the average spectrometer-measured counts in the range of 450–500 nm). All spectra were taken with the phase masks and profiles in (b). (b) SLM phase masks (top); beam profiles in the focus magnified approximately 40 times and with the left three profiles integrated 5x longer than the right-most profile (middle); true-color photographs of the resultant supercontinuum scattered off of a business card (bottom; taken with a DSLR camera [Sony $\alpha 37$] for different optimization regimes). Adapted from [5].

Much like the results in Section 3.3.2.1, the results in this section were generated with very little human input. We set the Labview algorithm to maximize the average spectrometer signal in the regions of 550–600 and 600–650 nm. If the crystal is placed slightly (0.1 mm) out of the foucs, the alogirthm gave us these interfering filaments. Given that similar results have already been published (albeit without the involvement of an SLM), we decided not to pursue or publish these results.

3.3.2.3 Tilted Lenses

Testing a hypothesis that the SLM was simply correcting for lens tilt or other experimental imperfections, we purposefully tilted the focusing lens in Fig. 3.1 and attempted to reoptimize the results in Section 3.3.2.1.

This, rather than correcting for the tilt of the lens, resulted in the algorithm attempting to exploit the tilt by producing a tilted supercontinuum, as can be clearly seen in Fig. 3.6. In other words, the various main spectral components of the supercontinuum are not collinear with each other.
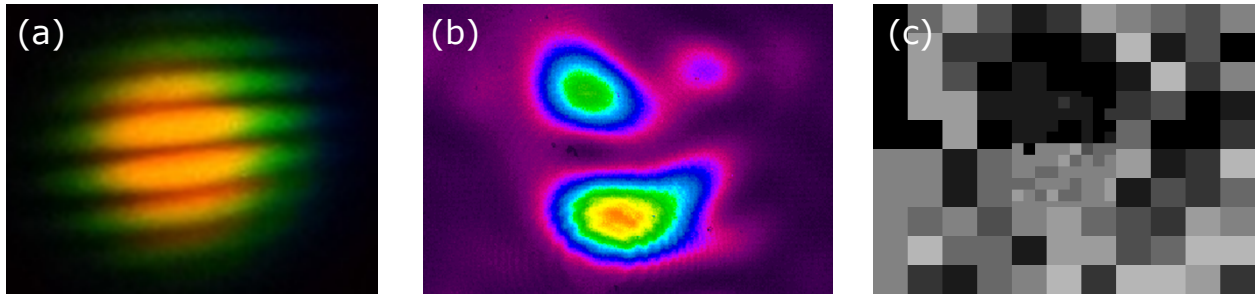
Figure 3.5: (a) True-color photograph of supercontinuum fringes generated via interference from a pair of filaments, taken with a DSLR camera [Sony α37]. (b) Focused beam profile of the beam generating two filaments. (c) Phase map generated as a result of 550–600 nm optimization. When applied to a Gaussian beam, we generate the profile in (b).
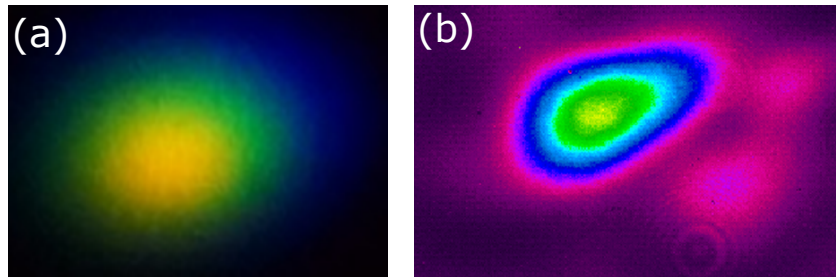
Figure 3.6: (a) True-color photograph of a "tilted" supercontinuum, as generated through a tilted focusing lens, taken with a DSLR camera [Sony α37]. (b) Focused beam profile of the beam generating a tilted supercontinuum, also visibly non-Gaussian.

This effect could be due to how the supercontinuum focused into the spectrometer, and hence how the tilt affected the signal. In this example, we were attempting to optimize 550–600, and so the SLM could have been simply optimizing how yellow/green focus into the spectrometer while removing blue from the focus. We repeated this experiment for other optimization regimes and obtained similar results; the optimized spectral components formed the center of the SC, while the undesired components were tilted to the side.

Unfortunately, our setup did not allow us to explore whether this was truly the cause of the supercontinuum tilt or not. It did, however, serve as a valuable check for the alignment of our system. If the lens was tilted, the alogrithm would exagerrate this tilt. It also showed that the algorithm was not merely correcting for rough alignment problems.

3.4 Simulation Methods

All results in this section are based on an open-source filamentation package in C++ developed by P. Zhokhov in [99, 100]. My role in this section was to apply the package to our results and open-source the original code (see our github, `pzhokhov/gsolver` or `Sokolab/gsolver`), as well as put together a team that will continue this work (see David Fernandez' work). All simulations were performed on the Ada and Curie clusters of the Texas A& M High-Performance Research Computing Center.

The main goal of the package is to solve the generalized nonlinear Schrodinger equation for the evoltion of the complex scalar field amplitude, labelled either $A = A(t, r, z)$ or $A = A(t, x, y, z)$. While this package is able to handle full t, x, y, z simulations, our initial work focused on axially symmetric beams and phase masks, represented by t, r, z simulations. These are computationally much less intensive than the full 3D treatment, and so allowed us to quickly determine how the parameters in the simulation package mapped to our experimental configuration.

Hence, the axially symmetric equation for the complex scalar field amplitude evolution, $A = A(t, r, z)$, is written as [101]:

$$\frac{\partial A(\omega)}{\partial z} = i \left[D(\omega) + \frac{i\Delta_{\perp}^2}{2k(\omega)} \right] A(\omega) + R_{NL} + R_{pl} \tag{3.2}$$

Where $D(\omega)$ is the dispersion, ω is the radiation frequency, $k(\omega) = \frac{\omega}{c}n(\omega)$, c is the speed of light in vacuum, $n(\omega)$ is the frequency-dependent linear refractive index, z is the propagation coordinate, R_{NL} is a seperate equation describing the nonlinear-optical response, and R_{pl} is a separate equation describing the photoionization response. Equataion 3.2 can be derived from Maxwell's equations by making use of the unidirectional pulse propagation envelope (UPPE) approximation [102, 103]. Further details are available in Section 2 of [100].

3.5 Simulation Results

We began by comparing the simulated losses in the single-filamentation regime in fused silica with the results of Sudrie, et al. in [6]. This was to ensure that we understood how our simulation
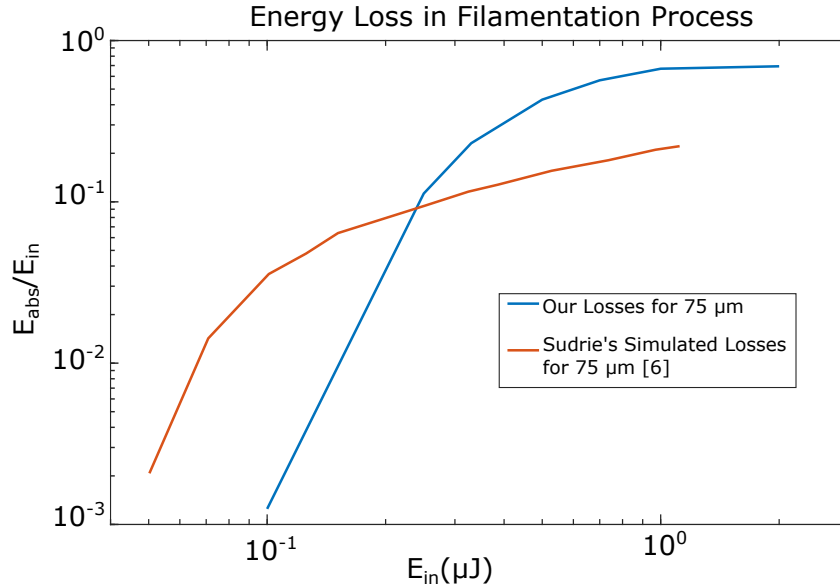
Figure 3.7: Comparing simulated energy losses in filamentation in fused silica. Sudrie's losses are taken from [6], numbers identical to theirs are used wherever relevant (i.e. density, power, bandgap).

package worked and were able to reproduce previously explored regimes. Initial plots were not particularly accurate, as shown in Fig. 3.7, where our losses are $5\times$ higher than theirs for all values of E_{in}.

We hypothesize that this is due to a variety of artifacts resulting from too-tight focusing and a too-small radial grid. Examples of these artifacts are shown in Fig. 3.8, where a good example of an electric field on axis plot is shown and compared with a bad example of an electric field on axis plot. These sorts of plots are easy ways to see filamentation dynamics at a glance and confirm proper (or improper) initial conditions.

We are currently in the process of rerunning simulations with increased radial and propagation grids to study the losses in their proper regime. However, the trend of the losses in Fig. 3.7 seems identical, which is promising for future work.

Once we have finished this initial stage, we will move onto adjusting the spatial phase of $A(\omega)$ and examining the effects of different phase masks on the resultant filament spectrum. We will adapt optimization code written by Jonathon Thompson in [104] to fully simulate the optimization
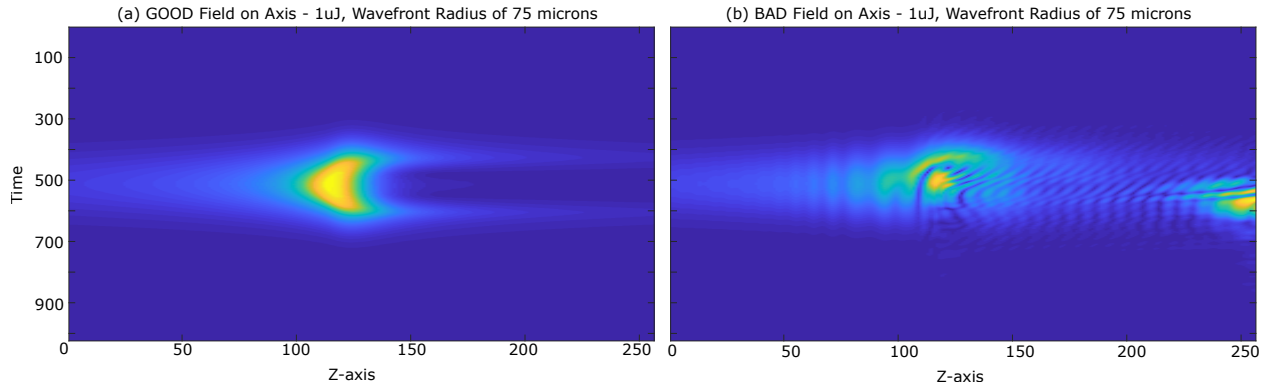
Figure 3.8: Electric field on the beam axis as a function of z for a typical filamentation process at $1\,\mu J$. While (a) correctly reproduces the pulse-splitting behaviour that is common in such regimes [7], (b) has a number of very strange artifacts, including ripples and distortions. While both simulations had the same grid size, (b) was run with parameters suggesting a higher atomic density, showing that there is no "one size fits all" way to run a filamentation simulation.

process of the SLM on the supercontinuum spectrum.

3.6 Conclusions

Our preliminary results in this section indicate that spatial beam shaping has substantial untapped potential for optimizing supercontinuum generation by enhancing a particular spectral region. We envision that this technique can dramatically improve the ability to tailor the supercontinuum spectrum for any particular application. For example,we can provide significantly stronger seed pulses for optical parametric amplifiers and substantially enhance signals in broadband coherent anti-Stokes Raman (CARS) spectroscopy/microscopy. An SLM provides a much more flexible platform, as compared to a microstructured fiber, to tailor the spectral properties of the supercontinuum [105]. The user will simply load the SLM with the phase mask for the particular spectral range they desire. By pre-generating optimal phase masks, the frequency can be tuned at the 10 Hz refresh rate of the SLM. In the future, we envision that this will lead to higher available powers for various nonlinear spectroscopy experiments and hence a greater signal-to-noise, paving the way for precision measurements.

Further work will likely elucidate the theoretical foundation behind this effect, as well as allow us to make predictions for the effectiveness of our technique in various spectral regions.

4. COHERENT SYNTHESIS AND CHARACTERIZATION OF RAMAN-ENABLED ULTRAFAST WAVEFORMS

4.1 Introduction

In the past, individual control of the full power of each Raman-produced sideband was limited as we used devices that were either power limited (such as the Dazzler) or did not allow full individual sideband control (such as the deformable mirror scheme). Both of these options have been described extensively in Section 1. For the current scheme, we make use of dichroic mirrors for recombination and sub-cycle controllable stages for phase control.

4.2 Setup

4.2.1 Experimental Schematic and Description

The full experiental setup is illustrated in Figure 4.2. A true-color image of the sidebands taken just after the diamond crystal is shown in Fig. 4.1. Details concerning parts and part numbers for each band are summarized in Table 4.1.

As described in detail in Section 1.3.1 and 1.3.2, we use the second harmonic of the idler out of the OPA (OPerA) at 870 nm and the main laser line at 800 nm. The frequency difference between these matches the 1332 cm^{-1} Raman line of a 0.5 mm thick, single-crystal diamond (Element Six 145-500-0385, 595$). We combine the two beams at a $\approx 3°$ angle, focusing each individually with a 50 cm lens (Stokes) and a 30 cm lens (pump). The Stokes beam profile is neatened with an iris
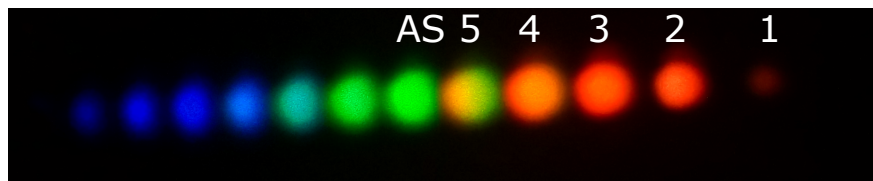
Figure 4.1: True-color image of sidebands used for experiments in this chapter. 12 sidebands are clearly produced, making our eventual goal of expanding this setup to AS 8 in order to produce single-cycle pulses fully realistic.
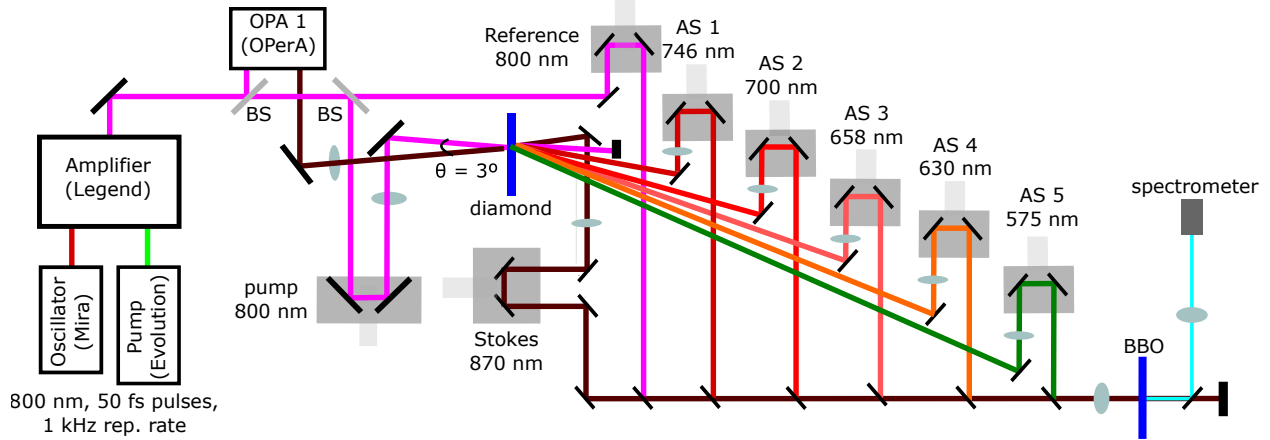
Figure 4.2: Our experimental setup to synthesize a sub-5-fs FWHM pulse. "BS" stands for 50/50 beamsplitter. For convenience, there is an extra delay stage for Stokes before it is sent to the diamond crystal to produce Raman sidebands. This stage is not technically necessary, but it makes it much easier to find temporal overlap between pump/Stokes in the diamond. While a dichroic mirror is shown to separate the fundamentals from their nonlinear signals at the end of the setup, this dichroic is only used for the results in Section 4.3.1. For Section 4.3.2, several Thorlabs UV filters are used instead (part numbers are listed in the text).

prior to focusing. The power of each beam is 18.28 mW (pump) and 1.86 mW (Stokes). After the diamond, pump is left with 10.78 mW of power, resulting in an efficiency of 40%.

This configuration produces many orders of Anti-Stokes (AS) Raman sidebands. These sidebands are essentially frequency-shifted copies of the original femtosecond pulses. After exiting the crystal, each sideband is individually collimated. This is necessary as, without collimation, the sidebands will diverge and it will be impossible to focus all bands in the same focal point upon recombination. Collimation is a difficult task as each band is spatially very close to each other and the beam divergence goes up with the sideband order. Proper combinations of lenses were largely found through trial and error, as some combinations were impossible to implement without running into experimental difficulties (i.e. a lens would end up impeding complete delay stage motion). Wherever possible, thin lenses were used to avoid adding substantial dispersion.

After collimation, each band is aligned to a separate delay line to allow for full control of phase and flexibility of position. We then used dichroic mirrors to Fourier synthesize each beam

together. After dichroic recombination, we used a single achromatic doublet (Thorlabs AC254-100-B-ML) to focus the beams into a 10 micron beta-barium-borate (BBO) crystal (Newlight Photonics BTC5001-SHG800(I)-P, 959$) to characterize the resultant pulse. A 1 mm BBO crystal (Newlight Photonics, BTC5100-SHG800(I)-P, 399$) was used for rough visual alignment of the pulses, as it produces a stronger signal. The full alignment procedure is described in Appendix A. Each BBO is housed in a rotation mount (Thorlabs RSP1) to allow us to rotate the crystal for phase-matching – maximum SHG/SFG signals for each frequency are optimally matched at different rotation angles in the BBO.

We initially used Zemax simulations to determine whether an off-the-shelf doublet would work better than a custom-made one. After some experimentation, we found that we can just as easily optimize the focal alignment of all beams by tweaking the placement of the collimating lenses and that a custom lens was unnecessary.

Each dichroic mirror potentially adds dispersion to either the band that is reflected or the bands that are transmitted. This is not particularly avoidable, as there were very few companies at the time of this thesis-writing that provided catalog dichroic mirrors in the necessary range. While it is likely possible to commission custom dichroic mirrors, we wished to keep the costs of this setup as low as possible. GDD graphs given by Semrock match fairly well with experimentally characterized dispersion.

To examine the interference of Stokes/Reference/AS 1, a single UV bandpass filter was used (Thorlabs FGB25). To examine the interference of the other bands (i.e. the higher frequencies of AS 2-4), an additional UV bandpass filter (Thorlabs FGUV11) was used to reduce the background from the main bands.

4.2.2 Sideband Properties

In order to determine the properties of the final synthesized pulse, it is first necessary to characterize each Raman sideband. This has not been done prior to this work. The spectra of all recombined sidebands, taken at the location of the BBO crystal in Fig. 4.2 in a single spectrometer scan, is shown in Fig. 4.3. In order to synthesize a single cycle pulse, we would have to extend the

Table 4.1: Parts to construct the Raman synthesis project and produce ≈ 5 fs pulses (with proper alignment). DC stands for "dichroic" – all DC mirrors were bought from Semrock. However, in the second set of data, the Semrock mirror used for Reference was replaced with one purchased from Edmund Optics (69-895).

Sideband #	Delay stage part #	Collimating lens(es)	DC mirror part #
Stokes	Newport 423 series	50 cm	N/A
Reference	Thorlabs LNR25ZFS	N/A	Di02-R830
AS 1	Newport GTS150	40 cm	FF776-Di01
AS 2	Newport 443 series/Thorlabs PAS005	15 cm & -10 cm	FF735-Di02
AS 3	Thorlabs LNR25ZFS	25 cm & -10 cm	FF685-Di02
AS 4	Newport 423 series	30 cm & -10 cm	Di03-R635-t1
AS 5	Newport 433 series	40 cm & -30 cm	FF605-Di02

bandwidth to 435 nm, or to AS 8. This is fully possible with the current setup, although scaling up intensities prior to this step will make finding overlap between higher order sidebands much easier. This is because the easiest and primary way for finding overlap between the pulses is via observation of the UV SFG signal corresponding to the nonlinear interaction between Reference + AS n, where n corresponds to the sideband order (i.e. $n = 1$ corresponds to AS 1). The full alignment procedure is described in Appendix A.

The maximum power of each sideband is recorded in Table 4.2. The power in Reference, Stokes, and AS 1 (the most intense beams) was measured using a Coherent FieldMax II power meter and PS10 head. The power in all other beams (unmeasureable with the first head, which is only good for > 500 nJ) was measured using an Ophir Vega meter and PD10-pj-C head. These are not the powers used for the final pulse synthesis, as in order for the Fourier synthesis to work, each band must match the power of the least intense sideband. Hence, for the final synthesis, each band is reduced by ND filters to ≈ 4 nJ for Section 4.3.1 and ≈ 6 nJ for Section 4.3.2.

4.2.2.1   *Sideband Pulse Characterization – SHG FROG and XFROG*

We used the XFROG technique [24] to retrieve the pulse shape of each sideband. The essence of the XFROG technique is to retrieve the shape of a weak, unknown pulse with a strong, known
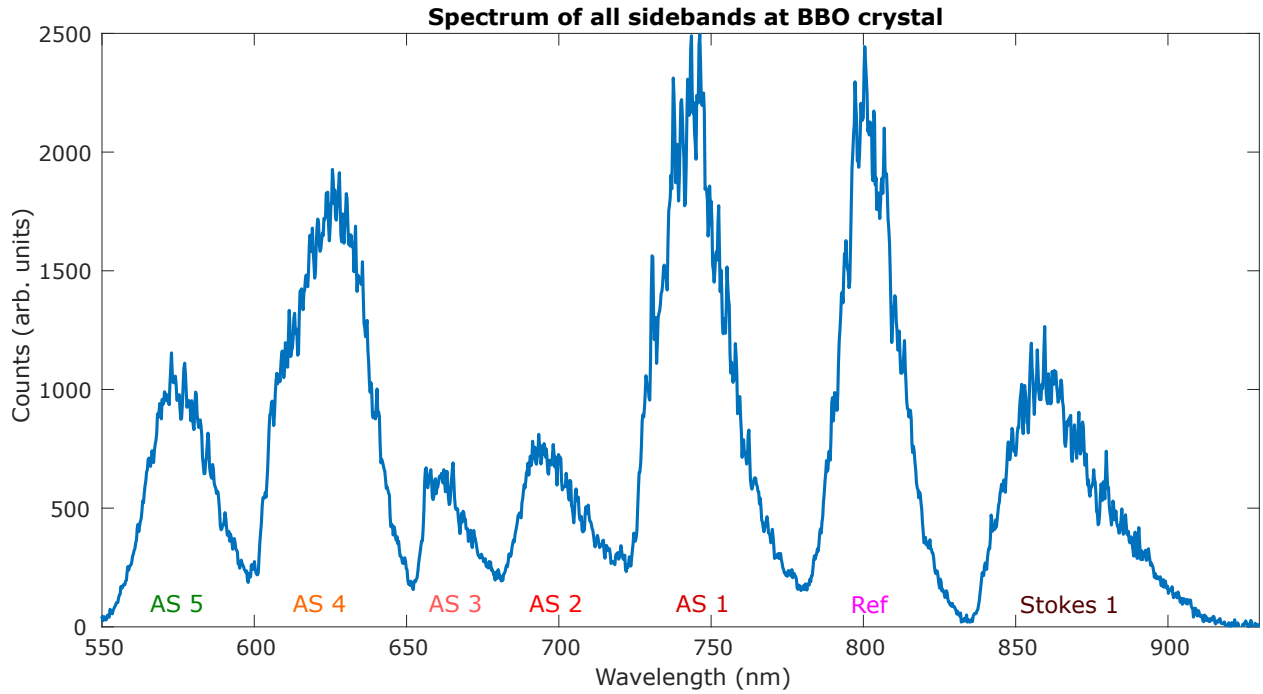
Figure 4.3: The combined spectrum of our sub-5-fs pulse, spanning from AS 5 to Stokes 1 (≈ 350 nm of bandwidth). Some bands are obviously artificially reduced by their dichroics, as is consistent with their retrieved pulse shapes in Figs. 4.7 and 4.12.

Table 4.2: Maximum power of each sideband, recorded at various locations in the setup.

Sideband #	Power after diamond	Power before DC mirror	Power after all mirrors
Stokes	1580 nJ (1.58 mW)	500 nJ (0.5 mW)	400 nJ (0.4 mW)
Reference	N/A	66000 nJ (66 mW)	62000 nJ (62 mW)
AS 1	310 nJ (0.31 mW)	250 nJ	200 nJ
AS 2	70.1 nJ	50 nJ	40 nJ
AS 3	35.1 nJ	20 nJ	3.4 nJ
AS 4	20.3 nJ	7.4 nJ	6.5 nJ
AS 5	11.5 nJ	4.4 nJ	4 nJ

pulse using sum-frequency generation in a $\chi^{(2)}$ medium. We used the pulse dubbed "Reference" in Fig. 4.2 as our strong, known pulse. We used the standard SHG FROG technique [24] to take a spectrogram of this pulse; the SHG FROG is not shown as part of the setup in Fig. 4.2. We placed our lab's homebuilt SHG FROG after all the mirrors in Fig. 4.2, requistioning the 10 micron BBO for use in the SHG FROG.

Once an SHG FROG trace was obtained, we used the open-source FROG code graciously provided by Dr. Trebino's group on his website [106] to retrieve the pulse shape. For SHG FROG, the pulse retrieval technique involves an algorithm dubbed "the method of generalized projections" [107]. The goal of the algorithm is to retreive the complex electric field $E(t)$ of the pulse from its FROG trace $I_{FROG}(\omega, t)$. The algorithm starts by making a guess for the signal field generated from the original pulse electric field, $E(t_i)$. This guess is called $E_{sig}(t_i, \tau_j)$, where t is the pulse time and τ is the delay time, with i, j corresponding to different data points in the 2D FROG trace. This guess is either a pure Gaussian pulse or noise, depending on which produces a trace most similar to the initial FROG spectrogram. Once this is done, an initial "generalized projection" is made by replacing $E_{sig}(t_i, \tau_j)$ with the square root of the magnitude of the intensity of the FROG trace, i.e.:

$$E'_{sig}(\omega, t) = \frac{E_{sig}(\omega, t)}{|E_{sig}(\omega, t)|} \sqrt{I_{FROG}(\omega, t)} \tag{4.1}$$

This accesses the set of waveforms that satisfies the FROG "data constraint", i.e.

$$I_{FROG}(\omega, t) = |\int E_{sig}(t, \tau) e^{-i\omega t} dt|^2 \tag{4.2}$$

The algorithm then makes another iteration by *projecting* onto the set of waveforms that satisfy the nonlinear optical constraint (for example, for second harmonic generation):

$$E_{sig}(t, \tau) \propto E(t) E(t - \tau) \tag{4.3}$$

This is done by minimizing the functional distance Z between the current (kth) iteration (i.e.

the Fourier transform of Eqn. 4.1 for the very first iteration) and the next iteration (the $k + 1$th iteration):

$$Z = \sum_{i,j=1}^{N} |E_{sig}^{(k)}(t_i, \tau_j) - E_{sig}^{(k+1)}(t_i, \tau_j)|^2 \tag{4.4}$$

This can be done by replacing $E_{sig}^{(k+1)}(t_i, \tau_j)$ directly with the expression in Eqn. 4.3 and using the method of steepest descent to find the gradient of Z with respect to the field $E_{sig}^{(k+1)}(t_i)$. Once this is done, $E_{sig}^{(k+1)}(t_i)$ is Fourier transformed back into the frequency domain and its intensity is once again replaced by that of the FROG trace. The process repeats until the reconstructed trace converges to a small error.

In practice, this method is very accurate and limited by experimental error. Using this process, we acquired a $< 2\%$ RMS difference between the modeled spectrogram and the experimentally obtained pulse, indicating very accurate retrieval.

After characterizing the main Reference pulse, we were able to use the same setup as depicted in Fig. 4.2 to characterize each sideband. After aligning all sidebands and the Reference pulse in the BBO (using the procedure outlined in Appendix A), we blocked all sidebands but one to minimize interference from other channels. We then replaced the thick, 1 mm BBO with a thin 10 micron BBO, collected the resulting SFG signal with a spectrometer, and varied the time delay of Reference with respect to the unknown pulse (i.e. AS n) to obtain an XFROG spectrogram. This process is repeated for each AS n.

Once a spectrogram is obtained, the pulse shape may be retrieved with an algorithm conceptually identical to that of the generalized projection technique described above. The functional distance minimized between subsequent iterations becomes:

$$Z = \sum_{i,j=1}^{N} |E_{sig}^{(k)}(t_i, \tau_j) - E^{(k+1)}(t_i)E_{Ref}(t_i - \tau_j)|^2 \tag{4.5}$$

Where $E_{Ref}(t_i - \tau_j)$ does not change from iteration to iteration and Z is minimized with respect to $E^{(k+1)}(t_i)$.

Using the jargon of Trebino, et al., [107], we retreive the temporal phase, $\phi(t)$, and intensity,

$I(t)$, expressing the electric field, $E(t)$, of each beam as:

$$E(t) = \frac{1}{2}\sqrt{I(t)}e^{i[\omega_0 t - \phi(t)]} + \text{c.c.} \tag{4.6}$$

Where ω_0 is the carrier frequency of each beam. We make what is called the "analytic signal" approximation and ignore the "c.c." terms. We performed a 1-D shape-preserving piecewise cubic interpolation in MATLAB to approximate the retrieved time-dependent phases and intensity at a finer time resolution than would have been available using the open-source FROG code. This assumes that the retrieved pulse properties do not change rapidly (i.e. on the scale of a single cycle), which seems a reasonable assumption for our pulses.

Once the pulse shapes are retrieved, we can move on to the final step of the setup, as described in Section 4.2.2.2.

4.2.2.2   Final Pulse Synthesis

After characterization, we used an interferometric technique developed by Zhi, et al. [8, 2] to show that all sidebands are coherently in-phase in the final, recombined beam. The core of this technique exploits the more-or-less constant frequency difference between each sideband. For example, the sum-frequency (SFG) between Stokes and AS 1 will be at the same frequency as the second harmonic (SH) of Reference. This is true of every evenly selected trio of beams, i.e. $\omega_{\text{Stokes}} + \omega_{\text{AS 3}} = 2 \times \omega_{\text{AS 1}}$. Hence, if all beams are collinear, the nonlinear signals will interfere constructively or destructively as a function of the delay of any one beam. By measuring the spectrum of the nonlinear signals as a function of sideband delay, we produce a spectrogram with clearly defined beats, as shown in Fig. 4.5.

We can then examine the phase of each set of beats (or Channels) with respect to each other to determine the phase between sidebands. This is illustrated in the inset to Fig. 4.5, where Channel A seems offset temporally from Channel B. We can correct this offset by moving the sideband in the channel (i.e. AS 4 in Channel A) forward or backward in time by adjusting the time delay. Since this corresponds to a delay on the order of $\phi = \pi/2 = \lambda/2 = 200$ nm, a precise translation stage

or glass window is required. For the manual stages, this can be achieved (in a not-very-repeatable manner) by lightly moving the stage until synchronization is obtained. We label the combination of this technique with SHG FROG as ξFROG, or cross-correlation interferometric FROG

Once synchronization is obtained and all beams are set to their proper energies, the pulse is assumed synthesized in the combined beam. This happens automatically as a consequence of the mathematics. A further check on this pulse synthesis technique is obtained by comparing the spectrograms obtained according to the method in Fig. 4.5 to those theoretically produced using the parameters retrieved in the ξFROG measurements. This sort of comparison is shown in Fig. 4.4 for a subset of four sidebands (Reference, Stokes, and AS 1/2). We produced the "theoretical" spectrogram by taking four chirped Gaussian beams at the frequencies indicated by the Stokes-AS 2 spectra in Fig. 4.3 and modelling (in MATLAB) the interference of their sum-frequencies/harmonics in the time domain. The experimental spectrogram also corresponds to data taken in preparation for the work in Section 5.3.2 to verify that all beams are in phase with each other.

A similar spectrogram comparison is planned for all 6 beams, but is hampered by the obvious mismatch between the linear beat period and the experimentally obtained beat period, as discussed in 4.4.1. The full explanation for why the beats are not consistent with linear expectations is not available, which limits our ability to generate an accurate theoretical spectrogram.

To summarize, once all bands are at least roughly aligned in time (but carefully collinearly aligned in space), we can use the resultant fringes in the spectrogram to pinpoint the moment of maximum positive interference. This corresponds to the phase configuration which leads to the synthesis of the shortest possible pulse. We can then retrieve the synthesized pulse field E_{synth} as a sum over the retrieved phases and envelopes for each n sideband [23]:

$$E_{\text{synth}} = \sum_{n=-1}^{N} \sqrt{I_n(t)} e^{i[\omega_n t - \phi_n(t)]}, \tag{4.7}$$

where N is the order of the highest-frequency sideband participating in the synthesis, $n = -1$ corresponds to Stokes 1, $I_n(t)$ is the retrieved intensity of the nth sideband, ω_n corresponds to the
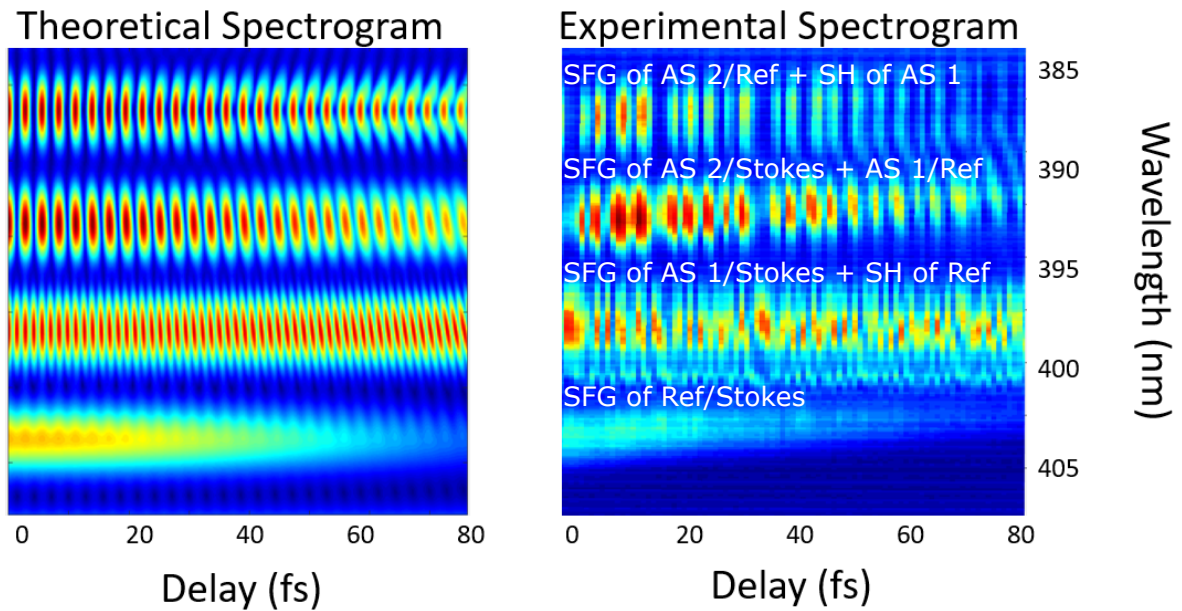
Figure 4.4: Right: theoretical spectrogram obtained by taking four chirped Gaussian beams at the frequencies indicated by the Stokes-AS 2 spectra in Fig. 4.3 and modelling the linear interference of their sum-frequencies/harmonics in the time domain. Left: experimental spectrogram taken with the setup in Fig. 4.2. While the beat period and spectral shape qualitatively matches with theory, there are some inconsistencies that have yet to be resolved, as is further discussed in Section 4.4.1. These differences worsen the more beams are added, so we have yet to construct a theoretical reproduction of Fig. 4.5.

Spectrogram with AS 4 - Stokes
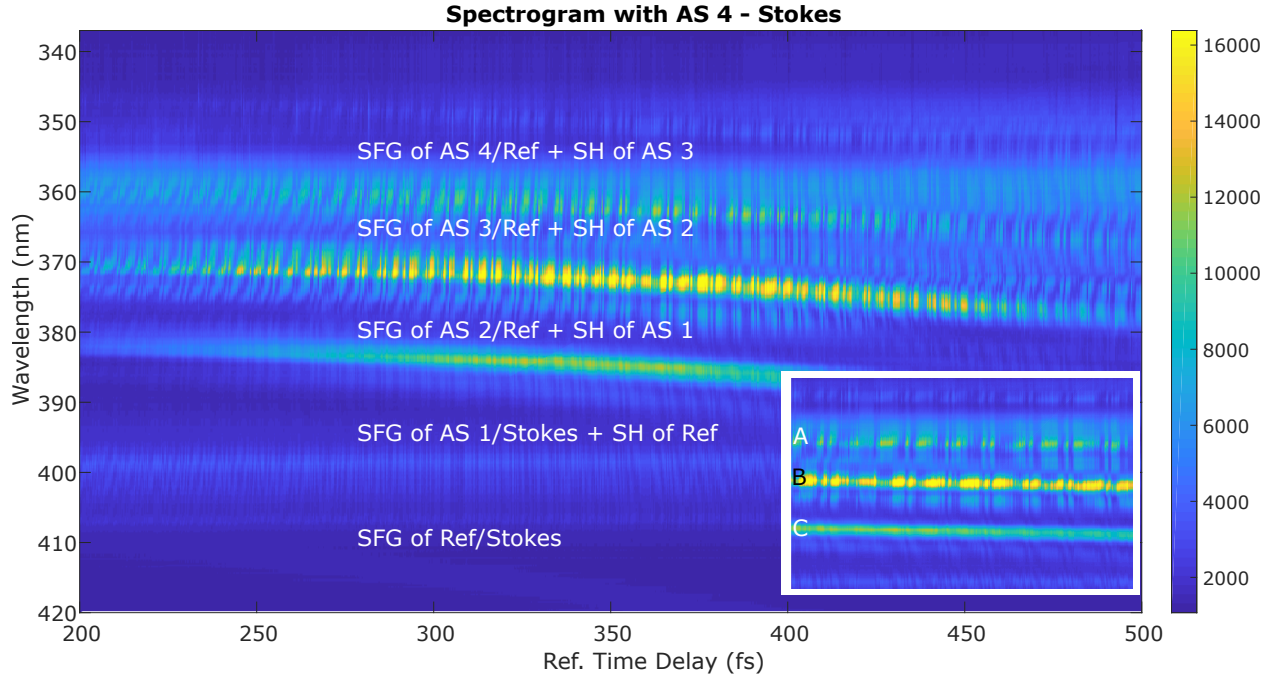
Figure 4.5: Time-resolved beats in the ξFROG spectrogram of 6 beams as described in Section 4.3.1, taken in a BBO with a thickness of 10 microns to avoid problems with phase matching. The AS 5 dichroic mirror was used to separate the fundamental beams from their nonlinear signals to avoid saturating the spectrometer, but as a result the AS 5 interference channel does not appear. The dominant interference channels are labelled. The inset shows a closeup of the spectrogram between 350 and 390 nm - Channels A, B, and C are slightly out of phase with each other, as the beats in A do not sync up with the beats in B. This can be corrected by adjusting the phases of AS 4, 3, and 2 (respectively).

carrier frequency of the nth sideband, and $\phi_n(t)$ is the retrieved phase of the nth sideband.

4.3 Results

4.3.1 Semrock Dichroic Mirror on Reference

We obtained final results for this Section by using Stokes, Reference, and AS 1-5 to synthesize an ultrashort pulse at the location of the BBO. A spectrogram that shows the various channels as being out-of-phase is shown in Fig. 4.5.

However, when the channels are in phase, we produce a ≈ 4.5 fs FWHM pulse, as shown in Fig. 4.8. This number implies a pulse that is either slightly shorter or of the same duration as the record Raman-synthesized pulse obtained by Zhi, et al., in [8], but without the need for a costly

pulse-shaper.

The XFROG spectrograms for each beam are shown in Fig. 4.6. The field envelopes and phases for all beams are plotted in Fig. 4.7. We have successfully retrieved these envelopes with $<$ 2% RMS difference between the experimentally obtained spectrograms and FROG-reconstructed spectrograms. Distortions in the pulse shapes of some beams are consistent with the GDD curves provided by Semrock, but are quite significant for some pulses including Reference, the non-Raman-generated part of the bandwidth. This causes the assymmetry in the temporal profile of the final synthesized pulse and exagerrated pre- and post-pulses shown in Fig. 4.8.

The 4.5 fs pulse duration is fairly robust so long as the pulses are added in phase. We retrieved the precise (to within 2% RMS accuracy) pulse shapes from the XFROG traces in Fig. 4.6. By recombining 7 beams, we make the pulse duration more insensitve to slight misalignments and energy fluctuations. These beams also represent a solid foundation towards our final goal of synthesizing a single cycle pulse by adding three more beams.

However, the extra bandwidth does not change the overall pulse shape – including the pre- and post-pulses visible at -35 and $+35$ fs. Adding bandwidth (at the proper phase) only decreases the pre- and post-pulse duration, it does not suppress the pulses themselves. These pre and post-pulses are also more intense than theoretically expected due to the chirped nature of our pulses, which causes the envelope amplitude at the location of the pre and post pulses to be higher. The pre- and post-pulses are limited by the comb-like nature of our source. The larger the frequency gap between our comb "teeth" the closer in time these pulses come to each other and the higher their amplitude. For sources that have a continuous bandwidth, these pre- and post-pulses are not an issue.

4.3.2 Edmund Optics Dichroic Mirror on Reference

We ran another set of data by using an Edmund Optics dichroic mirror instead of the Semrock mirror, which caused known phase distortions, to recombine Reference. This took care of the odd pulse splitting behavior shown in Fig. 4.6, but unfortunately resulted in one less sideband (AS 5) in this data set, mostly due to time limitations. AS 5, being the weakest beam and most unstable in
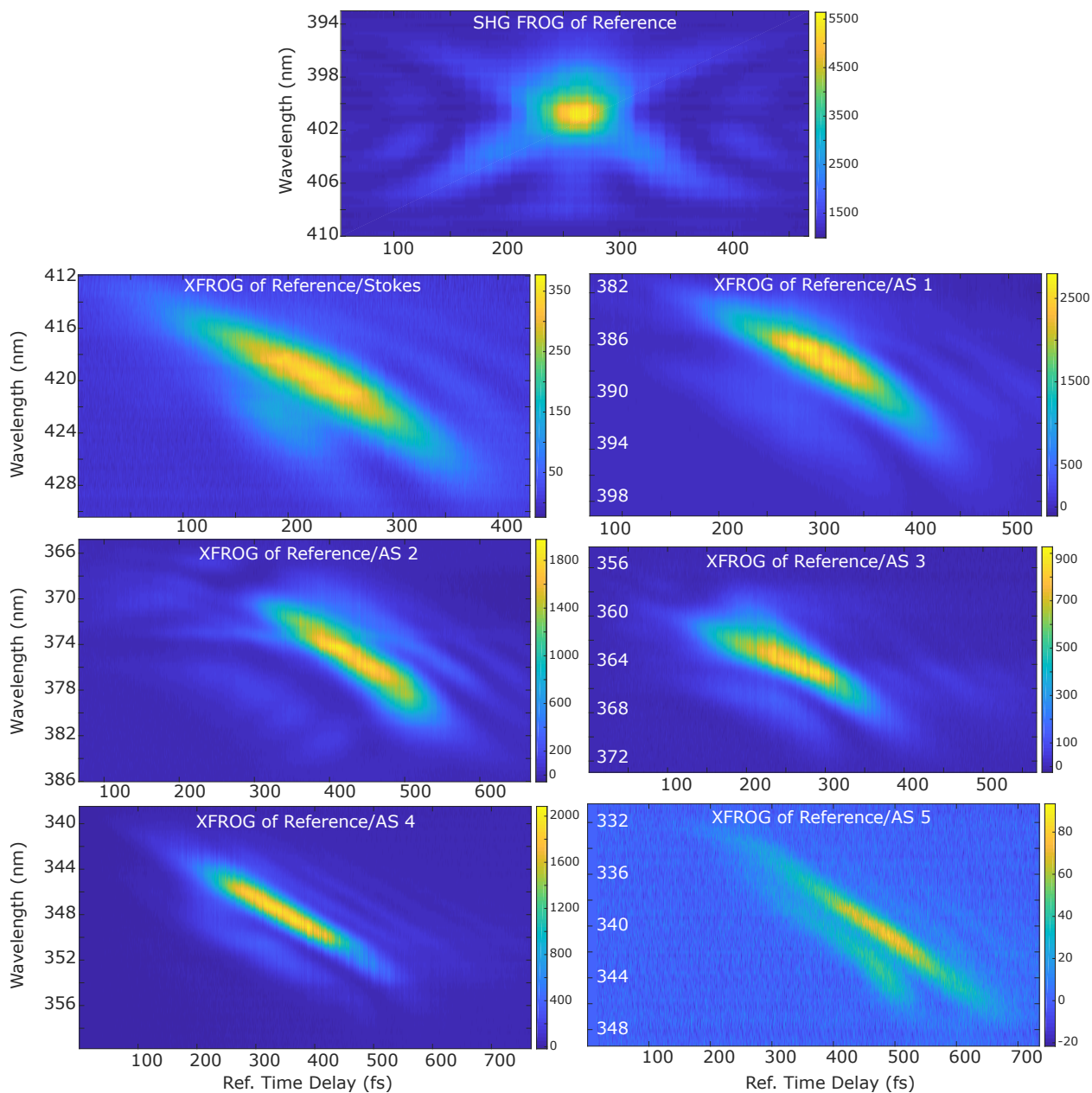
Figure 4.6: XFROG spectrograms of all beams employed in Section 4.3.1, using Reference as the known pulse to gate each unknown pulse. Each spectrogram was taken in a 10 micron BBO and they are all very similar, showing that indeed each beam is a Raman-shifted copy of the original (with slight distortions from dispersion added by each AS n dichroic mirror).
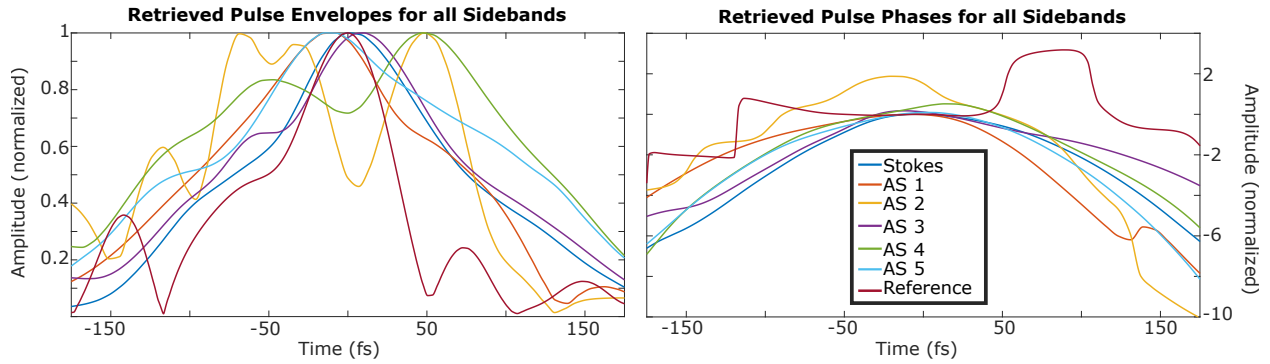
Figure 4.7: Pulse envelopes (left) and phases (right) of all beams employed in Section 4.3.1, using Reference as the known pulse to gate each unknown pulse. Each beam was retrieved with $< 2\%$ RMS error, indicating a very good retrieval.
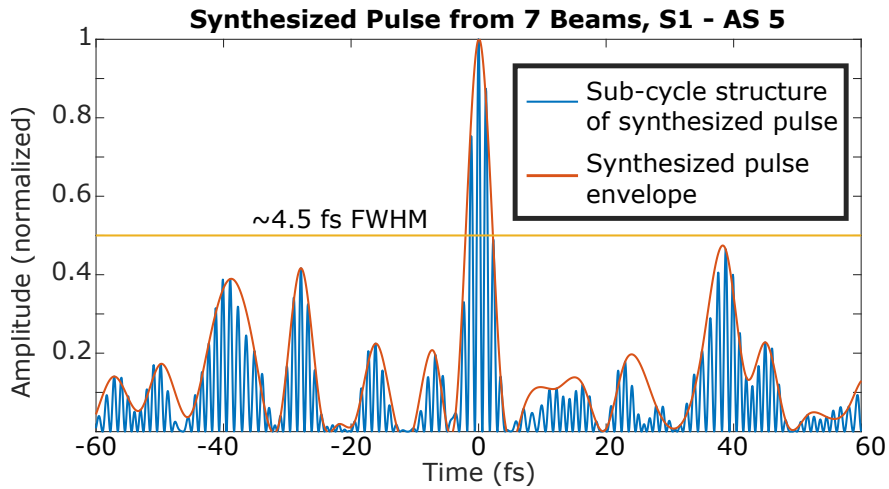
Figure 4.8: Pulse synthesized from Stokes, Reference, and AS 1-5, retrieved via ξFROG in Section 4.3.1.

terms of day-to-day alignent, was difficult to align collinearly with the rest of the sideband set.

The power for each sideband was also slightly optimized by adding an iris to the initial pump beam and moving the diamond closer to the focus, producing stronger (but same order of magnitude as Table 4.2) nonlinear signals in the final results. This set is considered the superior one to 4.3.1. The redone XFROGs are shown in Fig. 4.9. The retrieved pulse envelopes and phases from this set are shown in Fig.4.12, yielding slightly less distorted and faster pulses than Fig. 4.7.

The combined ξFROG spectrogram for this set is shown in Fig. 4.11, where AS 3 time delay is varied to produce temporal beats in each of the channels it participates in. By adding a time delay to AS 2, we can examine the effect of having one channel in-phase or out-of-phase with respect to the others. This comparison is shown in Fig. 4.11, where the channel where AS 2 participates as a second harmonic is clearly shifted with respect to the channel where it participates as a sum-frequency. This is explained in detail in Section 4.4.3. Due to time limitations (and the knowledge that eventually we would hopefully move on to this set anyway), such comparisons were not performed for the previous set.

The smoother pulse profiles in this data set result in suppressed pre- and post-pulses at -35 and $+35$ fs. Removing AS 5 from the bandwidth, however, increases the FWHM pulse duration from 4.5 fs to 5 fs, which puts our synthesized pulse on par with the one in [8]. On the other hand, our technique is more scalable, robust, and inexpensive than [8].

Both Sections 4.3.1 and 4.3.2 were included in this thesis to illustrate the large difference changing a single mirror can make in the XFROG spectrograms and retrieved pulses. It is also important to carefully recombining as many beams as possible, but the alignment is difficult to maintain without improvements to the source stability. The collinearality requirement in addition to the large travel distances of the beams makes day-to-day optimization challenging – as is illustrated by the loss of AS 5 from the bandwidth in this data set.
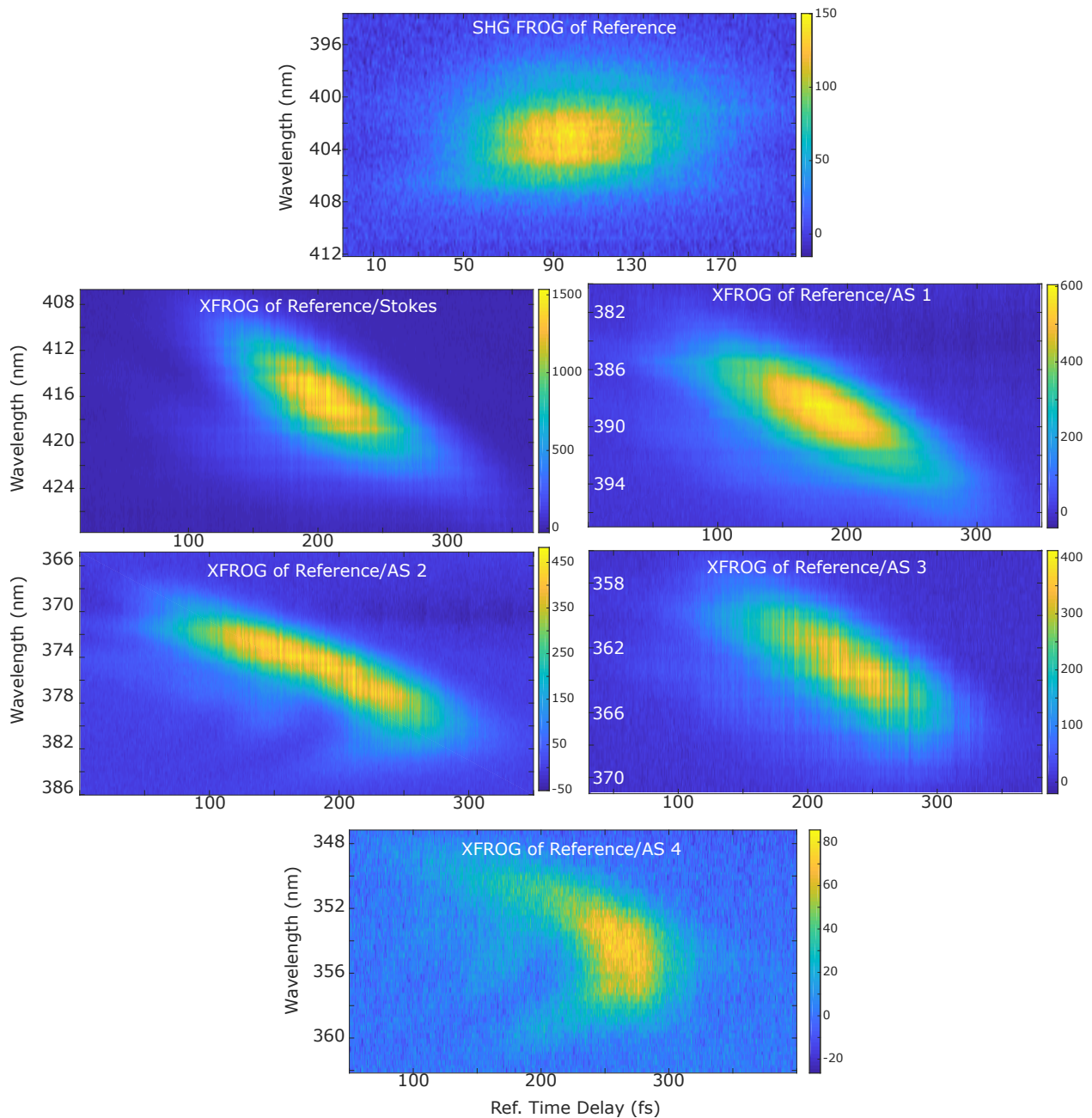
Figure 4.9: XFROG spectrograms of all beams employed in Section 4.3.2, using Reference as the known pulse to gate each unknown pulse. The nonlinear signals are shifted in frequency slightly with respect to Fig. 4.6, as the second harmonic of Reference is itself shifted slightly, due to the absence of third-order phase distortion. Each spectrogram was taken in a 10 micron BBO and they are all very similar, showing that indeed each beam is a Raman-shifted copy of the original (with slight distortions from dispersion added by each AS n dichroic mirror).

Spectrogram of Stokes 1 - AS 4

Labels in figure:
SFG of AS 2 + 3/AS 1 + 4
SH of AS 2/SFG of AS 1 + 3/Ref + AS 4 - Channel A
SFG of AS 1 + 2/Ref + AS 3/S 1 + AS 4 - Channel B
SH of AS 1/SFG of Ref + AS 2/S 1 + AS 3
SFG of Ref + AS 1/S 1 + AS 2
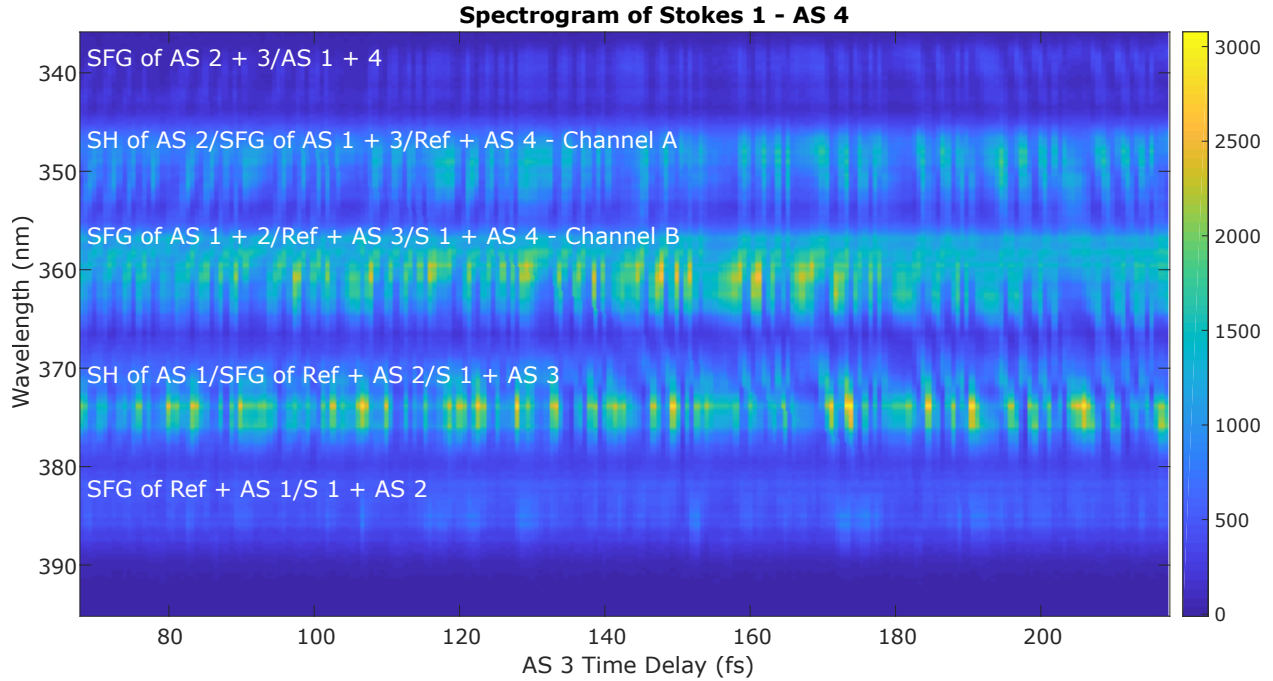
Figure 4.10: Time-resolved beats in the ξFROG spectrogram of 6 beams as described in Section 4.3.2, taken in a BBO with a thickness of 10 microns to avoid problems with phase matching. The filters described in Section 4.2.1 were used to separate the nonlinear signals from the fundamentals, so that the AS 5 mirror could be used to recombine AS 5 (AS 5 did not participate in this synthesis anyway for different reasons). The channels marked A and B are examined closer in Fig. 4.11.

In-Phase Spectrogram (AS 4 - S 1)   **Out-of-Phase Spectrogram (AS 4 - S 1)**
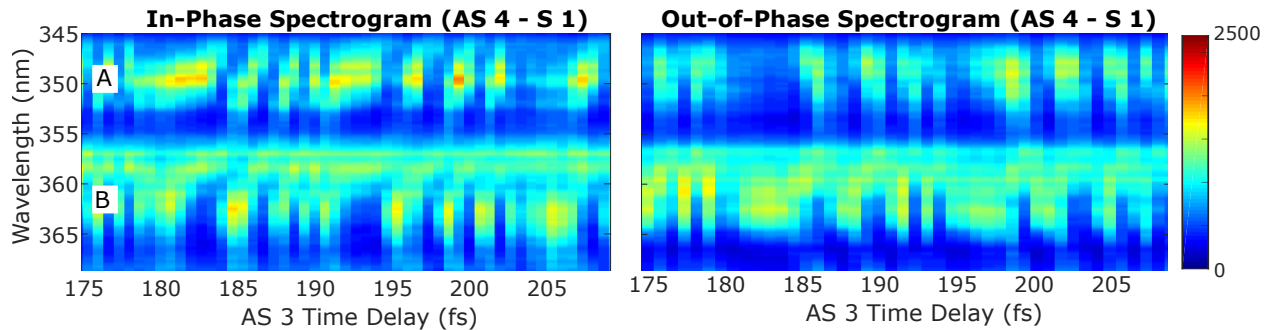
Figure 4.11: A and B correspond to Channels A and B marked in Fig. 4.10. Between the in-phase and out-of-phase comparison, the only change we have made is adding a $\pi/2$ phase to AS 2. Although AS 2 participates in both channels, in Channel A it participates as a second harmonic, and in Channel B it participates in a sum-frequency. Hence, AS 2's phase is doubled for Channel A in relation to Channel B and results in the channels being shifted with respect to each other. The other frequency channels are not shown in this figure, but match with Channel B (as AS 2 participates as a sum-frequency in each of those as well).
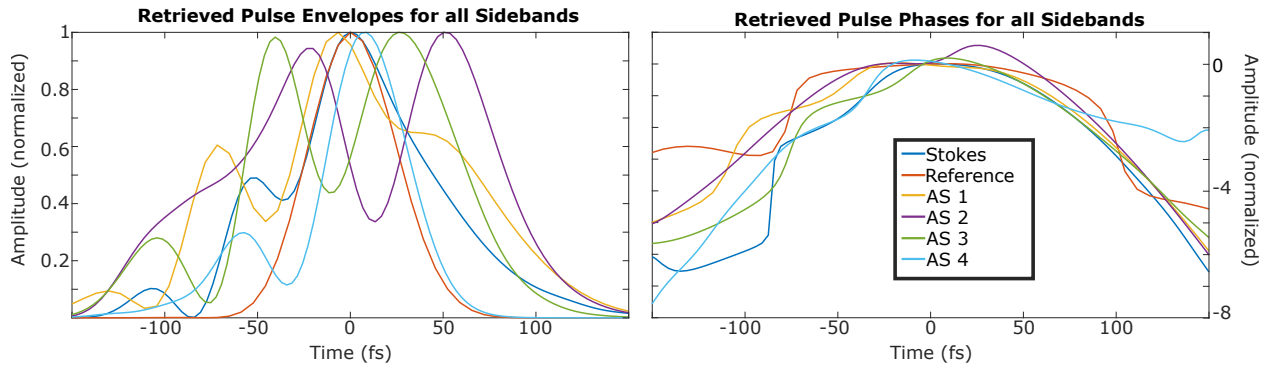
Figure 4.12: Pulse envelopes (left) and phases (right) of all beams employed in Section 4.3.2, using Reference as the known pulse to gate each unknown pulse. Each beam was retrieved with $< 2\%$ RMS error, indicating a very good retrieval.
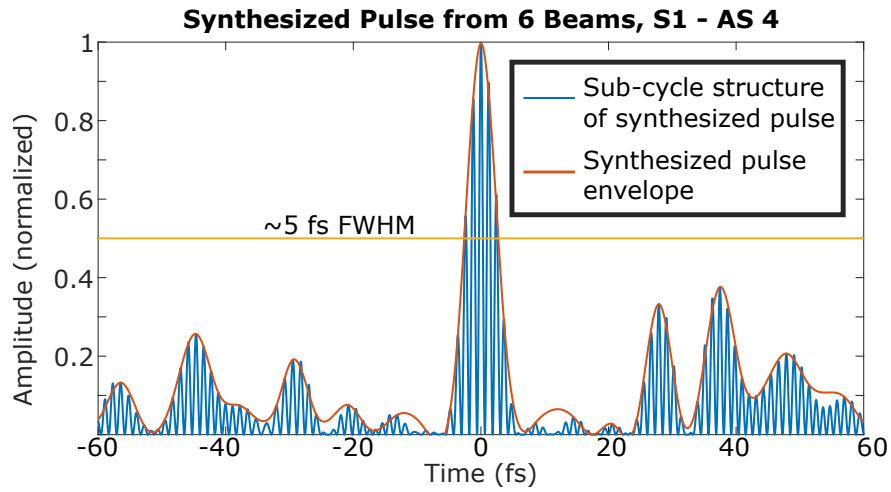
Figure 4.13: Pulse synthesized from Stokes, Reference, and AS 1-4, retrieved via ξFROG in Section 4.3.2.
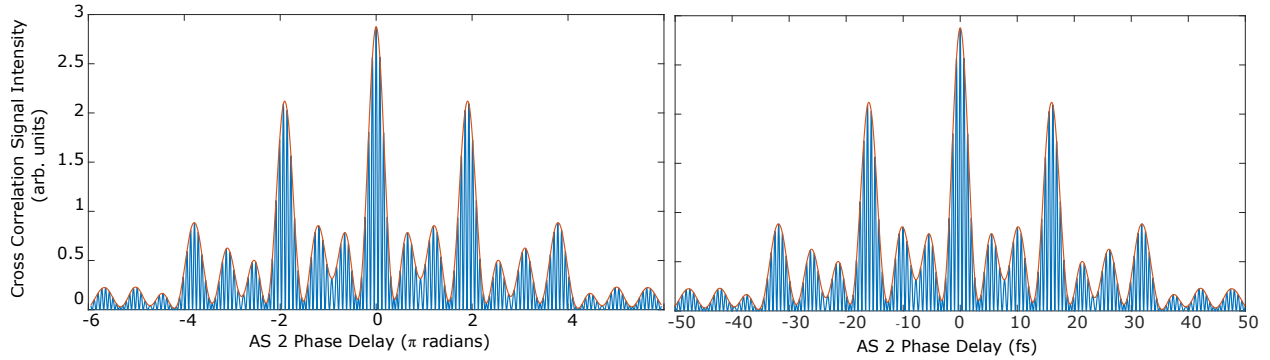
Figure 4.14: Cross correlations traces, produced by theoretically modelling the interference of five chirped Gaussian pulses and varying the delay of one of them (AS 2) by adding a phase. While the shape of the traces is the same regardless of the time axis, changing the axis to fs helps clarify that the beats are over within the specified pulse duration (≈ 100 fs). The trace shape also at least roughly matches the experimental data in [8].

4.4   Discussion

4.4.1   Data Analysis – Clarifying the Beat Period

This section is meant to explain our analysis of the beat period, which, as shown in Fig. 4.5, is clearly not limited to a single frequency. This is in contrast to both the theoretical spectrogram obtained in Fig. 4.4 and the results obtained by Zhi, et al. in [8]. In [8], the authors interpret the beats they obtain in the interference of the SFG of AS 1/3 with the SH of AS 2 to have a period of 16 fs, even though the phase of AS 2 is only changed by 2π. This comes out of the idea that small changes in the phase of one sideband (i.e. AS 2) have large effects on the overall synthesized group delay, as illustrated in Fig. 4.14.

In our experiment, we clearly do not obtain a period of 16 fs in our fringes, but this does not have to be mutually exclusive with the interpreation of Zhi, et al. Mathematically, the $1-2$ fs beats we obtain are equivalent to changing the group delay in the overall synthesized pulse by 16 fs, but our results do not consitute a direct measurement of this 16 fs group delay. Under a different set of experimental conditions, this 16 fs period could likely be directly measured and obtained. Under non-collinear conditions, we will definitely not see the fast beating we see here, which corresponds
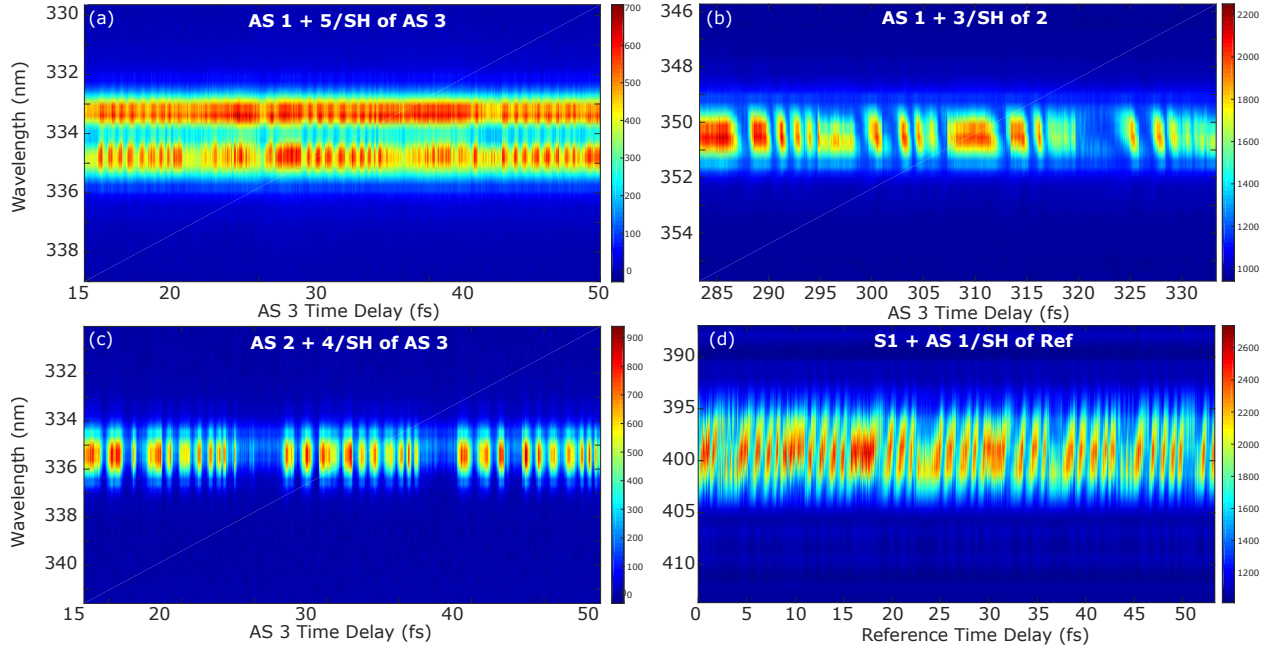
Figure 4.15: Spectrograms of different variants of beats found in our setup, taken in the 1 mm BBO. The beat period is identical in the thinner BBO, but the signal-to-noise is lower which results in less clear interference. In all cases, we interfere three beams. The more beams are added, the more complicated the beat pattern becomes, as seen in Fig. 4.5. Hence, in order to understand the phenomenon, we feel that it is best to start with sets of three beams. (a) and (c) are taken at the same frequency - the second harmonic of AS 3 - and by moving the same translation stage. Qualitatively, the beats are very similar, but the periods of both the fringes and sections of incoherence are different. (b) is also taken by delaying the AS 3 stage, but this time AS 3 participates in the SFG process instead of serving as the SH. (d) is taken by delaying the Reference stage, showing qualitatively similar beats to (a) and (c) (but again, with different periods and number of fringes).

to the field of the SFG-synthesized pulse moving in and out of sync with the SHG part of the pulse.

While it is easy to write off the multiple frequencies shown in Fig. 4.5 as noise, we can obtain clearer measurements of the beat frequencies by looking at just trios of beams (instead of the full spectrum). Sample measurements of such trios are shown in Fig. 4.15

Let us label these beams as w_1, w_2, and w_3, where in general these are each separated by the Raman shift and $w_1 + w_3 = w_2$. The main characteristics of the beats are that:

1. the beats are periodically chirped,

2. the beats disappear with a period that **roughly** matches $2w_3 - 2w_1$,

3. the beats have the same period and disappearance in thick and thin BBOs,

4. there are different frequency components to the beats depending on which sideband is moved, and

5. there is no good linear explanation for any of these.

Point 4 is an essential point. It at first led us to believe that the noise was simply a translation stage error. When taking measurements of the interference of AS 1+3/AS 2 by varying AS 1 and its corresponding Newport stage (which has a maximum time resolution of 200 nm, or 0.667 fs), the extra frequencies are not there. This is shown in Fig. 4.16, which compares measurements of this interference using the AS 1 stage and the AS 3 stage.

However, when looking at Reference + AS 2/AS 1 interference by varying Reference and AS 1, we can see that the spectrogram generated by moving AS 1 has the disappearing frequency components, but the spectrogram generated by moving Reference does not. This is illustrated in Fig. 4.17. AS 3 and Reference have the same model of translation stage, (as seen in Table 4.1), so if one translation stage has an issue that shows up in these spectrograms, the other likely will as well.

Our main hypothesis is that cross phase modulation between $2w_2$ and $w_1 + w_3$ is to blame. We plan further theoretical investigation into this hypothesis.

4.4.2 (No) Phase between Second Harmonic and Fundamental

One may note that, just because the second harmonics and sum-frequencies are in phase with each other, does not mean that the fundamentals are. This limits the use of our XFROG/beats technique from generating and characterizing "ready-to-use" single-cycle pulses. In other words, the sum-frequencies and second-harmonics of each beam may generate a single-cycle pulse, but if we remove the BBO the single-cycle pulse vanishes as the fundamental phases will not quite match.
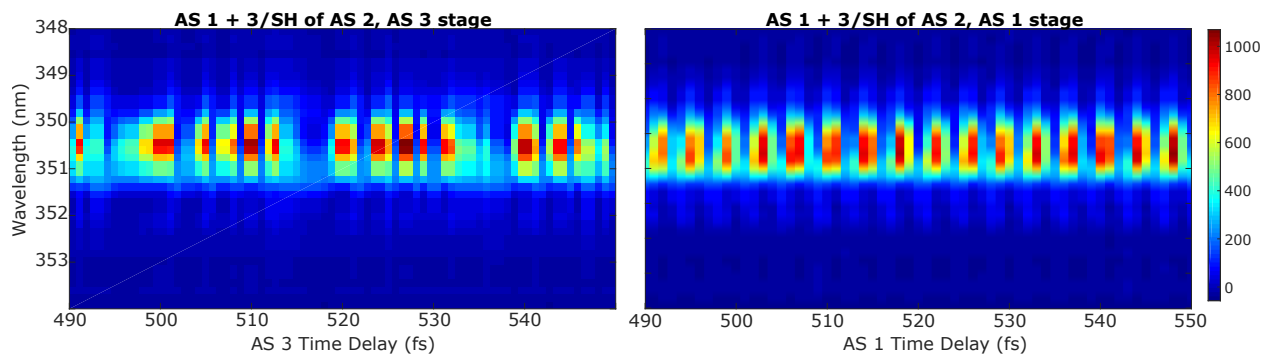
Figure 4.16: Beats produced by looking at the interference of AS 1 + 3/Second Harmonic of AS 2 by varying AS 3 and its corresponding Thorlabs stage (left) or varying AS 1 and its corresponding Newport stage (right) in the thick BBO. The time resolution for both stages is the same in this figure.
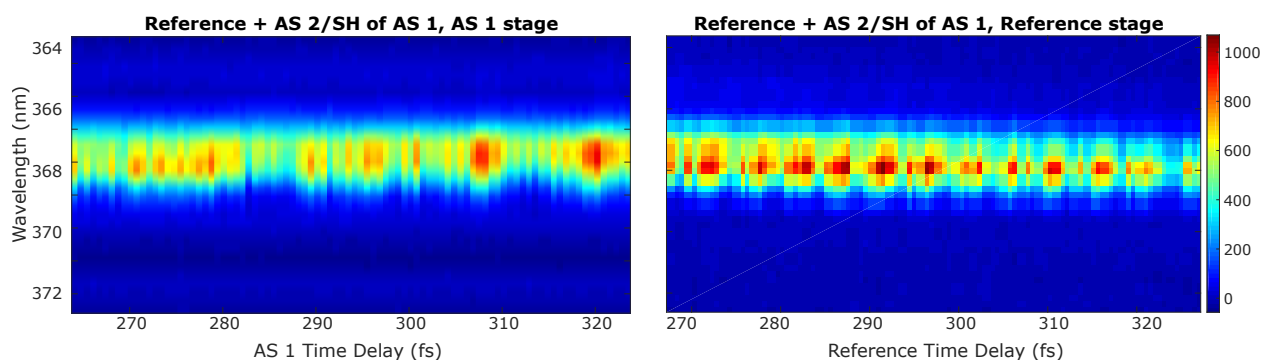
Figure 4.17: Beats produced by looking at the interference of Reference + AS 2/Second Harmonic of AS 1 by varying AS 3 and its corresponding Thorlabs stage (left) or varying AS 1 and its corresponding Newport stage (right) in the thick BBO. The time resolution for both stages is the same in this figure.

However, this is not a problem for our setup, because (assuming perfect phase-matching in the BBO) second harmonics are actually in phase with their fundamentals. In other words, second harmonics do not gain a phase mismatch from the fundamental through propagation in the crystal or some other means. There have been both theoretical [25] and experimental [108, 109] proofs of this. For the sake of completeness, let us briefly summarize both approaches.

Closely following [25] in the theoretical approach, we assume that the medium is lossless both at the fundamental frequency ω_1 and at the second harmonic frequency, $\omega_2 = 2\omega_1$. We take the total electric field within the nonlinear medium to be the sum of the fundamental and second harmonic electric fields:

$$E(z,t) = E_1(z,t) + E_2(z,t) \tag{4.8}$$

where each component is expressed in the standard way in terms of a complex amplitude $E_j(z)$ and slowly varying amplitude $A_j(z)$:

$$E_j(z,t) = E_j(z)e^{-i\omega_j t} + \text{c.c.}. \tag{4.9}$$

where

$$E_j(z) = A_j(z)e^{ik_j z}. \tag{4.10}$$

We write the complex, slowly varying field amplitudes as:

$$A_1 = \left(\frac{I}{2n_1\epsilon_0 c}\right)^{1/2} u_1 e^{i\phi_1}, \tag{4.11}$$

$$A_2 = \left(\frac{I}{2n_2\epsilon_0 c}\right)^{1/2} u_2 e^{i\phi_2}. \tag{4.12}$$

Where we have introduced the total intensity of the two waves:

$$I = I_1 + I_2, \tag{4.13}$$

and the intensity of each wave is given by:

$$I_j = 2n_j \epsilon_0 c |A_j|^2. \tag{4.14}$$

As a consequence of the Manley-Rowe relations, the total intensity I is invariant under propagation. n_1, n_2 are the linear refractive indices for ω_1 and ω_2 respectively, and ϵ_0 is the vacuum permeability. ϕ_1 and ϕ_2 are the phases of ω_1 and ω_2 respectively, and in a sense are the quantities we are most interested in in this discussion. u_1, u_2 correspond to the real, normalized field amplitudes defined such that $u_1(z)^2 + u_2(z)^2 = 1$ is a conserved quantity.

We also define a normalized distance parameter

$$\zeta = z/l, \tag{4.15}$$

where z is the propogation coordinate in the crystal and l is the characteristic distance over which the fields exchange energy, defined by:

$$l = \left(\frac{2n_1^2 n_2}{\epsilon_0 c I} \right)^{1/2} \frac{c}{2\omega_1 d_{eff}} \tag{4.16}$$

We also define a phase mismatch parameter $\Delta k = 2k_1 - k_2$ and a normalized phase mismatch parameter related to l:

$$\delta s = \Delta k l \tag{4.17}$$

Finally, we also define a relative phase of the interacting fields:

$$\theta = 2\phi_1 - \phi_2 + \Delta k z, \tag{4.18}$$

where this is clearly still the quantity we are most interested in.

By inputting these normalized quantities into the coupled-amplitude equations that can be obtained by some algebra from the wave equation (which can be derived from Maxwell's equations), we obtain an equation for θ:

$$\frac{d\theta}{d\zeta} = \Delta s + \frac{\cos\theta}{\sin\theta}\frac{d}{d\zeta}(\ln u_1^2 u_2) \tag{4.19}$$

If we assume perfect phase-matching, Δk and hence, Δs vanish. We can then rewrite Eq. 4.19 by differentiating it through and rearranging everything to one side to obtain:

$$\frac{d}{d\zeta}\ln(u_1^2 u_2 \cos\theta) = 0 \tag{4.20}$$

Hence, the quantity $\ln(u_1^2 u_2 \cos\theta)$ is a **constant**, which we can call $\ln\Gamma$, so that the solution to Eq. 4.20 becomes:

$$u_1^2 u_2 \cos\theta = \Gamma \tag{4.21}$$

This is the essential part. Γ is independent of the normalized propagation distance ζ, and is thus conserved for every point through the crystal. Hence, if the amplitude of either of the two input fields is equal to zero (i.e. there is no second harmonic input on the face of the crystal), $\Gamma = 0$ at the input of the crystal. It is then equal to zero for all values of ζ, demanding in general that:

$$\cos\theta = 0, \tag{4.22}$$

and so:

$$\theta = 2\phi_1 - \phi_2 = 0 \tag{4.23}$$

Leading to the second harmonic field being perfectly in phase with the input fundamental.

While there have been some assumptions made throughout this derivation (i.e. we assume no dispersion – in reality, there is dispersion through the crystal, which can result in some phase

corrections), experimental studies done with THz generation confirm that the second harmonic is indeed in phase with the fundamental, even for ultrashort pulses.

This was demonstrated by [108, 109]. [108, 109] were investigating enhanced THz generation when the fundamental of a Ti:Saphhire laser was focused and propagated through a BBO crystal placed prior to the beam waist. They confirmed that it was a four-wave rectification (FWR) process, brought about by the interaction of the second harmonic and fundamental, that drove the enhancement in THz signal. This FWR process is only possible when the second harmonic and fundamental of the beam are in phase; they confirmed depletion of signal when they changed the phase of the second harmonic with respect to the fundamental via a thin, angled, quartz-glass microslip. When the phase was tuned such that the second harmonic was again in phase with the fundamental, the enhanced signal was recovered. These results confirm that the derivation above is reasonably accurate in the case of ultrashort pulses, and, for the case of perfect phase-matching, the second harmonic of a beam is in phase with the fundamental.

This fact is, in principle, sufficient to find an overlap that produces a single-cycle pulse in both the SHG/SFG beats as well as the fundamentals, as is shown below.

4.4.3   Determining the Important Phases

Let us now consider the sum of three CW fields with unit amplitude, frequencies $\omega - \Omega$, ω and $\omega + \Omega$, and phases ϕ_-, ϕ, and ϕ_+ respectively (that is, CW fields with arbitrary phases, but equal amplitudes and equidistant in frequency). Each beam will also have the same (randomly determined, as our laser is not CEP-stabilized) CEP. In the combined beam, discussing the phase of each beam separately makes little sense, as adding a constant phase to each ϕ_n should not change the overall temporal structure of the synthesized beam, but will change each individual phase. Hence, we redefine the relevant phases in the context of the synthesized beam.

Let us split each of the phases into CEP and delay:

$$
\begin{cases}
\phi_- & = \phi_0 + (\omega - \Omega)\,\Delta t \\[2mm]
\phi & = \phi_0 + \Delta\phi + \omega\Delta t \\[2mm]
\phi_+ & = \phi_0 + (\omega + \Omega)\,\Delta t
\end{cases}
\tag{4.24}
$$

Note that Eqn. 4.24 is a system of three equations with three unknowns (ϕ_0, Δt, and $\Delta\phi$), and it has a unique solution unless $\Omega = 0$. It is easy to show that the determinant of this equation matrix equals 2Ω. In other words, for any combination ϕ_-, ϕ and ϕ_+ one can find ϕ_0, Δt, and $\Delta\phi$ that satisfy Eqn. 4.24. The solution is:

$$
\begin{cases}
\phi_0 & = \frac{\phi_+ + \phi_-}{2} - \frac{\omega}{\Omega}\frac{\phi_+ - \phi_-}{2} \\[2mm]
\Delta\phi & = \phi - \frac{\phi_+ + \phi_-}{2} \\[2mm]
\Delta t & = \frac{\phi_+ - \phi_-}{2\Omega}
\end{cases}
\tag{4.25}
$$

We find that ϕ_0 is effectively the CEP of the synthesized pulse, $\Omega\Delta t$ affects the linear time delay of the synthesized pulse, and $\Delta\phi$ is the only phase which significantly affects pulse structure. This is shown in Fig. 4.18, where synthesized pulse shapes are plotted as functions of different relative phases.

Note that the prior set of equations is not a proof, but we can analytically recover $\Delta\phi$ and Δt by adding the cosine expressions for each CW field.

First, let us review the basic trigonometry formulas that we will need:

$$
\cos x + \cos y = 2\cos\frac{x+y}{2}\cos\frac{x-y}{2}
\tag{4.26}
$$

$$
\cos(x + y) = \cos x \cos y - \sin x \sin y
\tag{4.27}
$$

$$
C\cos x + S\sin x = A\cos(x + \phi),
\tag{4.28}
$$
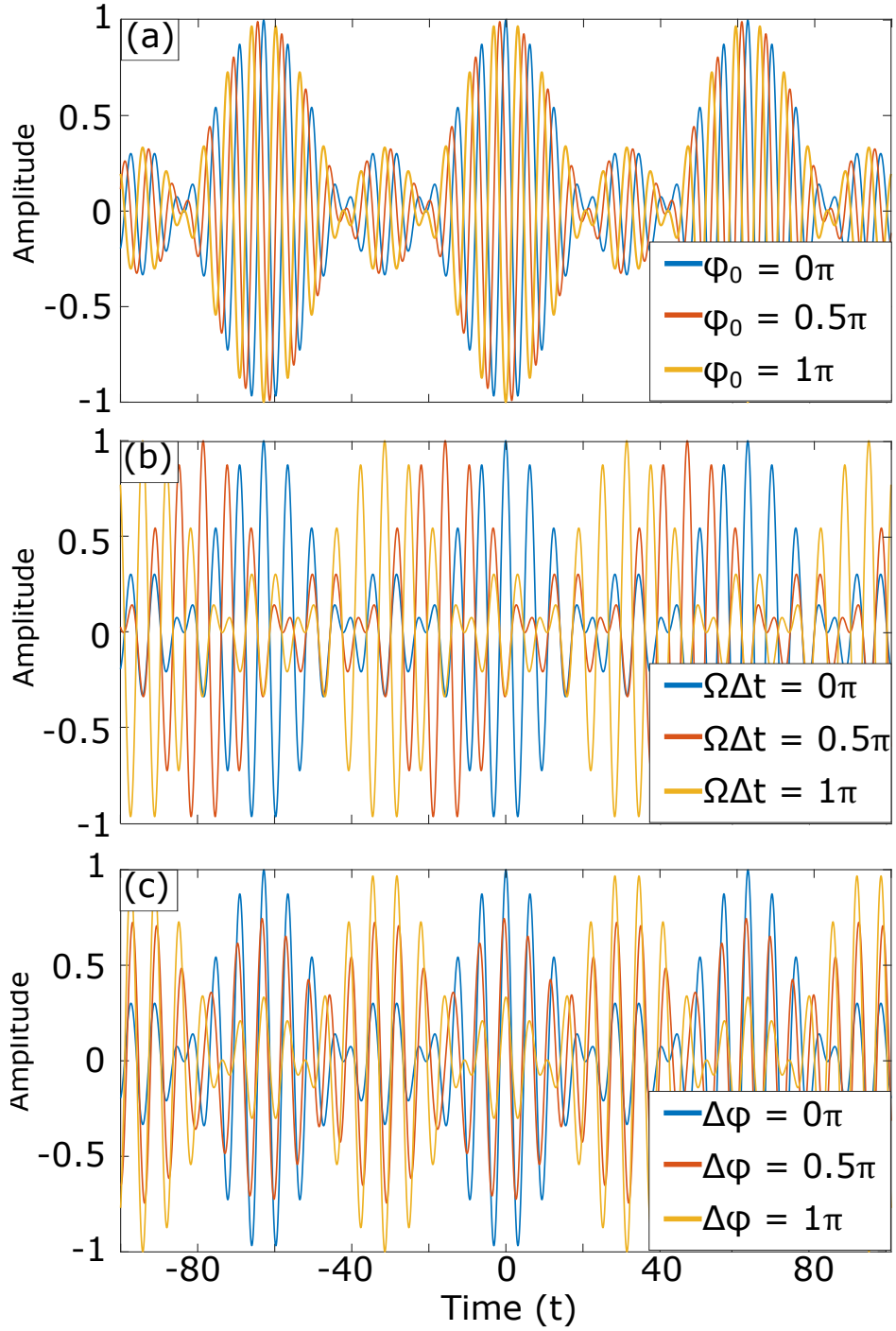
Figure 4.18: Multiple synthesized beams. Demonstrating the effects of changing (a) $\phi_0 = \frac{\phi_+ + \phi_-}{2} - \frac{\omega}{\Omega}\frac{\phi_+ - \phi_-}{2}$ (i.e. the carrier envelope phase) while keeping $\Omega\Delta t$ and $\Delta\phi$ constant; (b) $\Omega\Delta t = \frac{\phi_+ - \phi_-}{2}$ (i.e. the time delay) while keeping $\Delta\phi$ and ϕ_0 constant; (c) $\Delta\phi = \phi - \frac{\phi_+ + \phi_-}{2}$ while keeping $\Omega\Delta t$ and ϕ_0 constant. As shown in the text, $\Delta\phi$ is the only phase which significantly affects the pulse structure.

where

$$A = \sqrt{C^2 + S^2}, \tag{4.29}$$

is the amplitude of the sum and

$$\phi = \arccos \frac{C}{A} \operatorname{sgn} S \tag{4.30}$$

is its phase.

We can now derive the analytical expression for the sum of three CW fields, and in particular, $\Delta\phi$ and Δt, as follows:

$$
\begin{aligned}
E(t) &= \cos\left((\omega - \Omega)\,t + \phi_-\right) + \cos\left(\omega t + \phi\right) + \cos\left((\omega + \Omega)\,t + \phi_+\right) = \\
&= \cos\left(\omega t + \phi\right) + 2\cos\left(\Omega t + \frac{\phi_+ - \phi_-}{2}\right)\cos\left(\omega t + \frac{\phi_+ + \phi_-}{2}\right) = \\
&= \cos\left(\omega t + \frac{\phi_+ + \phi_-}{2} - \frac{\phi_+ + \phi_-}{2} + \phi\right) + 2\cos\left(\Omega t + \frac{\phi_+ - \phi_-}{2}\right)\cos\left(\omega t + \frac{\phi_+ + \phi_-}{2}\right) = \\
&= \cos\left(\omega t + \frac{\phi_+ + \phi_-}{2}\right)\cos\left(\phi - \frac{\phi_+ + \phi_-}{2}\right) - \\
&\quad - \sin\left(\omega t + \frac{\phi_+ + \phi_-}{2}\right)\sin\left(\phi - \frac{\phi_+ + \phi_-}{2}\right) + \\
&\quad + 2\cos\left(\Omega t + \frac{\phi_+ - \phi_-}{2}\right)\cos\left(\omega t + \frac{\phi_+ + \phi_-}{2}\right)
\end{aligned}
$$

Let us denote $\Delta\phi \equiv \frac{2\phi - \phi_+ - \phi_-}{2}$ and $\delta \equiv \frac{\phi_+ - \phi_-}{2}$. Then:

$$E(t) = \cos\left(\omega t + \frac{\phi_+ + \phi_-}{2}\right)\left(\cos\Delta\phi + 2\cos\left(\Omega t + \delta\right)\right) + \sin\left(\omega t + \frac{\phi_+ + \phi_-}{2}\right)\sin\Delta\phi \tag{4.31}$$

Applying Eqs. (4.28) – (4.30) we get the following:

$$E(t) = A(t)\cos\left(\omega t + \hat{\phi}(t)\right) \tag{4.32}$$

where amplitude is given by:

$$A(t) = \sqrt{(\cos \Delta\phi + 2\cos(\Omega t + \delta))^2 + \sin^2 \Delta\phi} \qquad (4.33)$$

and phase is given by:

$$\hat{\phi}(t) = \frac{\phi_+ + \phi_-}{2} + \arccos \frac{\cos \Delta\phi + 2\cos(\Omega t + \delta)}{A(t)} \text{sgn}\Delta\phi \qquad (4.34)$$

In the limit $\Omega \ll \omega$ we see that the phase combinations that affect the pulse shape (i.e. $A(t)$) are $\Delta\phi$ and δ. At the same time, $\delta = \Omega\Delta t$ only affects the temporal shift of $A(t)$.

Hence, $\Delta\phi$ is the only phase which significantly affects pulse structure. It is also (luckily) the phase we can most easily measure with our setup. $\Delta\phi = 0$ corresponds quite simply to a bright spot in Fig. 4.5, while $\Delta\phi = \pi$ corresponds to a dark spot in the same figure. Therefore, as long as we are not interested in the CEP, we can freely use our technique to accurately retrieve the synthesized pulse.

This situation can be extrapolated to the point when one of the phases, i.e. ϕ, is actually the combination of two phases. This is relevant to the situations when the central frequency for the interference situation described above is actually a sum-frequency of two beams, say ϕ_1 and ϕ_2. In this case, $\Delta\phi$ becomes:

$$\Delta\phi = \frac{\phi_1 + \phi_2}{2} - \frac{\phi_+ + \phi_-}{2}, \qquad (4.35)$$

Such that each phase contributes equally to $\Delta\phi$. This helps us determine when a particular sideband phase ϕ_n is zero or non-zero by comparing the delay mis-match between channels where ϕ_n contributes equally with other phases (i.e. as a sum-frequency) and when it counts for twice (i.e. as a second harmonic).

4.5 Conclusions

In conclusion, we successfully characterized several anti-Stokes sidebands via the XFROG technique and interferometically recombined these into a ≈ 5 fs pulse. Scaling the setup to include more sidebands and hence synthesize an even shorter pulse is imminently feasible. In the future, we plan several experiments investigating the ionization of Xenon with single-cycle pulses. These experiments will be along the lines detailed in Sec. 5, but ideally with higher pulse energy and more sidebands. This chapter sets the stage for these experiments by making it possible to be confident in the generation of a single-cycle pulse via our setup (albeit at lower energies).

5. XENON IONIZATION WITH ULTRAFAST PULSES

5.1 Introduction

As part of my PhD (but a part that did not end with any publishable results), we experimented with ionizing Xenon gas with ultrafast pulses. The idea was to use the pulse that we have optimized based off of the procedure described in Section 4 to ionize Xenon gas in a vacuum, pressure-controlled chamber. As has been demonstrated by Sokolov *et al.* in [61], the ion signal grows as the pulse duration decreases; we could therefore use this signal as a rough diagnostic for our pulses. Further, our work would provide an independent confirmation that the multiphoton ionization of Xenon would follow the order closer to the lower bound of the broadband source. Unfortunately, to correctly synthesize a FTL pulse, each sideband must have equal power to the rest of the sidebands. Ergo, the power of the highest-order-sideband used limits the possible applications of the Fourier-synthesized pulses. Our highest-order-beam at the time was AS 2; the pulse energy in this beam was 30 nJ. 30 nJ $\times 4 = 120$ nJ over ≈ 10 fs, resulting in a peak power of 12 MW. This was not enough to produce a detectable ion signal.

However, we performed preliminary experiments in order to verify this logic, using the maximum power available to us from each sideband and the minimum power in the Reference beam to detect an ionization signal.

5.2 Preliminary Experimental Parameters and Setup

The experimental setup is shown in Fig. 5.1.

We set Stokes and AS 1 and 2 to their maximum available power. We used ND filters to attenuate Reference until an ionization signal was barely detectable – at 62μJ over ≈ 100 fs, this corresponded to a peak power of roughly 620 MW. When focused to a roughly ≈ 100 micron radius spot size, we get a peak power of 1.97×10^{16} W/m^2. The power in each beam is recorded in Table 5.1. The power in Reference (the most intense beam) was measured using a Coherent FieldMax II power meter and PM10 head. The power in Stokes was measured using the same meter and PS10

70
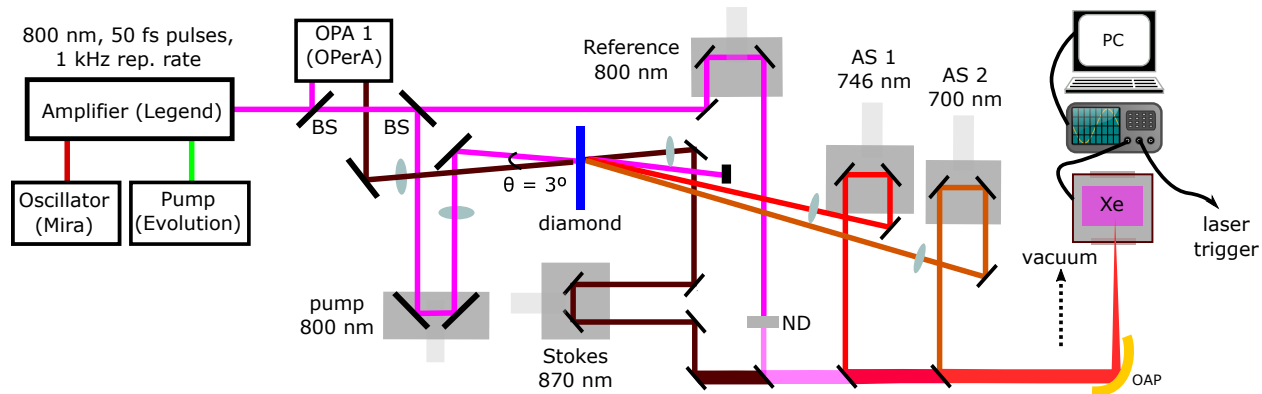
Figure 5.1: A schematic of our experimental setup for using ultrafast synthesized pulses to ionize Xenon in a 10^{-7} mbar vacuum. OAP stands for off-axis paraboloid, ND stands for neutral density filter, used to lower the power of Reference, as described in the text.

Table 5.1: Power of beams in preliminary experiments.

Beam Name, Wavelength	Measured Power (Convenient Units)
Reference, 800 nm	62 mW (62μJ)
Stokes, 870 nm	0.35 mW (350 nJ)
AS 1, 750 nm	150 nJ
AS 2, 700 nm	27 nJ

head. The power in all other beams (unmeasureable with the first two heads, which are only good for > 500 nJ) was measured using an Ophir Vega meter and PD10-pj-C head.

We then developed a Labview program (now available on Github at `Sokolab/raman_labview`) to collect data. We used a Channeltron detector (CEM 4869, Scientific Instrument Services) to measure the number of ions produced and an oscilloscope (Tektronix C3000) to collect the resulting signal. The pressure in the gas chamber was set to 8.4×10^{-6} mbar. We focused all beams with an off-axis paraboloid (Newport 50332AL, 322$), avoiding lenses to minimize dispersion. For alignment, we set another mirror before the vacuum chamber. This reflects the beam as it focuses into a mounted sapphire window for best recreation of the vacuum conditions. The Reference beam, at full power, is strong enough to produce a plasma, but only when optimally focused. We

used the brightness of the plasma and resulting third-harmonic to optimize the alignment of the parabola. We then set all sidebands (Stokes, AS 1, and AS 2) in phase and varied the phase of the main 800 nm beam (termed Reference), measuring the ion signal as a function of the phase.

5.3 Experimental Methods

5.3.1 Plasma Overlap Method

Setting each beam in phase and ensuring spatial overlap is a complicated procedure. At low powers, the procedure outlined in Section 4 involving the synchronization of SFG signals works well. This synchronization is shown in Fig. 4.4, which was taken to prepare the beams for the experiments in this section. However, Reference, Stokes, and AS 1 are generally attenuated with an ND filter prior to being focused on the BBO. Removing these ND filters results in mismatched delays for each beam. Further, there are different dispersive regimes in the BBO and in the vacuum chamber. Aligning in open air is a better approximation of the conditions in the gas chamber than aligning in the crystal. To address both of these concerns, we aligned the beams using what I will call the "plasma overlap" method, developed originally from conversations with Peter Zhokhov and Ilya Fedotov. This method is illustrated in Figure 5.2.

The plasma formed by Reference will diffract collinear pulses that arrive after the plasma is formed. Hence, by observing the diffraction pattern on these other beams, we can determine all needed information. The beams are spatially aligned if a diffraction pattern is visible when the plasma is present, and they are temporally overlapped at the moment of plasma formation (which theoretically should happen at the peak of the pulse).

5.3.2 Vacuum Methods

All vacuum chamber parts were obtained from Kurt J. Lesker, while all pump parts were obtained from Pfeiffer Vacuum systems. I have compiled Table 5.2 describing parts and part numbers for future reference. All manuals are available upon request.

In the course of preparing this experiment, Aysan Bahari and I had to:

- Replace the Channeltron.
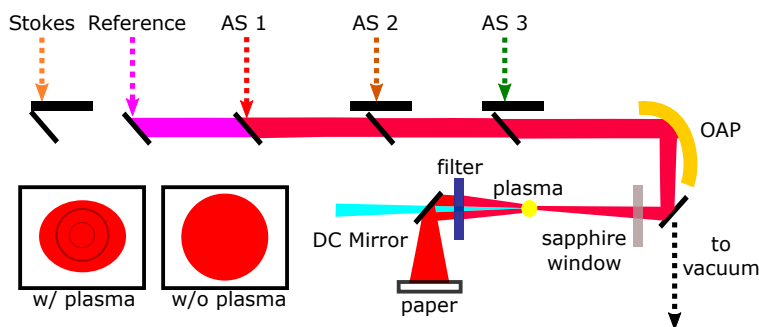
Figure 5.2: A schematic of the "plasma overlap" method. OAP stands for off axis paraboloid, DC stands for dichroic (Semrock FF605-Di02). By iteratively blocking and unblocking Stokes, and AS 1-3, while maximizing the plasma-induced distortion on each beam, cohesive temporal and spatial overlap can be achieved. The "filter" shown corresponds to a notch filter (Semrock NF03-808E) which blocks the Reference beam, this beam would otherwise be reflected by the DC mirror along with Stokes/AS 1-3 and make visual inspection of diffraction much more difficult. The insets are not real experimental data, but rather the author's best representation as to what this diffraction looks like. It is very difficult to take true-color images or measure the beam profile.

- Find leaks in the vacuum (after only lowering the pressure to $\approx 10^{-3}$).

- Subsequently replace the sapphire windows.

- Bake down to get to the lowest pressure (something like 6×10^{-8} mbar)

This subsection summarizes our experiences in attempting all of these things.

5.3.2.1 Preparing for Vacuum

If it becomes neccessary to open any of the flanges on the vacuum chamber, it is absolutely necessary to **replace** the copper gasket between the flanges. The gasket becomes deformed after every excursion under vacuum. Some may claim that the same gasket can be used twice as long as the second time, the flange is tighter, but this is not a claim worth verifying in this setup.

All of the flanges on the vacuum chamber belong to the category called "CF" or "knife-edge." In order to properly seal each flange, we used a torque wrench and tightened each bolt in a star pattern, as shown in Figure 5.3(a). For the $2 - 3/4$" flange, the maximum torque is 12 ft-lbs, or 144 in-lbs. We found 60 in-lbs, or half the maximum torque, to be sufficient to hold 10^{-7} mbar. We

Table 5.2: Vacuum parts needed to construct chamber with experimentally obtained 6×10^{-8} minimum pressure. All manuals are available upon request.

Parts	Part Numbers	Description
Sapphire windows	VPZL-275S	$2 - 3/4$" flange
Main vacuum body	C-0275	$2 - 3/4$" flange, 4-way CF cross
Copper gaskets	GA-0275LB	$2 - 3/4$" flange, 1.895" OD, 1.528" ID
Angle valve	VAT 284	on-off valve for connection to gas chamber
Main pump	TMU 071 P	Turbo, 1×10^{-8} mbar min. pressure
Backing pump	MVP 035	Diaphragm, 1 mbar min. pressure
Vacuum gauge	PKR 251	Pirani (high pressure) & cold cathode (low pressure)

initally tightened each bolt to 20 in-lbs, then added 5 in-lbs each time we went around the star. The proper torque for each flange depends on the size of the flange; a complete table matching flange size to torque is available on Kurt J. Lesker's website [110]. For example, the small, $1 - 1/3$" flange between the chamber and the angle valve requires only 7 ft-lbs of torque, much less than for the $2 - 3/4$" flange.

The key, we found, to keeping the vacuum was to ensure that the distance between the flanges was equal all around the flange, as in Fig. 5.3(b). This can be checked (after implementing the star tightening method) by using "feeler gauges." If the gauge gets stuck on any point between the bolts but doesn't get stuck on other points, the flange is not properly tightened.

5.3.2.2 *Finding Vacuum Leaks*

There are three ways we found from conversations with various people to find vacuum leaks without resorting to fancy helium detection equipment:

1. Cover all flange joints with soap and look for bubbles.

2. Put the chamber under pressure instead of without pressure and listen for hisses.

3. Cover all flange joints with methane or acetone and watch for pressure changes.

We explored all three of these very scientific ways. We found that the best soap for (1) was di-
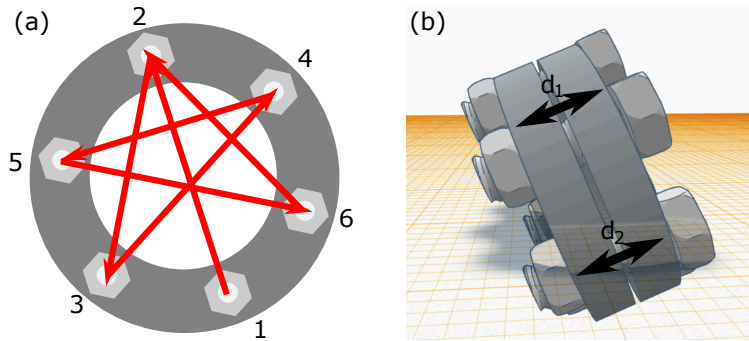
Figure 5.3: (a) Bolt-tightening order, from 1 to 6, with the "star" pattern drawn out for clarity. (b) A 3D model of two bolted flanges, drawn in Tinkercad. To best hold vacuum, we want an equal d_1 and d_2 all around the two flanges.

luted (not bubbling) hand soap. We also tried the bubbling hand soap and diluted dishwasher fluid. Neither of these worked well. Once we covered the windows with the hand soap, we immediately saw bubbles, replaced the windows, and threw a party (not a joke).

Before we successfully used nonbubbling hand soap, we thought that the proper kind of soap did not exist and so focused on (2) and (3). We filled the chamber with dry nitrogen gas but did not hear any hissing. We also used up a significant amount of methane pursuing route (3) - the idea is that the methane is supposed to be sucked into wherever the leak is coming from and freeze. We neglected to cover the windows with methane, which is presumably why this technique did not work for us.

5.3.2.3 *Heating and Baking*

To bring the chamber down to 1×10^{-7} mbar, it was necessary to heat (otherwise known as "bake") the chamber. This must be done **very carefully**, as the sapphire windows can break if exposed to large heat gradients. We wrapped 6 feet of electric heat tape (AWH-101-060DC-MP, HTS/Amptek) plugged into a variable autotransformer (type 3PN 1010, Staco) around the vacuum chamber. We also wrapped several layers of aluminum foil, which served as a heat shield, around the tape, giving special care to the windows. We then heated the vacuum chamber to $150°$ C as measured by a dual laser IR thermometer (Avantek). This is the **maximum** permissible
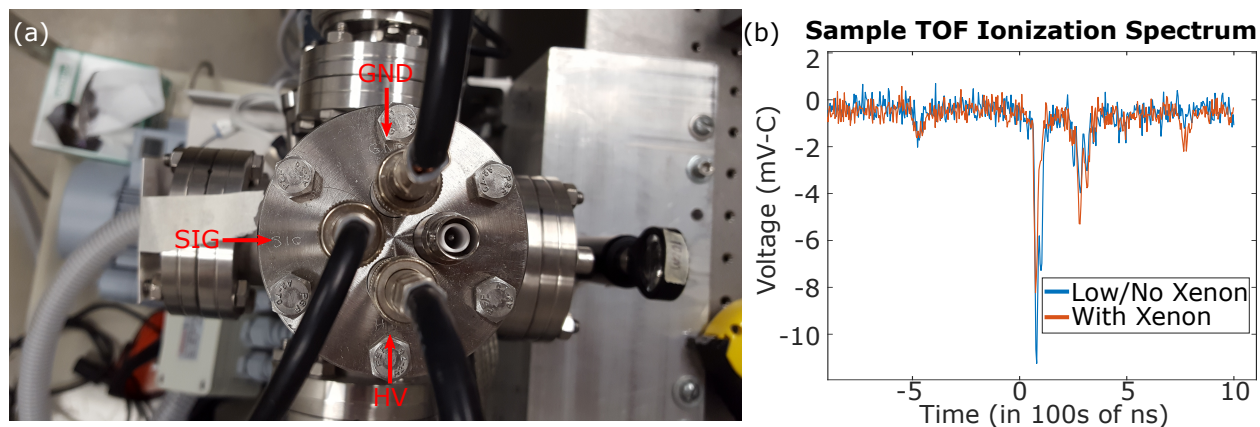
Figure 5.4: (a) Channeltron ports, top view. (b) A sample Channeltron ionization signal, as seen with an oscilloscope and subsequently saved onto a computer.

temperature – any more and the Channeltron may melt, or the angle valve or turbo pump may break.

We did this **slowly**, by varying the transformer voltage from 0 to 60 and going up by 1 V at a time. We then left the chamber with the pump and all valves open for anywhere between 12 hours and several days, depending on how much time was left before the pressure for experimental results overwhelmed us. Generally, 12 hours is accepted as being the minimum time for this procedure. We then carefully lowered the temperature by lowering the transformer voltage 1 V at a time.

5.3.3 Channeltron Methods

The Channeltron is mounted at the top of the chamber with a CF flange. The Channeltron has four (three useful and one empty) ports, located at the top of the instrument and shown in Fig. 5.4 (a).

The bottom-most port (labelled "HV" in the picture and scratched into the Channeltron's metal) connects to an extral Burle power supply (PF1056, 670 μA) to supply the bias voltage. The Channeltron requires a fairly high bias voltage ($1.5 - 3$ kV) in order to operate. After 1.5 kV, the strength of the signal increases until it saturates [111]. However, the Channeltron lifetime will shorten faster at higher voltages, so we usually kept the gain voltage at 1.5 kV and instead optimized the ion sig-

nal by adjusting the focusing optics in our setup.

Going clockwise, the ionization time-of-flight (TOF) signal is collected from the "SIG" port, on the middle-left port of the Channeltron. We used an oscilloscpe to collect this signal by way of a BNC cable from the Channeltron port to the scope; a sample signal is shown in Fig. 5.4. Any scope can be used in principle, but the lower-end ones (i.e. TDS 1002B) will require an additional resistance terminator, may not be able to resolve the TOF peaks adequately, and will have a lower signal-to-noise. The higher-end ones can be plugged in directly. Whatever the scope, it is best to trigger it using the "SYNC OUT DELAY" output on the Coherent Synchronization and Delay Generator (SDG) box. This signal should be aligned so that it triggers with the Channeltron as closely as possible (so that the higher resolution scope settings can be used). This can be adjusted by turning the knob of the "SYNC OUT DELAY" setting on the box, adding or removing delay. We typically set the "SYNC OUT DELAY" to its maximum (1000 ns), and used the "500 ns" (x axis) and "2.00 mV-C" (y axis) settings on the TDS 684C scope for alignment. However, we used a different scope for final data collection, as we were unable to synchronize the older scope with Labview.

Finally, we ensured that the Channeltron GND port (top of Fig. 5.4 (a)) and power supply shared a mutual ground by running a wire between them and fixing the wire to the optical table.

5.3.4 Note for Future Experiments

If anyone were to continue/repeat this experiment, I would strongly advise them to invest in the VAT 59024-GE01 leak valve from Kurt J. Lesker. It is a 2k investment, but is absolutely essential for doing this experiment in a repeatable way. The current valve on the vacuum setup is an "angle valve" (see Table 5.2) which is meant to serve strictly as an on/off valve only [112]. Adjusting the pressure with this valve is only possible in a very crude way. Hence, to achieve the preliminary results presented in this section, we would first pump out the vacuum chamber to $\approx 1 \times 10^{-7}$ mbar, then fill the gas chamber to atmospheric pressure with Xenon gas (Matheson), and finally pump it down again over the course of 24 hours to $\approx 6 \times 10^{-6}$ mbar, the maximum permissible pressure while allowing operation of the Channeltron. It is very difficult to estimate exactly how much time

is needed to pump to get as close to $\approx 6 \times 10^{-6}$ mbar, so often we would have to make do with $\approx 1 - 4 \times 10^{-6}$ mbar. This does not make for good, repeatable, experimental conditions, hence the recommendation to just buy the leak valve.

5.4 Results

After setting all sidebands in phase using the procedure detailed in Sec. 5.3.1 and obtaining an appropriate vacuum pressure, as detailed in 5.3.2, we varied the delay of Reference and observed the Channeltron TOF spectrum, as shown in Fig. 5.5. This spectrogram was taken at 1.0×10^{-6} mbar and 1.5 kV of bias voltage, with an initial vacuum pressure of $\approx 10^{-7}$ mbar. Despite a very visible Xenon peak at ≈ 275 ns, little variation in the ion signal was seen as the delay was varied. We saw no statistical difference between this spectrogram and the one taken without any sidebands (Fig 5.6).

According to [113], what we should see is enhancement of the ion signal when Reference is in phase with the sidebands and suppression of the ion signal when Reference is not in phase, roughly following the shape of the pulse envelope. However, we do not see this – likely because of the power issues mentioned in Section 5.1.

We also attempted to measure the power dependence of the ionization peak on the power of the Reference, without sidebands. The results are shown in Fig. 5.7. There are some strange items to note - the first ionization peak (at 0.1 microseconds) seems to have a much more nonlinear power dependence than the Xenon peak. If the experiment were to be repeated, a larger power range and perhaps a higher gain would be beneficial. A lower base vacuum pressure to reduce the noisy first ionization peak would also be helpful.

5.5 Future Work and Conclusions

To summarize, several factors limited the experiments in this section:

1. The lack of repeatable pressure conditions (as described in Section 5.3.4)

2. The unfavorable power ratio between Stokes/AS 1-2 beams and the Reference beam
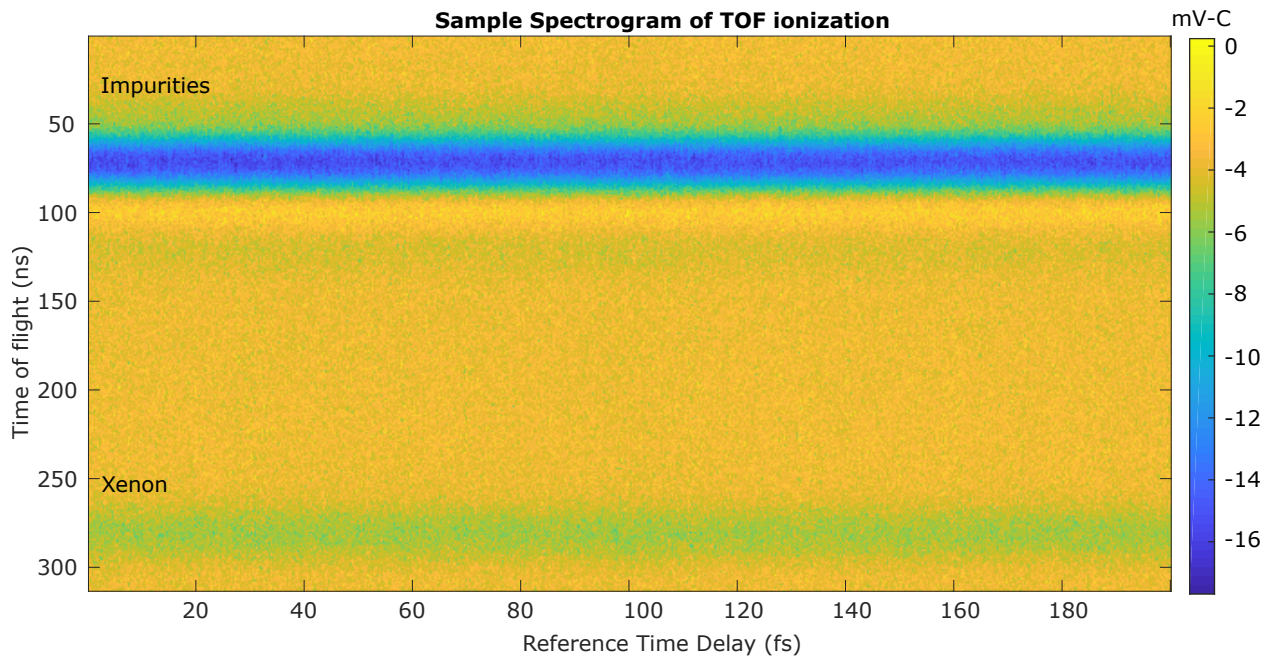
Figure 5.5: A "spectrogram" taken of the TOF ionization spectrum generated by the Reference beam and Stokes 1, AS 1-2 in phase. The Reference time delay is varied to generate the y-axis, while the x-axis corresponds to the time of flight as measured by the oscilloscope (i.e. it is the time axis of the oscilloscope, as shown in Fig. 5.4).
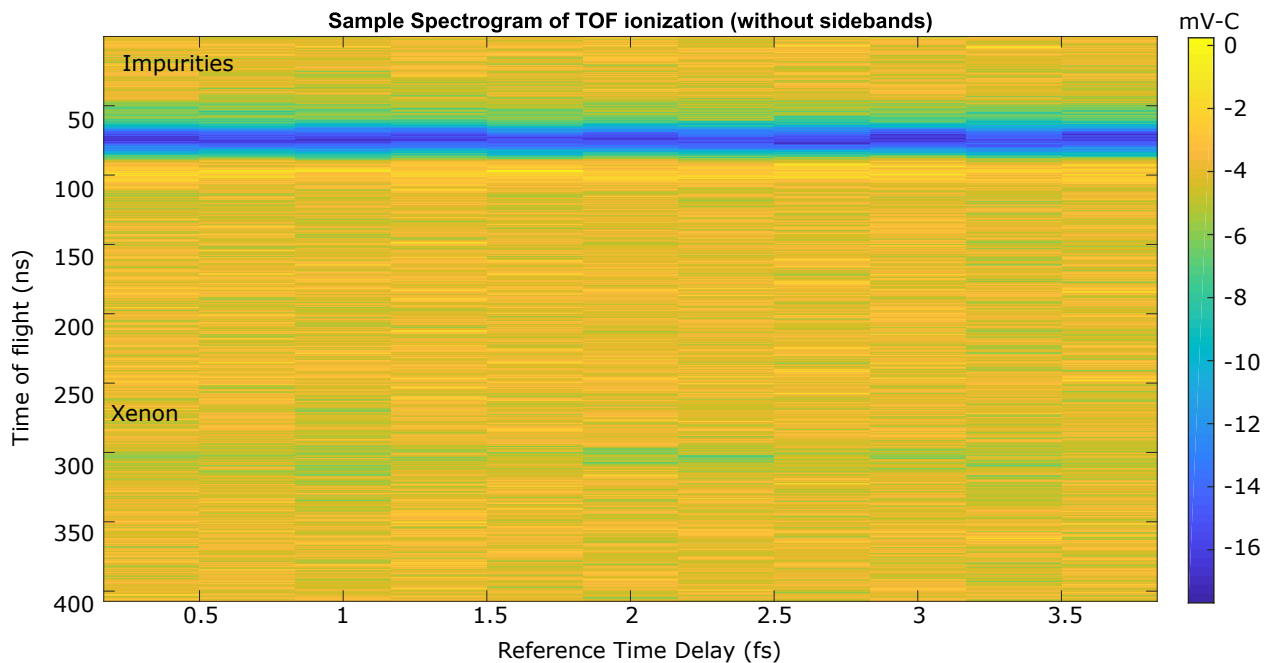
Figure 5.6: Despite the lowered resolution, it is obvious that the fluctuations we see in Fig. 5.5 are consistent with those seen from step to step here; hence, step size was minimized to save time and conserve resources.
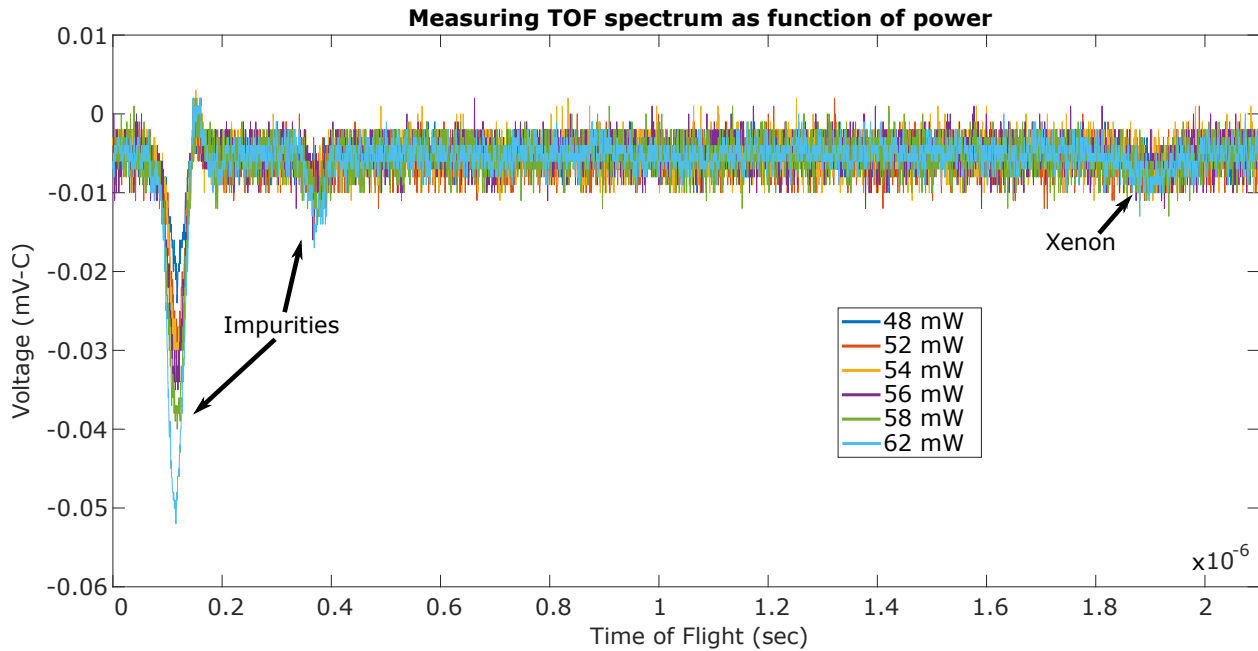
Figure 5.7: A series of TOF spectra taken from the oscilloscope (Tektronix) as a function of power in the Reference beam, without any sidebands.

3. No way to really check whether alignment in vacuum is the same as alignment in open air (as described in Section 5.3.1)

Increasing the power to the sidebands would be very helpful for taking care of points (2) and (3), as the higher power would allow for the possibility of nonlinear interaction between the sidebands in the vacuum chamber. This would allow us to characterize the synthesized waveform via the generated four-wave mixing signal, as in [31]. While the pressure in [31] is higher than in our experiment, we could set the vacuum chamber to high pressure, obtain the four-wave mixing signal, and slowly lower the pressure while continuously optimizing the signal to ensure overlap.

The power in the sidebands can be increased by scaling up the intensities of pump and Stokes. This can be done by increasing the average power to pump and Stokes while focusing less tightly (or by not putting the diamond in the focus). With our group's newly acquired 8 mJ laser system, we will have an order of magnitude increase in the power available to the OPA (from 500μJ to 5 mJ). This will, ideally, result in a corresponding increase to the energy in Stokes. Straightforward

80

scaling of our experimental conditions will be deployed by keeping the same intensity (power per unit area). For example, this means that we will use a spot size area 1500 times larger than previous experiments ($\sim 3 - 4$mm in diameter). Given the $\sim 31\%$ of conversion efficiency demonstrated by our group, a 1 mJ total energy in the spectrum of the Raman sidebands is very much achievable. This is the plan for the experiments next year, as led by A. Bahari.

6. SUMMARY AND CONCLUSIONS

In summary, this thesis describes various experiments done to better understand and manipulate Raman generation for the goal of synthesizing ultrashort pulses. These ultrashort pulses will be essential tools for the future of the field of femtochemistry, and ideally will lead to the control of electron dynamics on the attosecond time-scale.

In terms of this overall story, Section 2 summarizes our initial attempts at phase-only spatial control by looking at the transfer of topological charge in the Raman interaction. Section 3 then describes more sophisticated (but less theoretically understood) forays into tailoring white-light spectra via wavefront-optimization algorithms. This work also served to connect our spectral and spatial approaches to optimizing our Raman-generated pulse. A stronger connection between this work and Raman was subsequently forged by Shutova, et al. in [22].

Sections 4 and 5 then turned more directly to the question of spectral optimization of pulses synthesized via the coherent Raman technique. While Section 5 ends with sub-optimal results, we are confident that this will serve as a foundation for future work with Raman-generated pulses in vacuum and we see this as the main goal for our group.

Hence, we see this work as a significant milestone towards using Raman-based ultrafast sources to forward our understanding of attosecond dynamics.

REFERENCES

[1] A. Zhdanova, M. Zhi, and A. Sokolov, "Coherent Raman generation in solid-state materials using spatial and temporal laser field shaping," in *Front. Adv. Mol. Spectrosc.* (J. Laane, ed.), Elsevier, 2nd ed., 2017.

[2] M. Zhi, K. Wang, X. Hua, B. D. Strycker, and A. V. Sokolov, "Shaper-assisted phase optimization of a broad "holey" spectrum," *Opt. Express*, vol. 19, no. 23, p. 23400, 2011.

[3] K. Wang, M. Zhi, X. Hua, and A. V. Sokolov, "Ultrafast waveform synthesis and characterization using coherent Raman sidebands in a reflection scheme," *Opt. Express*, vol. 22, no. 18, pp. 21411–21420, 2014.

[4] A. A. Zhdanova, M. Shutova, A. Bahari, M. Zhi, and A. V. Sokolov, "Topological charge algebra of optical vortices in nonlinear interactions," *Opt. Express*, vol. 23, no. 26, pp. 34109–34117, 2015.

[5] A. A. Zhdanova, Y. Shen, J. V. Thompson, M. O. Scully, V. V. Yakovlev, and A. V. Sokolov, "Controlled supercontinua via spatial beam shaping," *J. Mod. Opt.*, 2017.

[6] L. Sudrie, A. Couairon, M. Franco, B. Lamouroux, B. Prade, S. Tzortzakis, and A. Mysyrowicz, "Femtosecond laser-induced damage and filamentary propagation in fused silica," *Phys. Rev. Lett.*, vol. 89, no. 18, p. 186601, 2002.

[7] J. E. Rothenberg, "Pulse splitting during self-focusing in normally dispersive media," *Opt. Lett.*, vol. 17, no. 8, pp. 583–585, 1992.

[8] M. Zhi, K. Wang, X. Hua, and A. V. Sokolov, "Pulse-shaper-assisted phase control of a coherent broadband spectrum of Raman sidebands," *Opt. Lett.*, vol. 36, no. 20, pp. 4032–4, 2011.

[9] I. Shpinkov, I. Kamenskikh, M. Kirm, V. Kolobanov, V. Mikhailin, A. Vasilev, and G. Zimmerer, "Optical functions and luminescence quantum yield of lead tungstate," *Phys. Status*

Solidi, vol. 170, no. 1, pp. 167–173, 1998.

[10] Diamond Materials: Advanced Diamond Technology, "The CVD diamond booklet," 2014.

[11] M. Zhi and A. V. Sokolov, "Broadband generation in a Raman crystal driven by a pair of time-delayed linearly chirped pulses," *New J. Phys.*, vol. 10, no. 2, p. 025032, 2008.

[12] A. H. Zewail, "Femtochemistry: ultrafast dynamics of the chemical bond," *J. Phys. Chem. A*, vol. 104, no. 24, pp. 5660–5694, 2000.

[13] S. T. Cundiff and A. M. Weiner, "Optical arbitrary waveform generation," *Nat. Photonics*, vol. 4, no. 11, pp. 760–766, 2010.

[14] S. Rausch, T. Binhammer, A. Harth, J. Kim, R. Ell, F. X. Kärtner, and U. Morgner, "Controlled waveforms on the single-cycle scale from a femtosecond oscillator," *Opt. Express*, vol. 16, no. 13, pp. 9739–9745, 2008.

[15] F. Ferdous, H. Miao, D. E. Leaird, K. Srinivasan, J. Wang, L. Chen, L. T. Varghese, and A. M. Weiner, "Spectral line-by-line pulse shaping of on-chip microresonator frequency combs," *Nat. Photonics*, vol. 5, no. 12, pp. 770–776, 2011.

[16] G. Sansone, L. Poletto, and M. Nisoli, "High-energy attosecond light sources," *Nat. Photonics*, vol. 5, no. 11, pp. 655–663, 2011.

[17] A. Wirth, M. Hassan, I. Grguras, J. Gagnon, A. Moulet, T. Luu, S. Pabst, R. Santra, Z. Alahmed, A. Azzeer, V. Yakovlev, V. Pervak, F. Krausz, and E. Goulielmakis, "Synthesized light transients," *Science*, vol. 334, no. 6053, pp. 195–200, 2011.

[18] M. T. Hassan, T. T. Luu, A. Moulet, O. Raskazovskaya, P. Zhokhov, M. Garg, N. Karpowicz, A. M. Zheltikov, V. Pervak, F. Krausz, and E. Goulielmakis, "Optical attosecond pulses and tracking the nonlinear response of bound electrons," *Nature*, vol. 530, no. 7588, pp. 66–70, 2016.

[19] S.-W. Huang, G. Cirmi, J. Moses, K.-H. Hong, S. Bhardwaj, J. R. Birge, L.-J. Chen, E. Li, B. J. Eggleton, G. Cerullo, and F. X. Kärtner, "High-energy pulse synthesis with sub-cycle waveform control for strong-field physics," *Nat. Photonics*, vol. 5, no. 8, pp. 475–479, 2011.

[20] P. Krogen, H. Suchowski, H. Liang, N. Flemens, K.-H. Hong, F. X. Kärtner, and J. Moses, "Generation and multi-octave shaping of mid-infrared intense single-cycle pulses," *Nat. Photonics*, vol. 11, no. 4, pp. 222–226, 2017.

[21] V. Shumakova, P. Malevich, S. Ališauskas, A. M. Zheltikov, A. A. Voronin, D. Faccio, D. Kartashov, A. Baltuška, and A. Pugžlys, "Multi-millijoule few-cycle mid-IR pulses through nonlinear self-compression in bulk," *Nat. Commun.*, vol. 7, p. 12877, 2016.

[22] M. Shutova, A. Shutov, J. V. Thompson, A. A. Zhdanova, and A. V. Sokolov, "Extending total bandwidth of broadband coherent Raman generation via adaptive optics," *Prep.*, 2018.

[23] A. Weiner, *Ultrafast optics*. John Wiley & Sons, Inc., 2009.

[24] R. Trebino, K. W. Delong, D. N. Fittinghoff, J. N. Sweetser, M. A. KrumbuÌĹgel, B. A. Richman, and D. J. Kane, "Measuring ultrashort laser pulses in the time-frequency domain using frequency-resolved optical gating," *Rev. Sci. Instrum.*, vol. 68, no. 9, pp. 3277–3295, 1997.

[25] R. W. Boyd, "Nonlinear optics - chapter 2," in *Nonlinear Opt.*, ch. 2, pp. 69–133, Elsevier, 2008.

[26] M.-C. Chen, C. Mancuso, C. Hernández-García, F. Dollar, B. Galloway, D. Popmintchev, P.-C. Huang, B. Walker, L. Plaja, A. A. Jaroń-Becker, A. Becker, M. M. Murnane, H. C. Kapteyn, and T. Popmintchev, "Generation of bright isolated attosecond soft X-ray pulses driven by multicycle midinfrared lasers," *Proc. Natl. Acad. Sci. U. S. A.*, vol. 111, no. 23, pp. 1–7, 2014.

[27] K. Zhao, Q. Zhang, M. Chini, Y. Wu, X. Wang, and Z. Chang, "Tailoring a 67 attosecond pulse through advantageous phase mismatch," *Opt. Lett.*, vol. 37, no. 18, pp. 3891–3893, 2012.

[28] A. V. Sokolov and S. E. Harris, "Ultrashort pulse generation by molecular modulation," *J. Opt. B Quantum Semiclass. Opt.*, vol. 5, no. 1, pp. R1–R26, 2003.

[29] A. V. Sokolov, "Subfemtosecond compression of periodic laser pulses," *Opt. Lett.*, vol. 24, no. 17, pp. 1248–1250, 1999.

[30] D. Yavuz, D. Walker, G. Yin, and S. Harris, "Rotational Raman generation with near-unity conversion efficiency," *Opt. Lett.*, vol. 27, no. 9, pp. 769–71, 2002.

[31] M. Shverdin, D. Walker, D. Yavuz, G. Yin, and S. Harris, "Generation of a single-cycle optical pulse," *Phys. Rev. Lett.*, vol. 94, p. 033904, jan 2005.

[32] M. Katsuragawa, K. Yokoyama, T. Onose, and K. Misawa, "Generation of a 10.6-THz ultrahigh-repetition-rate train by synthesizing phase-coherent Raman-sidebands," *Opt. Express*, vol. 13, no. 15, pp. 5628–34, 2005.

[33] K. R. Pandiri and M. Katsuragawa, "A 10 THz ultrafast function generator-generation of rectangular and triangular pulse trains," *New J. Phys.*, vol. 13, no. 2009, pp. 1–5, 2011.

[34] J. Zheng and M. Katsuragawa, "Freely designable optical frequency conversion in Raman-resonant four-wave-mixing process," *Sci. Rep.*, vol. 5, p. 8874, 2015.

[35] E. Sali, K. J. Mendham, J. W. G. Tisch, T. Halfmann, and J. P. Marangos, "High-order stimulated Raman scattering in a highly transient regime driven by a pair of ultrashort pulses," *Opt. Lett.*, vol. 29, no. 5, pp. 495–497, 2004.

[36] D. R. Austin, T. Witting, S. J. Weber, P. Ye, T. Siegel, P. Matia-Hernando, A. S. Johnson, J. W. G. Tisch, and J. P. Marangos, "Spatio-temporal characterization of intense few-cycle 2 µm pulses," *Opt. Express*, vol. 24, no. 21, pp. 24786–24798, 2016.

[37] H.-S. Chan, Z.-M. Hsieh, W.-H. Liang, A. Kung, C.-K. Lee, C.-J. Lai, R.-P. Pan, and L.-H. Peng, "Synthesis and measurement of ultrafast waveforms from five discrete optical harmonics," *Science (80-.).*, vol. 331, pp. 1165–1168, 2011.

[38] A. M. Burzo and A. V. Sokolov, "Broadband modulation of light by coherent molecular oscillations," in *Front. Mol. Spectrosc.*, ch. 12, pp. 347–366, Elsevier B.V., first ed., 2009.

[39] M. Zhi and A. V. Sokolov, "Broadband coherent light generation in a Raman-active crystal driven by two-color femtosecond laser pulses," *Opt. Lett.*, vol. 32, no. 15, pp. 2251–2253, 2007.

[40] M. Zhi, X. Wang, and A. V. Sokolov, "Broadband coherent light generation in diamond driven by femtosecond pulses," *Opt. Express*, vol. 16, no. 16, pp. 12139–12147, 2008.

[41] A. A. Annenkov, M. V. Korzhik, and P. Lecoq, "Lead tungstate scintillation material," *Nucl. Instruments Methods Phys. Res. Sect. A Accel. Spectrometers, Detect. Assoc. Equip.*, vol. 490, no. 1-2, pp. 30–50, 2002.

[42] A. A. Kaminskii, C. L. McCray, H. R. Lee, S. W. Lee, D. A. Temple, T. H. Chyba, W. D. Marsh, J. C. Barnes, A. N. Annanenkov, V. D. Legun, H. J. Eichler, G. M. A. Gad, and K. Ueda, "High efficiency nanosecond Raman lasers based on tetragonal PbWO4 crystals," *Opt. Commun.*, vol. 183, no. 1, pp. 277–287, 2000.

[43] G. M. A. Gad, H. J. Eichler, and A. A. Kaminskii, "Highly efficient 1.3-μm second-Stokes PbWO 4 Raman laser," *Opt. Lett.*, vol. 28, no. 6, pp. 426–428, 2003.

[44] A. A. Zhdanova and R. Letiecq, "Personal notes from 2/22/16 coherent engineer visit," tech. rep., Texas A&M University, 2016.

[45] K. Wang, A. Zhdanova, M. Zhi, X. Hua, and A. Sokolov, "Multicolored femtosecond pulse synthesis using coherent Raman sidebands in a reflection Scheme," *Appl. Sci.*, vol. 5, no. 2, pp. 145–156, 2015.

[46] M. Zhi and A. V. Sokolov, "Toward single-cycle pulse generation in Raman-active crystals," *IEEE J. Sel. Top. Quantum Electron.*, vol. 18, no. 1, pp. 460–466, 2012.

[47] FASTLITE, "Phazzler system operating manual," 2009.

[48] M. V. Vasnetsov and K. Staliunas, *Linear theory of optical vortices*. Nova Science Publishers, Inc, 1999.

[49] J. F. Nye and M. V. Berry, "Dislocations in wave trains," *Proc. R. Soc. London A*, vol. 336, pp. 165–190, 1974.

[50] A. M. Yao and M. J. Padgett, "Orbital angular momentum: origins, behavior and applications," *Adv. Opt. Photonics*, vol. 3, pp. 161–204, may 2011.

[51] H. He, M. Friese, N. Heckenberg, and H. Rubinsztein-Dunlop, "Direct observation of transfer of angular momentum to absorptive particles from a laser beam with a phase singularity," *Phys. Rev. Lett.*, vol. 75, no. 5, pp. 826–829, 1995.

[52] A. M. Akulshin, R. J. Mclean, E. E. Mikhailov, and I. Novikova, "Distinguishing nonlinear processes in atomic media via orbital angular momentum transfer," *Opt. Lett.*, vol. 40, no. 6, pp. 1109–1112, 2015.

[53] F. M. Fazal and S. M. Block, "Optical tweezers study life under tension," *Nat. Photonics*, vol. 5, no. 6, pp. 318–321, 2011.

[54] M. J. Padgett, "Light in a twist: optical angular momentum," *Proc. SPIE*, vol. 8637, p. 863702, 2013.

[55] D. G. Grier, "A revolution in optical manipulation," *Nature*, vol. 424, pp. 810–816, 2003.

[56] T. A. Klar, E. Engel, and S. W. Hell, "Breaking Abbe's diffraction resolution limit in fluorescence microscopy with stimulated emission depletion beams of various shapes," *Phys. Rev. E*, vol. 64, no. 6, p. 066613, 2001.

[57] G. A. Swartzlander, "Peering into darkness with a vortex spatial filter," *Opt. Lett.*, vol. 26, no. 8, pp. 497–499, 2001.

[58] G. Foo, D. M. Palacios, and G. A. Swartzlander Jr, "Optical vortex coronagraph," *Opt. Lett.*, vol. 30, no. 24, pp. 3308–3310, 2005.

[59] A. Mair, A. Vaziri, G. Weihs, and A. Zeilinger, "Entanglement of the orbital angular momentum states of photons," *Nature*, vol. 412, pp. 313–316, 2001.

[60] E. A. Gibson, A. Paul, N. Wagner, R. Tobey, S. Backus, I. P. Christov, M. M. Murnane, and H. C. Kapteyn, "High-order harmonic generation up to 250 eV from highly ionized Argon," *Phys. Rev. Lett.*, vol. 92, no. 3, p. 033001, 2004.

[61] A. V. Sokolov and S. E. Harris, "Ultrashort pulse generation by molecular modulation," *J. Opt. B Quantum Semiclass. Opt.*, vol. 5, pp. R1–R26, 2003.

[62] A. Sokolov, M. Shverdin, D. Walker, D. Yavuz, A. Burzo, G. Yin, and S. Harris, "Generation and control of femtosecond pulses by molecular modulation," *J. Mod. Opt.*, vol. 52, no. 2-3, pp. 285–304, 2005.

[63] J. Strohaber, M. Zhi, A. V. Sokolov, A. A. Kolomenskii, G. G. Paulus, and H. A. Schuessler, "Coherent transfer of optical orbital angular momentum in multi-order Raman sideband generation," *Opt. Lett.*, vol. 37, no. 16, pp. 3411–3413, 2012.

[64] M. Zhi, K. Wang, X. Hua, H. Schuessler, J. Strohaber, and A. V. Sokolov, "Generation of femtosecond optical vortices by molecular modulation in a Raman-active crystal," *Opt. Express*, vol. 21, no. 23, pp. 27750–27758, 2013.

[65] N. Bozinovic, S. Golowich, P. Kristensen, and S. Ramachandran, "Control of orbital angular momentum of light with optical fibers," *Opt. Lett.*, vol. 37, no. 13, pp. 2451–2454, 2012.

[66] A. M. Amaral, E. L. Falcão-Filho, and C. B. de Araújo, "Characterization of topological charge and orbital angular momentum of shaped optical vortices," *Opt. Express*, vol. 22, no. 24, pp. 30315–30324, 2014.

[67] T. Roger, J. J. Heitz, E. M. Wright, and D. Faccio, "Non-collinear interaction of photons with orbital angular momentum," *Sci. Rep.*, vol. 3, p. 3491, 2013.

[68] G. Molina-Terriza, J. P. Torres, and L. Torner, "Orbital angular momentum of photons in noncollinear parametric downconversion," *Opt. Commun.*, vol. 228, pp. 155–160, 2003.

[69] D. Persuy, M. Ziegler, O. Crégut, K. Kheng, M. Gallart, B. Hönerlage, and P. Gilliot, "Four-wave mixing in quantum wells using femtosecond pulses with Laguerre-Gauss modes," *Phys. Rev. B*, vol. 92, no. 11, p. 115312, 2015.

[70] K. Dholakia, N. B. Simpson, M. J. Padgett, and L. Allen, "Second-harmonic generation and the orbital angular momentum of light," *Phys. Rev. A*, vol. 54, no. 5, pp. R3742–R3745, 1996.

[71] J. Liao, X. Wang, W. Sun, Y. Tan, D. Kong, Y. Nie, J. Qi, H. Jia, J. Liu, J. Yang, J. Tan, and X. Li, "Analysis of femtosecond optical vortex beam generated by direct wave-front modulation," *Opt. Eng.*, vol. 52, no. 10, p. 106102, 2013.

[72] H. Ma, Z. Liu, H. Wu, X. Xu, and J. Chen, "Adaptive correction of vortex laser beam in a closed-loop system with phase only liquid crystal spatial light modulator," *Opt. Commun.*, vol. 285, no. 6, pp. 859–863, 2012.

[73] W. M. Lee, X. C. Yuan, and K. Dholakia, "Experimental observation of optical vortex evolution in a Gaussian beam with an embedded fractional phase step," *Opt. Commun.*, vol. 239, no. 1-3, pp. 129–135, 2004.

[74] C.-S. Guo, L.-L. Lu, and H.-T. Wang, "Characterizing topological charge of optical vortices by using an annular aperture," *Opt. Lett.*, vol. 34, no. 23, pp. 3686–3688, 2009.

[75] Y. Peng, X.-T. Gan, P. Ju, Y.-D. Wang, and J.-L. Zhao, "Measuring topological charges of optical vortices with multi-singularity using a cylindrical lens," *Chinese Phys. Lett.*, vol. 32, no. 2, p. 024201, 2015.

[76] M. Harris, C. A. Hill, P. R. Tapster, and J. M. Vaughan, "Laser modes with helical wave fronts," *Phys. Rev. A*, vol. 49, no. 4, pp. 3119–3122, 1994.

[77] P. Vaity, J. Banerji, and R. Singh, "Measuring the topological charge of an optical vortex by using a tilted convex lens," *Phys. Lett. A*, vol. 377, no. 15, pp. 1154–1156, 2013.

[78] R. L. Phillips and L. C. Andrews, "Spot size and divergence for Laguerre Gaussian beams of any order," *Appl. Opt.*, vol. 22, no. 5, pp. 643–644, 1983.

[79] S. G. Reddy, S. Prabhakar, A. Kumar, J. Banerji, and R. Singh, "Higher order optical vortices and formation of speckles," *Opt. Lett.*, vol. 39, no. 15, pp. 4364–4367, 2014.

[80] M. Shutova, A. A. Zhdanova, and A. V. Sokolov, "Detection of mixed OAM states via vortex breakup," *Phys. Lett. A*, vol. 381, no. 4, pp. 408–412, 2017.

[81] Y. Liu, M. King, H. Tu, Y. Zhao, and S. A. Boppart, "Broadband nonlinear vibrational spectroscopy by shaping a coherent fiber supercontinuum," *Opt. Express*, vol. 21, no. 7, pp. 8269–8275, 2013.

[82] H. Kano and H.-O. Hamaguchi, "Vibrationally resonant imaging of a single living cell by supercontinuum-based multiplex coherent anti-Stokes Raman scattering microspectroscopy," *Opt. Express*, vol. 13, no. 4, pp. 1322–1327, 2005.

[83] V. V. Yakovlev, B. Kohler, and K. R. Wilson, "Broadly tunable 30-fs pulses produced by optical parametric amplification," *Opt. Lett.*, vol. 19, no. 23, pp. 2000–2002, 1994.

[84] G. Cerullo and S. De Silvestri, "Ultrafast optical parametric amplifiers," *Rev. Sci. Instrum.*, vol. 74, no. 1, pp. 1–18, 2003.

[85] R. R. Alfano, *The supercontinuum laser source*. New York, NY: Springer, 2nd ed., 2006.

[86] D. Majus and A. Dubietis, "Statistical properties of ultrafast supercontinuum generated by femtosecond Gaussian and Bessel beams: a comparative study," *J. Opt. Soc. Am. B*, vol. 30, no. 4, pp. 994–999, 2013.

[87] H. I. Sztul, V. Kartazayev, and R. R. Alfano, "Laguerre-Gaussian supercontinuum," *Opt. Lett.*, vol. 31, no. 18, pp. 2725–2727, 2006.

[88] R. Borrego-Varillas, J. Pérez-Vizcaíno, O. Mendoza-Yero, G. Mínguez-Vega, J. R. V. De Aldana, and J. Lancis, "Controlled multibeam supercontinuum generation with a spatial light modulator," *IEEE Photonics Technol. Lett.*, vol. 26, no. 16, pp. 1661–1664, 2014.

[89] J. V. Thompson, M. M. Springer, A. J. Traverso, A. Zheltikov, A. V. Sokolov, and M. O. Scully, "Amplitude concentration in a phase-modulated spectrum due to femtosecond filamentation," *Sci. Rep.*, vol. 7, p. 43367, 2017.

[90] R. Ackermann, E. Salmon, N. Lascoux, J. Kasparian, P. Rohwetter, K. Stelmaszczyk, S. Li, A. Lindinger, L. Wöste, P. Béjot, L. Bonacina, and J.-P. Wolf, "Optimal control of filamentation in air," *Appl. Phys. Lett.*, vol. 89, no. 17, p. 171117, 2006.

[91] J. V. Thompson, B. H. Hokr, G. A. Throckmorton, D. Wang, M. O. Scully, and V. V. Yakovlev, "Enhanced second harmonic generation efficiency via wavefront shaping," *Submitted*, 2016.

[92] J. V. Thompson, G. A. Throckmorton, B. H. Hokr, and V. V. Yakovlev, "Wavefront shaping enhanced Raman scattering in a turbid medium," *Opt. Lett.*, vol. 41, no. 8, pp. 1769–1772, 2016.

[93] G. Fibich and A. L. Gaeta, "Critical power for self-focusing in bulk media and in hollow waveguides.," *Opt. Lett.*, vol. 25, no. 5, pp. 335–337, 2000.

[94] I. H. Malitson, "Refractive index and birefringence of synthetic sapphire," *J. Opt. Soc. Am.*, vol. 52, no. 12, pp. 1377–1379, 1962.

[95] A. Major, F. Yoshino, I. Nikolakakos, J. S. Aitchison, and P. W. E. Smith, "Dispersion of the nonlinear refractive index in sapphire," *Opt. Lett.*, vol. 29, no. 6, pp. 602–604, 2004.

[96] I. M. Vellekoop and A. P. Mosk, "Phase control algorithms for focusing light through turbid media," *Opt. Commun.*, vol. 281, no. 11, pp. 3071–3080, 2008.

[97] J. Thompson, B. Hokr, and V. Yakovlev, "Optimization of focusing through scattering media using the continuous sequential algorithm," *J. Mod. Opt.*, vol. 63, no. 1, pp. 80–84, 2016.

[98] K. Cook, A. K. Kar, and R. A. Lamb, "White-light supercontinuum interference of self-focused filaments in water," *Appl. Phys. Lett.*, vol. 83, no. 19, pp. 3861–3863, 2003.

[99] P. A. Zhokhov and A. M. Zheltikov, "Nonlinear-optical coherent combining of supercontinua from multiple filaments," *Phys. Rev. A*, vol. 86, no. 1, p. 013816, 2012.

[100] P. Zhokhov, *Subcycle dynamics of laser-induced ionization and tailored laser filaments*. PhD thesis, Texas A&M University, 2015.

[101] A. Couairon, E. Brambilla, T. Corti, D. Majus, O. de J. Ramírez-Góngora, and M. Kolesik, "Practitioner's guide to laser pulse propagation models and simulation," *Eur. Phys. J. Spec. Top.*, vol. 199, no. 1, pp. 5–76, 2011.

[102] M. Kolesik, J. V. Moloney, and M. Mlejnek, "Unidirectional optical pulse propagation equation," *Phys. Rev. Lett.*, vol. 89, no. 28, pp. 1–4, 2002.

[103] M. Kolesik and J. V. Moloney, "Nonlinear optical pulse propagation simulation: From Maxwell's to unidirectional equations," *Phys. Rev. E.*, vol. 70, no. 3, p. 11, 2004.

[104] J. V. Thompson, *Enhanced optical sensing via wavefront shaping and microscopic interface engineering*. PhD thesis, Texas A&M University, 2017.

[105] A. M. Zheltikov, "Let there be white light: supercontinuum generation by ultrashort laser pulses," *Physics-Uspekhi*, vol. 49, no. 6, pp. 605–628, 2006.

[106] R. Trebino, "Trebino-group code for retrieving a pulse intensity and phase from its FROG trace," 2016. Available at `http://frog.gatech.edu/code.html`.

[107] R. Trebino, *Frequency-resolved optical gating: the measurement of ultrashort laser pulses*. 2000.

[108] M. Kress, T. Löffler, S. Eden, M. Thomson, and H. G. Roskos, "Terahertz-pulse generation by photoionization of air with laser pulses composed of both fundamental and second-harmonic waves," *Opt. Lett.*, vol. 29, no. 10, pp. 1120–1122, 2004.

[109] D. J. Cook and R. M. Hochstrasser, "Intense terahertz pulses by four-wave rectification in air," *Opt. Lett.*, vol. 25, no. 16, pp. 1210–1212, 2000.

[110] K. J. Lesker, "CF flanges technical notes," 2017.

[111] Burle, "Channeltron electron multiplier handbook for mass spectrometry applications," tech. rep., 2017.

[112] K. J. Lesker, "Vacuum valves," 2017. Available at `https://www.lesker.com/newweb/flanges/flanges_technicalnotes_conflat_1.cfm`.

[113] A. V. Sokolov, D. R. Walker, D. D. Yavuz, G. Y. Yin, and S. E. Harris, "Femtosecond light source for phase-controlled multiphoton ionization," *Phys. Rev. Lett.*, vol. 87, no. 3, p. 033402, 2001.

APPENDIX A

ALIGNMENT FOR SECTION 4

The rough alignment procedure we used is as follows, from beginning of the setup to the end.

We first mesaured the distance each sideband travels from the diamond to the BBO. We then adjusted the setup in such a way to ensure that the distance was equal for each sideband. So long as we are accurate to within an inch, the precise alignment can be found by looking for SFG signals in the BBO as we vary the delay of each sideband. Once this time-distance measurement is done, we collinearly recombined all beams to a single row of screw holes on the optical table to ensure that the second harmonics and sum-frequencies of all beams will also be collinear (and hence interfere). This step can be done by carefully aligning to two spatially separated pinholes. The more separated these pinholes, the more accurate the setup.

We then placed the focusing lens into the collinear part of the setup, such that all recombined beams were focused. We then examined the spatial overlap of the focused beams in the place where the BBO should be. This can be done in several ways. The most accurate way is to take a thin piece of paper, burn a small hole in it by using the full power of Reference, and tweak the alignment of each AS n dichroic until each AS n beam passes through the hole. Rough alignment can be done simply by examining focal spots on a piece of paper (such as a business card) and again, tweaking the angle of each AS n dichroic until each AS n beam is aligned to the Reference focal spot on the card. It is best that this spatial alignment procedure is performed at the focal point of the beam - that way, the BBO can be placed at the place where the optimal SHG signal is generated and ensure that it is the same place where spatial overlap was examined.

Once this is done, the thick BBO is placed at the focal point and rotated to an angle between the optimal phase-matching angle for the SHG of Reference and the SHG of whichever AS n overlap is in question. A business card can be placed after the filters in Fig. 4.2 to examine any additional light that leaves the BBO. The time delay of Reference is then varied until an SFG signal
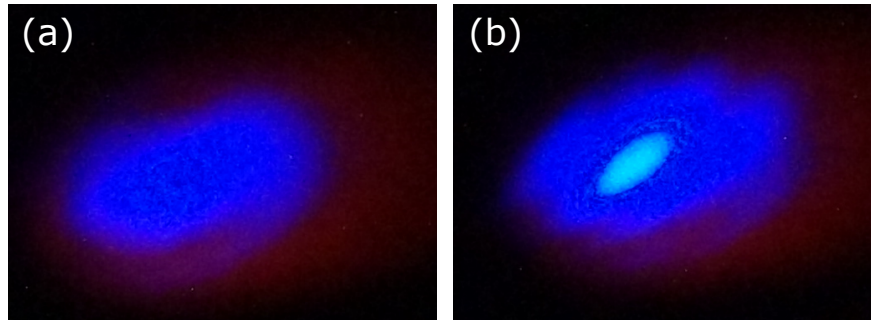
Figure A.1: UV interference fringes (i.e. ≈ 325 nm), out of a 1 mm thick BBO crystal; true-color photos taken with a Sony $\alpha 37$ DSLR camera. (a) Second harmonic of AS 3, imaged by blocking AS 4. (b) Second harmonic of AS 3, interfering with the sum frequency generated by AS 2 and AS 4. A bright fringe is seen in the middle, surrounded by darker fringes.

is visible. The AS n dichroic mirror should be tweaked so as to optimize this signal. This process is then repeated for all beams. Synchronization is obtained by choosing a beam (i.e. Stokes), moving the Reference stage to the point where the SFG between Stokes and Reference is visible, and moving each subsequent AS n delay stage until the SFG signal appears without having to move the Reference stage. This is simpler than finding the initial overlap with the AS n stage as it minimizes the necessary precision with which each delay stage must be aligned. This way, only the Reference stage has to be carefully aligned in order to minimize possible deviations in the spatial overlap as the stage is moved.

If all is done well and several beams are collinearly overlapped, the sum-frequency of two sidebands should interfere and produce spatial fringes with the second-harmonic of a third, as described in detail in Section 4.2.2.2 and illustrated in Fig. A.1.

Once the needed beams are synchronized and spatial fringes are visible, the thin BBO can be placed instead of the thick BBO. Minor deviations in spatial alignment are possible, the SFG signal should be reoptimized after this replacement procedure. The BBO might also be not in the exactly optimal spot - once the SFG signal is optimized by tweaking the AS n dichroic, the BBO can be shifted back and forth to see if further SFG optimization is possible. Spatial fringes are unlikely to be seen (as the signals in the thin BBO are much weaker than in the thick BBO), but generally

the temporal beats can be seen once the spectrometer signal is optimized. If beats are not seen, continue tweaking the AS n dichroics until beats are visible.